[redacted] 63 10097 Copy 599

NASA TM X-647

NASA TM X-647

TECHNICAL MEMORANDUM

X - 647

PRESSURE AND HEAT-TRANSFER MEASUREMENTS ON A MERCURY CAPSULE MODEL

By John O. Reller, Jr., and H. Lee Seegmiller

Ames Research Center
Moffett Field, Calif.

Declassified by authority of NASA
Classification Change Notices No. 143
Dated ** 6/28/61

[redacted]

[redacted]

NATIONAL AERONAUTICS AND SPACE ADMINISTRATION
WASHINGTON [redacted] May 1962

[redacted]

TABLE OF CONTENTS

Page

- SUMMARY 1
- INTRODUCTION 2
- SYMBOLS 3
- TEST FACILITIES 5
  - Wind Tunnel 5
  - Shock Tunnels 5
  - Free Flight 6
- MODELS AND INSTRUMENTATION 7
  - Wind Tunnel 7
  - Shock Tunnel 7
  - Free Flight 8
- REDUCTION AND ACCURACY OF DATA 8
  - Reduction of Wind-Tunnel Data 8
  - Reduction of Shock-Tunnel Data 10
    - Air stream calibration 10
    - Chemical equilibrium in model flow field 10
    - Reduction of heat-transfer data 10
  - Collected Flow Visualization Data 13
  - Accuracy of the Results 14
- RESULTS AND DISCUSSION 15
  - Stagnation Region 16
  - Heat Shield 17
    - Pressure distribution 17
    - Heating-rate distribution 18
  - Afterbody 19
    - Longitudinal pressure distribution 19
    - Circumferential pressure distribution 21
    - Real-gas effects on afterbody pressures 22
    - Variation of afterbody pressures with angle of attack 23
    - Longitudinal distribution of heat-transfer rates 23
    - Circumferential distribution of heating rates 25
    - Variation of afterbody heating rates with angle of attack 25
    - Real-gas effects on heat-transfer rates to the afterbody 26
  - Afterbody Flow Regimes 28
- CONCLUSIONS 30
- APPENDIX A - CALIBRATION OF THE 2-INCH SHOCK TUNNEL 32
- APPENDIX B - CHEMICAL EQUILIBRIUM IN MODEL FLOW FIELD 36
- REFERENCES 38
- TABLES 42
- FIGURES 45

[redacted]

DECLASSIFIED

[redacted]

NATIONAL AERONAUTICS AND SPACE ADMINISTRATION

TECHNICAL MEMORANDUM X-647

PRESSURE AND HEAT-TRANSFER MEASUREMENTS ON A MERCURY CAPSULE MODEL*

By John O. Reller, Jr., and H. Lee Seegmiller

SUMMARY

Convective heat-transfer rates, surface pressures, and schlieren and shadowgraph pictures of the flow about the body have been obtained for the re-entry configuration of the Mercury capsule. Tests were conducted in the air streams of four separate facilities and were arranged to provide complementary information on the effects of Mach number, Reynolds number, and stagnation enthalpy. The experimental results have been correlated and are compared with theoretical estimates of local pressures and heat-transfer rates. Visual evidence of the pattern of flow over the capsule is related to the experimental measurements and both are used to indicate regimes of attached or separated flow.

Test results were obtained at angles of attack from 0° to 10° for Mach numbers from 3.4 to 14.7 and stagnation enthalpies up to 5000 Btu per pound. Heat-transfer rates at the stagnation point of the nose (heat shield) for zero angle of attack agree with theoretical estimates which are based on measured pressure distributions. The distribution of heating rates over the heat-shield surface develops a substantial asymmetry with increasing angle of attack. Heat-transfer rates over most of the afterbody were less than 10 percent of the stagnation heating rate. In some cases, however, the effects of flow separation were such that values up to 40 percent of the stagnation heating rate were encountered. The magnitude of these heating rates can be estimated from measured pressure distributions if the nature of the flow, whether attached or separated, is known. It appears that similar estimates for high-enthalpy conditions would have to take into account the effects of any chemical nonequilibrium in the local flow.

---

*Title, Unclassified

[redacted]

INTRODUCTION

Aerodynamic heating is a basic consideration in the design of a vehicle which is to be capable of entering the earth's atmosphere from a circular orbit and landing intact on the surface. In particular, some protection is required to provide the vehicle with both structural integrity and a suitable internal environment. One approach to the heat protection problem is to present a large and relatively flat surface normal to the approaching air and to keep remaining body surfaces in the wake region behind this shield. By this means, the convective heating rates in the nose region can be reduced because of the large radius of curvature, although the heating load is spread over a large surface area, while afterbody surfaces may be shielded by immersion in a separated flow of relatively low density. The Mercury re-entry capsule, as originally proposed by Faget, Garland and Buglia (ref. 1), is one configuration of this general type.

The accurate estimation of afterbody heating for such vehicles is hampered, unfortunately, by a lack of knowledge about the behavior of separated flow. Such flows are known to be dependent upon local Mach number, Reynolds number, the nature of the boundary layer, and in the entry situation, upon surface temperature and chemical reaction rates in dissociated air as well. Theoretical studies, such as that by Chapman (ref. 2), have helped to define the basic mechanism of heat transfer in the separated flow of an ideal gas. However, as pointed out by Sprinks (ref. 3), there are at present no suitable theories for application at the temperature level of hypersonic flight, while only a very limited amount of experimental work is available. Thus it is not immediately clear that a given set of measurements of heating rates and pressures, obtained in a small-scale separated flow in an air stream behaving essentially as an ideal gas, can be directly related to the corresponding quantities in the full-scale flight environment. For the case of attached flow over a blunt shape (e.g., ref. 4), it has been possible to show a rather direct correspondence of this type. In the present instance the lack of theoretical basis may be overcome, in part, by an integrated experimental investigation in several complementary facilities, since no one facility can duplicate all the flight conditions. An attempt toward this objective by the correlation of data obtained in several test facilities forms the purpose of the present investigation. The correlations include local convective heat-transfer rates, pressures, and flow visualization data for the afterbody as well as the nose of the Mercury capsule. The reference flight conditions are those for a location in a typical entry trajectory at which the vehicle is traveling at a Mach number of 15 at an altitude of 165,000 feet.

To this end, tests were conducted in an essentially cold-flow supersonic wind tunnel at Mach numbers from 3.5 to 6 with free-stream Reynolds numbers approximating the reference full-scale condition;

[redacted]

DECLASSIFIED

[redacted]

in a hypervelocity shock tunnel at a Mach number of 8.4 with stagnation enthalpy close to the reference value of 5620 Btu per pound; and in a free-flight wind tunnel at Mach numbers from 3.5 to 15 with approximately full-scale Reynolds numbers. In addition, these results are compared with theoretical estimates of local pressures and heat-transfer rates, with extension of such estimates to include the conditions encountered in high-enthalpy flight.

SYMBOLS

A489

A	area, ft^2
C_D	drag coefficient
C_p	pressure coefficient
c_p	specific heat of air at constant pressure, Btu/lb °F
c_w	specific heat of shell material, Btu/lb °F
g	gravitational acceleration, 32.17 ft/sec^2
H	enthalpy, Btu/lb
H_{diss}	enthalpy of dissociation, Btu/lb
H_s	stagnation point enthalpy, Btu/lb
h	convective heat-transfer coefficient, Btu/ft^{2}sec °F
M	Mach number
Le	Lewis number
Pr	Prandtl number
St	Stanton number
p	pressure, lb/ft^2, except as noted
q	dynamic pressure, lb/ft^2
$\dot{q}$	convective heat-transfer rate (or heat-storage rate), Btu/ft^{2}sec
R	Reynolds number or radius of curvature
r	maximum radius of axisymmetric body

[redacted]

S	distance along surface from model axis, ft
S_{max}	distance along surface from stagnation point to base of hemisphere, ft
S'	distance along afterbody surface from edge of heat shield, ft
$\frac{S}{R}$	dimensionless entropy
T	temperature, °R
t	time, sec
V	velocity, ft/sec
W	weight, lb
w	unit weight of shell material, lb/ft^3
Z	ratio of molecular weight of undissociated air to mean molecular weight of gas mixture
α	angle of attack, deg
Δ	shock detachment distance, ft
η_r	temperature recovery factor
θ	ray angle, deg
μ	viscosity coefficient, $lb\text{-}sec/ft^2$
ρ	density of gas, $slugs/ft^3$
τ	model shell thickness, ft
Φ	azimuth angle measured from windward meridian, deg

Subscripts

aft	afterbody
d	maximum diameter of axisymmetric body
e	wall in thermal equilibrium

A
4
8
9

[redacted]

F	chemically nonreacting or "frozen"
l	local inviscid flow
r	adiabatic wall
s	body stagnation point
T	reservoir condition
w	body surface or wall
∞	free stream
2	behind normal shock
*	sonic point

A
4
8
9

TEST FACILITIES

Wind Tunnel

Low-enthalpy tests were conducted in the Ames 10- by 14-Inch Supersonic Wind Tunnel at Mach numbers of 5 and 6. This facility is a continuous-flow wind tunnel that is supplied with dry air at a nominal pressure of 6 atmospheres and a temperature sufficient only to prevent condensation of the test stream. Further details of this facility will be found in reference 5. Test models were sting-supported from the rear. Heat-transfer data were obtained by the calorimeter technique with models precooled with liquid nitrogen. With this system, nitrogen injected into the tunnel reservoir just upstream of the sonic throat cooled the core of the test stream as well as the test model. The control and pressure relief valves were suitable for sharp cutoff of the coolant flow. With this system, it was possible to obtain steady-state model surface temperatures from 100° F to 400° F below local recovery temperatures, depending in part upon the total temperature of the test stream. Test stream conditions, model stagnation conditions, and model size are given in table I.

Shock Tunnels

Tests were also conducted in two hypervelocity shock tunnels. One of these facilities, hereafter referred to as the 2-inch shock tunnel, has a 2-inch square test section and is supplied with dry air at a nominal reservoir pressure of 823 atmospheres and enthalpy of 5410 Btu per pound. This reservoir of high-energy air is created with a tailored-interface shock tube which uses combustion-heated helium as the driver gas. The method used to calibrate the air stream is similar to that used in reference 6. For the present investigation the facility was calibrated with a geometric nozzle area ratio of 315, which for flow in chemical equilibrium, was expected to develop $M_\infty = 5$ in the test air stream. Stream static pressure, pitot pressure, and velocity were measured after the manner of reference 6. These measurements indicated a usable testing time of 2.5 to 3.0 milliseconds. Analysis of the calibration data also revealed that the test stream was probably not in chemical equilibrium. Thus it appears that as a result of the nonequilibrium condition of the nozzle flow, the test Mach number was about 8.4 at a Reynolds number of 1.1×10^6 per foot. Other free-stream and stagnation-point conditions are listed in table I.

A489

The second shock-driven facility, hereafter referred to as the 1-foot shock tunnel, was in calibration at the time of the present tests. The operation of this facility is similar to that of the 2-inch shock tunnel just described. A reservoir of dry air at a nominal pressure of 260 atmospheres and an enthalpy of 4900 Btu per pound provides a test stream which is represented by the conditions listed in table I. A single test was made with the Mercury capsule configuration in this tunnel to obtain a schlieren photograph of the flow about the model. Data from this photograph are used herein.

Test models were sting-supported from the rear. A visual record of the flow about models was obtained with a spark-discharge schlieren system and by photographing the luminous gas behind the bow shock wave.

Free Flight

A number of free-flight tests of the Mercury capsule shape were conducted in the Ames Supersonic Free-Flight Wind Tunnel. In this facility models are gun-launched upstream through the test stream of a supersonic wind tunnel. Reference 7 presents the details of the arrangement, operational technique, instrumentation, and model design for this facility. The data obtained consist of shadowgraph pictures of the flow about the models at known flight conditions. These flight conditions and the corresponding stagnation-point values are listed in table I.

[redacted]

MODELS AND INSTRUMENTATION

Wind Tunnel

Sketches of the models used to obtain heat transfer and pressure distributions in the low-enthalpy wind-tunnel tests are shown in parts (a) and (b) of figure 1. Both models had the modified shoulder configuration shown. The heat-transfer model consisted of a metal support frame over which a thin outer skin of stainless steel was spotwelded. Thermocouple locations and tabulated skin thicknesses are shown on figure 1(a). Copper-constantan thermocouples were located as far as possible from the frame members to minimize conduction effects. The number 40 gage wires were inserted into separate holes in the skin and were attached with small amounts of silver solder. Thermocouple signals were first amplified and then recorded on an oscillograph. The pressure model is shown in figure 1(b). Afterbody orifices were located to provide surface pressure information at all positions for which heating rates were measured and at several other points in addition. Pressures were measured with conventional mercury and dibutyl U-tubes.

Surface finishes of RMS 10 (25 microinches) were specified on both model noses, while afterbody surfaces were to be RMS 16 or better. The former finish is obtained by polishing with progressively finer grit down to a number 600 paper. No controlled measurements of the quality of surface finish were made on the completed models. No apparent deterioration of surface finish was observed during the test program.

Shock Tunnel

Sketches of the heat-transfer and pressure models used for the high-enthalpy tests in the 2-inch shock tunnel are shown in parts (c), (d), and (e) of figure 1. Note that the shoulder configuration has been simplified to a square corner on these models. The heat-transfer model was designed from preliminary estimates of flow time and local heating rates. Calculations showed that it was feasible to use the calorimeter technique of measurement for the short duration flows of this facility. The calorimeter element at the stagnation point was copper 0.010 inch thick with a relatively small iron-constantan thermocouple fastened to the inner surface. The element for the afterbody was 0.005 inch thick and was formed from the lower half of a butt-welded iron-constantan thermocouple cemented into a groove normal to the flow direction. Additional details are shown in figures 1(c) and 2(a).

A sketch of the model used to measure afterbody pressures is shown in figure 1(d). The model was made of stainless steel and housed two diaphragm-type pressure transducers. These units were designed to measure

[redacted]

small differential pressures with spirally wound strain-gage elements, one of which was mounted on each face of the diaphragm. The double-gage diaphragm was found to be relatively insensitive to temperature changes, compared to a single gage unit. The stagnation pressure model, shown in figure 1(e), used a piezoelectric pressure transducer mounted in the model support.

A photograph of a heat-transfer model installed in the removable test section is shown in figure 3. The nozzle exit can be seen at the left and the model-support wedge at the right. Model surface finishes were specified to be less than RMS 10 for each test and, because of abrasion of the model nose which occurred during the blowdown following the test period (see fig. 2(b) for example), the nose cap was repolished or replaced after each run.

Free Flight

Two sets of models were used in the present free-flight tests. The first set consisted of models 1.65 inches in diameter made of titanium, while those of the second group were 0.45 inch in diameter with a body of aluminum and a nose cap of phosphor bronze about 0.08 inch thick. The models were not instrumented but were used to obtain shadowgraph pictures of the model flow fields. The larger models were tested at Mach numbers from 3 to 5; the smaller, from $M = 6$ to 14.7. The shape was the same as those tested in the wind tunnel (figs. 1(a) and 1(b)) except for the shoulder region which did not have the flattened corner and for a threaded section behind the canister, which was necessary for launching. Model surface finishes were in all cases as good as previously quoted or better; carefully polished surfaces on the small models often had finishes better than RMS 5.

REDUCTION AND ACCURACY OF DATA

Reduction of Wind-Tunnel Data

The heat-transfer data in the wind tunnel were obtained as an oscillograph record of the temperature history of local elements of the skin of a precooled model, while the model was being heated by the tunnel air stream. The temperature-rise rate of an element of skin was converted to heat-storage rate with the familiar equation

$$\dot{q} = \tau w c_w (dT/dt) \qquad (1)$$

[redacted]

where τ, w, and c_w are properties of the skin material. Skin thickness τ was determined on the polished model prior to thermocouple installation; unit weight w was assumed constant. The specific heat c_w and its variation with temperature were assumed to be the same as for AISI type 347 stainless steel which has a nearly identical composition. Information on specific heat was taken from reference 8 and is shown in figure 4. The last term in equation (1) can be derived from an oscillograph record in a number of ways. In the present instance, the slope of a trace was read at the earliest time consistent with the establishment of a steady heat-input situation, as illustrated in figure 5. Figure 5(a) shows the variation of heat-storage rate with wall temperature for a thermocouple on the heat shield where the rate is relatively high, and part (b) shows a similar variation at a low heating-rate location on the conical afterbody. If it is assumed that the local convective heat-transfer coefficient is constant for the range of temperatures encountered, measured heating rates should fall on a straight line which intersects the axis at the adiabatic wall or recovery temperature. This result follows from the basic definition of convective heat-transfer coefficient, h, in the equation

$$\dot{q} = h(T_r - T_w) \qquad (2)$$

where T_r is the local recovery temperature. If heat loss or gain by conduction and radiation is negligible, the measured equilibrium wall temperature, T_e, will be equal to T_r. This was assumed to be the case in the present investigation. It can be seen in the lower portions of figures 5(a) and 5(b) that part of the measured data does fall on such a line in each case. The resultant coefficients are shown in the upper parts of the figure. The deviation of the data in the low-temperature region is attributed to a lag in stream total temperature following coolant shutoff (a basic weakness of this system), while that in the high-temperature region is believed to result from lateral conduction within the model shell. Between these limits the data are representative of steady-state convective heating, at least to the accuracy of the present investigation.[1]

The stagnation point heating data have also been presented in **dimensionless form as** Stanton numbers

$$St = \frac{h}{g(\rho V c_p)_2} \qquad (3)$$

---

[1] A small semiempirical correction has been applied to some of the heat-shield data to account for lateral conduction. In several runs a wall temperature gradient resulted from a nonuniformity in the cooled core of the test stream. It is furthermore tacitly assumed that the cooler model surface that exists during heating-rate measurements does not appreciably alter boundary-layer development or the afterbody flow field or, thus, the effective T_r.

where density, velocity, and specific heat are evaluated for conditions behind the normal shock wave. Other data are presented as the ratio h/h_s, where h_s refers to model stagnation point conditions at zero angle of attack.

Reduction of Shock-Tunnel Data

Air stream calibration.- As was stated earlier, the investigation in the 2-inch shock tunnel was to be conducted at the same Mach number as the wind-tunnel tests, namely, $M_\infty = 5$. To accomplish this plan, it was first necessary to calibrate the test stream. This was carried out with the techniques discussed in reference 6. With the assumption that the flow was in chemical equilibrium, the calibration indicated that a test stream of approximately the desired Mach number had been obtained. Subsequent to the completion of the present program, it was found that the calibration results could be reduced by another and more general method which allows for the possibility of chemical nonequilibrium in the test stream. A summary of the analysis and results of the two methods is given in appendix A. When the nonequilibrium effects are considered, the stream Mach number in the 2-inch shock tunnel is indicated to be 8.4; this value and the corresponding nonequilibrium conditions were used in the reduction of the present data.

A similar flow situation may, to some extent, also exist in the test stream of the 1-foot shock tunnel. At present, however, this question has not been resolved so that for the purposes of this report the test stream in the 1-foot facility is assumed to be in chemical equilibrium.

Chemical equilibrium in model flow field.- The departure from chemical equilibrium of the test stream of the 2-inch shock tunnel implies that a similar condition may exist in the flow about models. An analysis of this situation is given in appendix B. It was found in this analysis that the gas flow behind the bow shock wave should be either in equilibrium or close to the equilibrium condition as it reaches the stagnation point of the body. Similarly, the inviscid flow approaching the corner of the heat shield is indicated to make only a small departure from chemical equilibrium. On the other hand, the inviscid flow over the afterbody is indicated to be well into the frozen flow regime. Thus it is possible that data measured on the afterbody may in some manner show the effects of a local flow that is not in chemical equilibrium.

Reduction of heat-transfer data.- Heat-transfer data were recorded by photographing an oscilloscope trace. The temperature-rise rate of the calorimeter element was converted into heat-storage rate with equation (1), as before, with the indicated dT/dt read at the earliest time consistent with the establishment of steady flow in the test section. Unit weight w and specific heat c_w were assumed constant, while the mass of the calorimeter element was determined by direct measurement of sectioned models after each run. Radiant heat transfer from the shock-heated gas cap to the model was estimated from charts derived from reference 9 and was found to be negligible. Radiant heat flux from the model to the tunnel walls was also negligible. Transverse temperature gradients in the calorimeter elements were calculated and found to have no appreciable effect on the measured data. Lateral conduction effects were estimated and are included in the over-all estimate of accuracy shown later.

Stagnation point heating rates are presented as Stanton numbers based on enthalpy potential. Thus,

$$St = \frac{\dot{q}_s c_{p_2}}{(H_s - H_w)(\rho V c_p)_2 g}$$

where again the gas properties are referenced to conditions behind the normal shock wave. Heat-transfer rates measured at locations other than the stagnation point are presented as the ratio of the local value per unit surface area to that at the stagnation point to avoid the necessity of estimating local recovery enthalpies.

Since both heating-rate measurements in the shock tunnel and estimates from existing theories for full-scale conditions at locations downstream of the body stagnation point are most readily available in the form $\dot{q}/\dot{q}_s$, it is necessary to consider the relationship between these values and low-enthalpy wind-tunnel data in the form h/h_s. Note first that at high-enthalpy conditions it can generally be assumed that $T_w \ll T_r$ (or T_s) and therefore $H_w \ll H_r$ (or H_s), so that the expression $\dot{q}/\dot{q}_s = (h/h_s)(H_r/H_s)$ is valid for a representative constant value of specific heat. Consider now the variation of enthalpy ratio H_r/H_s in response to real-gas effects. In general the recovery enthalpy H_r can be defined by the relationship $\eta_r = (H_r - H_l)/(H_s - H_l)$, where η_r for the case of a laminar boundary layer is approximated by $(Pr)^{1/2}$ evaluated at a temperature and pressure representative of conditions within the boundary layer.[2] Now, since the Prandtl number Pr is found to be relatively insensitive to temperature over the range of present interest, it can be shown by theoretical calculations that local ratios of H_r/H_s for a short blunt body are only a weak function of M_∞ or H_s, for values of M_∞ of about 5 or greater. This is illustrated in the top part of figure 6, where H_r/H_s is shown as a function of local Mach number in a generalized blunt body flow for two representative test conditions; for an ideal gas at $M_\infty = 5$ (H_s = 160 Btu/lb) and for a real gas at $M_\infty = 22$ (H_s = 10,700 Btu/lb) in a typical entry trajectory. The latter calculations were made with the normal shock equations, a modified Newtonian pressure distribution, and the gas properties of reference 10. The two curves agree within 5 percent for local Mach numbers up to about 4 and indicate that, as a first approximation, low-enthalpy wind-tunnel data for blunt shapes might be compared with high-enthalpy results when in the form $\dot{q}/\dot{q}_s = (h/h_s)(H_r/H_s)$. In effect, the "cold wall" assumption ($H_w \ll H_r$) is applied to the wind-tunnel results.

---

[2] A similar argument can be advanced for the case of a turbulent boundary layer.

[redacted]

The second term in this comparison, namely, the ratio of heat-transfer coefficients, h/h_s, must also be considered. As a first guess the low- and high-enthalpy h/h_s distributions around a blunt body might be assumed to be similar. Intuitively, this assumption of similarity would be most closely satisfied in those regions where the local surface pressures can be described by the Newtonian approximation. In other areas the local pressures and, as a result, the local heating rates will no doubt be dependent to some extent on M_∞ and H_s. Thus, it is indicated that both M_∞ and real-gas effects on local h/h_s ratios are such as to limit the direct comparison of $\dot{q}/\dot{q}_s$ ratios to those surfaces with substantial inclination to the free-stream direction. With this thought in mind then, the validity of one further simplification will be discussed. It is suggested that for such inclined surfaces, the ratio H_r/H_s be dropped from the expression $\dot{q}/\dot{q}_s = (h/h_s)(H_r/H_s)$ as applied to low-enthalpy results, and that low-enthalpy h/h_s ratios be compared directly to high-enthalpy $\dot{q}/\dot{q}_s$ ratios. Again in the top part of figure 6 the error introduced by this simplification is seen to be less than 10 percent (local H_r/H_s as compared to unity) at local Mach numbers up to 3.5, and not more than about 5 percent within the prior limitation of substantial surface inclination. Furthermore, the low-enthalpy numbers will be conservative since the neglect of H_r/H_s should lead to overprediction of local heating rates relative to high-enthalpy results. A sample comparison of this type is shown in the lower part of figure 6 where, for a hemispherical shape, experimental results from reference 11 are compared with the theory of reference 12. In this case the experimental variation of heating rate with distance from the stagnation point actually falls below the theory at first, but then rises above it as the shoulder is approached and the flow enters a region where the magnitude of the local pressures is no longer accurately defined by the Newtonian model.

Within the framework of this simplified analysis, then, two conclusions can be drawn with regard to the present investigation. First, the ratio of local to stagnation point heating on the nose of the capsule configuration should be insensitive to either M_∞ or H_s, at least so long as $M_\infty \geq 5$. Thus, since this surface is steeply inclined to the free-stream direction, a low-enthalpy h/h_s ratio for the nose should be closely comparable to the corresponding $\dot{q}/\dot{q}_s$ at high-enthalpy conditions. Second, the afterbody heating-rate ratios are probably a function of both M_∞ and H_s. Therefore, low-enthalpy results for the afterbody are not directly applicable to a high-enthalpy environment.

Collected Flow Visualization Data

Shadowgraph pictures of flow about the model were obtained during the tests in the wind tunnel at Mach numbers 3.5, 4.0, 5.0, and 6.0 for angles of attack of 0° and 10.6°, with the model surface at essentially recovery temperature. The corresponding test stream and model stagnation conditions are shown in table I, while a representative set of pictures is shown in figure 7. At some test conditions the airflow over the afterbody was sufficiently dense that a photographic record of the boundary layer or the separated flow region was obtained; at other conditions the local density gradients were below the limit that could be resolved by the optical system. Therefore, to increase the usefulness of the visual data, an attempt was made to correlate the shock-wave pattern over the afterbody (which remains visible to lower density levels) in such a manner that this shock pattern could be used to indicate whether the afterbody flow was separated or attached. It was found that afterbody flows could be divided roughly into three regimes:

A489

1. Attached flow: This regime is characterized by a strong trailing shock wave which extends to the surface at the intersection of the cone and cylinder, and a weak shock wave just behind the corner which stands at about the local Mach angle from the conical surface.

2. Separated and reattached flow: In this regime the flow separates at the corner and reattaches at some downstream location. Reattachment on the cone may give rise to a separate shock wave, or to a wave which coalesces with the trailing shock wave. The corner wave moves out from the surface to allow for the thickness of the separated region and the reduction in local Mach number. The trailing shock wave loses definition in the vicinity of the body.

3. Separated flow: This flow field is identified by flow separation at the corner, a widely distended corner wave and a weak trailing shock wave that is far removed from the body.

It is obvious from the general nature of these definitions that many intermediate flow situations will occur. However, it is believed that the listed characteristics are descriptive of the range of conditions that will be encountered.

Figure 8 presents two schlieren pictures and one self-luminous "glow" picture taken during the investigation in the shock tunnel; figure 9 presents a series of shadowgraph pictures taken in the free-flight facility at approximately the same stream Reynolds number and for Mach numbers from 3.4 to 14.7.

[redacted]

Accuracy of the Results

The estimated accuracy to which the gas properties in the reservoir and test stream of the shock tunnel are known are compared with similar values for the wind tunnel in the following table:

		10- by 14-inch wind tunnel		2-inch shock tunnel	
Location	Property	Nominal value	Accuracy, percent	Nominal value	Accuracy, percent
Reservoir	Pressure, psia	72.0	±0.5	[1]12100	±5
	Temperature, °R	665	±0.3	[2]12960	±4
	Enthalpy, Btu/lb	159	±0.3	[2]5410	±4
Stream	Static pressure, psia	0.158	±2.4	[1]0.81	±20
	Pitot pressure, psia	5.31	±1.3	[1]74.0	±4
	Total enthalpy, Btu/lb	159	±0.6	[2]5000	±6
	Velocity, fps	2575	±0.4	[1]14390	±6
	Mach number	5.03	±0.4	[2]8.40	±9
	Reynolds number/ft	3.54×10^6	±4.5	[2]1.10×10^6	±15

[1] Measured values.
[2] Computed values.

[redacted]

The estimated accuracy of the measured pressures and heat-transfer rates are shown in the following table:

	10- by 14-inch wind tunnel		2-inch shock tunnel	
	Range	Accuracy, percent	Range	Accuracy, percent
Heat-transfer coefficient, Btu/ft^{2}sec °F	0.00015 to 0.0015	±23 to ±16	---	---
	0.0015 to 0.015	±16 to ±8	---	---
Heat-transfer rate, Btu/ft^{2}sec	---	---	20 to 100	±25
	---	---	1500 to 2500	±10
Surface pressure, psia	0.05 to 0.50	±6 to ±3	1.0 to 2.0	±25
	0.50 to 5.0	±3 to ±2	70 to 80	±4

The above estimates of accuracy should be interpreted as approximate limits on the physical measurements. It should be recognized, however, that the shock-tunnel results are relatively less precise than indicated when reduced to coefficient form for a given set of stream conditions, simply because the test stream itself cannot be accurately defined within the framework of existing measurements.

RESULTS AND DISCUSSION

The results of this investigation are presented in graphical form in figures 10 through 24. Figures 10 through 14 present results for the stagnation region and the heat-shield surface, figures 15 through 23 cover the conical afterbody and parachute canister, and figure 24 deals with the problem of afterbody flow separation. The discussion will, in general, follow this same order and, with the exception of the stagnation region of the heat shield, will consider the measured pressures and their relation to theory prior to the analysis of the convective heat-transfer results.

[redacted]

Stagnation Region

Convective heat-transfer rates to the stagnation point of the heat shield for the capsule at $\alpha = 0^{\circ}$ are presented in figure 10. Measured data are shown as open symbols, with each point representing the average of at least two independent measurements. The cross-shaped symbols represent estimated stagnation heating rates obtained with the theory of reference 13, which has been applied both for the test conditions of the present investigation and for typical flight conditions. The expression

$$\dot{q}_s = 0.763\left\{(\rho\mu)_w^{0.1}(\rho\mu)_s^{0.4}\left[1 + (Le^{0.52} - 1)\frac{H_{diss}}{H_s}\right]\left(\frac{H_s - H_w}{Pr^{0.6}}\right)\left(\frac{dV}{dS}\right)^{0.5}\right\} \tag{5}$$

is the relationship found in reference 13 between the local flow conditions and gas properties and the convective heating rate at the stagnation point of an axially symmetric body. Note that this expression can accommodate both ideal and real gases and can be used to determine the effects of body surface temperature. For these reasons the theory is attractive for the present investigation since one purpose is to relate low-enthalpy wind-tunnel results to data for high-enthalpy test conditions and to flight estimates. In the present application, the last term in equation (5) is used to account for the difference in velocity gradient at the stagnation point of the Mercury capsule as compared to that which would be predicted for a simple hemisphere with a Newtonian pressure distribution. From measured pressure distributions (e.g., ref. 14), the gradient for the capsule has been found to be about 27 percent greater than for a simple hemisphere; thus, the heating rate as predicted by equation (5) should be about 13 percent greater.

The results are presented in the form of Stanton number as a function of Reynolds number in figure 10(a). As noted on the figure, the various parameters are referenced to conditions behind the normal shock wave. In consideration of this figure it is important to recognize that the quantitative results depend upon the evaluation of the various gas properties. In the present investigation, model stagnation conditions for both the wind tunnel and shock tunnel were obtained from the results of the air stream calibration. For the free-flight test, the known stream conditions and model velocity were used with the equations of motion and the charts of reference 15 to compute the stagnation conditions. For full-scale conditions, a shallow entry trajectory from a 100-mile orbit was computed for the nonlifting capsule with a W/C_DA of 45 pounds per square foot. In the determination of this trajectory, the model atmosphere of reference 16 was used. Again the stagnation properties

[redacted]

of the real gas were computed with the aid of reference 15. With the stagnation conditions known, then, the thermodynamic and transport properties of the real gas were evaluated from reference 10.

It can be seen in figure 10(a) that the data from the low-enthalpy wind tunnel for Mach numbers of 5 and 6 are in close agreement with the theoretical estimates. These estimates are shown on the figure by cross symbols and were obtained from equation (5), in which, of course, the enthalpy of dissociation has gone to zero. The wind-tunnel data serve to define the solid line on the figure which passes through the theoretical estimates for the free-flight tests at $M_\infty = 3.4$ and 5.3. This line has been drawn to express the well-known relation that $St\sqrt{R}$ is a constant. This line, then, represents the low-enthalpy, ideal-gas, stagnation-point heating for the configuration. It is noted, however, that both the experimental and theoretical results for higher enthalpies depart from this line in an apparently consistent manner. For example, both the data point from the shock tunnel at an enthalpy of about 5000 Btu per pound and the corresponding theoretical estimate are some 35 percent above the ideal-gas line. This difference is apparently not due to surface temperature effects since the theory of reference 13 indicates that this effect influences the present results by less than 5 percent for the range of surface temperatures of the present investigation. More properly these differences would appear to reflect the variations in gas properties, such as those due to dissociation, with increasing enthalpy.

To evaluate this apparent enthalpy dependence, the results have been converted to the parameter, $St(R_d)_2^{1/2}(Pr)_2^{2/3}$ and are shown as a function of enthalpy in figure 10(b). The Prandtl number has been introduced to obtain a parameter that is consistent with the general form of Reynolds analogy. Estimates for a second entry trajectory are also shown. The heating parameter shows a relatively weak dependence on enthalpy and the single curve appears to correlate the stagnation-heating rates, at least up to satellite enthalpy levels, within about ±5 percent. It is believed that this 5-percent scatter results, in large part, from the uncertainty in present knowledge of the transport properties of gases. This correlation supports results presented earlier in reference 4, thus reaffirming the conclusion that it should be possible to predict the basic convective heat transfer to the stagnation point ($\alpha = 0^\circ$) of the full-scale version of this configuration with reasonable accuracy, at least in the continuum flow regime.

Heat Shield

Pressure distribution.- Local pressures on the heat shield, ratioed to body stagnation pressure, are given as a function of surface distance from the body axis in figure 11. Data for the windward and leeward

[redacted]

meridians at angles of attack of 0°, 5°, 10°, and 15° are shown. The pressure variations in this figure are, for the most part, illustrated by results obtained from references 14, 17, 18, and 19 since the present results are limited to measurements on the model axis at irregular angles of attack. Although these results are not presented here they do substantiate the variations shown in the figure. In figure 11(a) the data for $\alpha = 0^\circ$, for which the test Mach number varies from 1.6 to 20.1 and the stagnation enthalpy from about 130 to 1900 Btu per pound, are well represented by the solid faired curve. A pressure distribution obtained with the use of Newtonian theory is shown as a dashed curve. The experimental results show that downstream of the stagnation point the pressures are lower than are predicted for this spherical surface; hence the corresponding local velocities are higher. These differences are attributed to the effects of the expansion at the edge of the shield. Since the local flow is subsonic, these effects influence the entire region behind the shock wave. As noted earlier, these differences indicate increases in the velocity gradient and hence the heating rate at the stagnation point.

When the capsule is inclined at some angle of attack, the situation becomes a bit more complex. Due to the effects of the edge of the heat shield, the stagnation point appears to shift to a location other than that specified by geometric considerations. This shift is shown by results at $M_\infty = 6.9$ given in reference 19 and reproduced in figure 12 herein. In this reference oil-flow patterns were obtained at $M_\infty = 6.9$ and it was found that the angle between the radial line containing the actual stagnation point and the capsule center line was about 20 percent less than the angle of attack for α between 5° and 20°. Stagnation points located by this criterion and pressure data for $\alpha = 5^\circ$, 10°, and 15° (windward and leeward meridian only) are shown in figures 11(b) through (d). In each case, a Newtonian distribution centered on the geometric stagnation point is also shown as a reference curve. The results are similar to those for $\alpha = 0^\circ$. For example, the pressures obtained with Newtonian theory are higher than the experimental results, particularly on the windward side of the stagnation point. The good agreement among the data from the several sources indicates that these distributions are basic to the configuration and are in all likelihood applicable to the full-scale vehicle. Unfortunately, however, the results shown in figure 11 also imply that the heat transfer may be difficult to predict and that it may vary substantially with angle of attack.

Heating-rate distribution.- Heating-rate distributions on the windward and leeward meridians of the heat shield are presented in figure 13 as the ratio of local heat-transfer coefficient to the stagnation-point value at $\alpha = 0^\circ$. This ratio, as discussed earlier, should be closely comparable on this highly inclined surface to the ratio $\dot{q}/\dot{q}_s$, $\alpha = 0^\circ$ used at high-enthalpy conditions. Measured values from the present investigation are augmented by data for $M_\infty = 9.6$ from reference 19. (Note that the effect of stream Mach number can be shown

[redacted]

to be sufficiently small to be neglected in this comparison.) For $\alpha = 0^\circ$ (fig. 13(a)), the heating-rate distribution obtained in the wind tunnel agrees with that predicted with the theory of reference 12. This theory makes use of the cold-wall assumption and, as used here, it is employed with a pressure distribution of the Newtonian form. This agreement between the experimental and theoretical results is perhaps fortuitous in view of the departure of measured pressures from the Newtonian distribution with the corresponding increase in heating level at the stagnation point. In any event, it would seem that the heating-rate distribution is relatively insensitive to the observed pressure differences, at least at $\alpha = 0^\circ$. Also shown in this figure is a similar distribution, from the theory of reference 20 for the conditions of $M_\infty = 15$ in the forementioned nonlifting entry trajectory. In this case the calculations were based on the pressure distribution of figure 11. The substantial agreement between these theoretical flight results and the previous experimental results indicates the relevance of low-enthalpy data in the prediction of heating rates for this blunt face of a full-scale vehicle.

In figure 13(b) heating-rate distributions are shown for angles of attack up to about 10°. Appreciable changes in the heating pattern, particularly on the windward side of the heat shield, result from the variation in local flow properties at these relatively small angles of attack. In particular, the region of maximum heating appears to move to the windward edge of the shield. It would seem that this behavior is typical for the configuration at least when the boundary-layer flow is laminar.

The variations of heating rate with azimuth angle for two distances from the axis as given by the ratio S/r are shown in figure 14. Representative curves have been faired through some of the data to illustrate the trends. The results are generally as would be expected, with an "inclined-cylinder" type of distribution developing with increasing distance from the origin of flow.

By way of summary, then, the heating rates on the shield appear to fall into an understandable pattern. This pattern reflects the influence of the expansion from subsonic to supersonic flow about the corner at the edge of the heat shield. The expansion has a surprisingly large effect on local pressures and thus on heat-transfer rates over the entire shield surface as well.

Afterbody

Longitudinal pressure distribution.- Pressure data for the afterbody are presented in figure 15 as a function of surface distance along a meridian line from the edge of the heat shield. Several theoretical estimates are also shown. As shown in figure 15(a), the pressures measured on the conical surface at $M_\infty = 5$ and $\alpha = 0^\circ$ are almost constant over the surface. Although the pressures are less than the stream static pressure, they are somewhat in excess of the theoretical estimates. One such estimate is shown as the solid line at $C_p = -0.0435$ in the left side of the figure. This line indicates the pressure level that would be reached if the flow at the edge of the heat shield were expanded two-dimensionally through the angle bounded by local sonic flow conditions, on the one side, and by the conical surface of the afterbody on the other side. To fix the size of this expansion angle it was assumed, in effect, that sonic conditions were reached when the flow from the stagnation region had turned 45° to the free-stream direction in the expansion at the edge of the heat shield.[3] The resultant expansion angle at $\alpha = 0^\circ$ is therefore 65°. This theoretical estimate corresponds to a limiting case of attached afterbody flow and, as such, will provide a lower limit of the pressures possible in an ideal-gas flow. By comparison, then, the measured pressures indicate that the flow is separated over this surface; this result agrees with the visual evidence of figure 7(a).[4] This rather simple method for estimating pressures on the conical part of the afterbody does not, of course, account for any three-dimensional flow effects. As a first step, these effects might be considered by use of the second-order shock-expansion method of reference 21 to estimate the surface-pressure gradient downstream of the corner expansion. Results obtained in this manner are shown in the left side of figure 15(a) as a dashed line; this estimate was obtained with the additional assumption that the gradient is constant along the conical surface. It appears that the three-dimensional flow effects are relatively small for these conditions and the estimates do not give results in conflict with the evidence for flow separation discussed earlier.

The pressure level on the cylindrical section at $\alpha = 0^\circ$ is somewhat higher than that on the cone, although much less than either the two-dimensional or the three-dimensional estimate for attached flow. This observed pressure rise on the cylinder is perhaps surprising because of the apparent flow separation over the conical surface at this angle of attack. However, there is evidence of a weak trailing shock wave in the shadowgraph picture of figure 7(a) which corresponds to this test condition. Thus, the flow pattern in this region is indicative of a partial reattachment of the flow, at least to the extent that can be inferred from the response of the local flow to the change in body shape. For $\alpha = 10^\circ$, pressures on the leeward meridian indicate separated flow over the afterbody. On the windward side the flow is attached (as the visual evidence of fig. 7(b) shows) with the pressure level and gradient rather well estimated on the cone with the Prandtl-Meyer expansion and the correction from reference 21 (the dashed curve). The pressure level on the cylinder is close to that estimated with the assumption of a conical compression from the theoretical pressure at the cone-cylinder juncture. Insufficient data are available to assess the pressure gradient on the cylinder.

---

[3] This assumption regarding the sonic line, although approximate, has been used to obtain estimates of pressures on the afterbody in the present investigation. It is realized, in fact, that the sonic line is not straight but may have considerable curvature between the shock wave and the body surface. In addition, it should in theory approach the surface nearly normal to the flow just upstream of the sharp corner.

[4] Careful inspection of the original print of figure 7(a) indicated that the flow was separated over the afterbody. The fine details leading to this conclusion have been lost in the reproduction process.

In figure 15(b) a pressure distribution is shown for $M_\infty = 6$, $\alpha = 0^\circ$, and at about one-half the free-stream Reynolds number of the data for $M_\infty = 5$ just discussed. Extensive flow separation is indicated since the level of the measured pressure on the conical section is much in excess of the theoretical estimate. In fact, the flow apparently did not expand much beyond the free-stream direction, as indicated by a comparison of the measured pressures with that estimated for a Prandtl-Meyer expansion of 45°. The differences between these results and the distributions for $M_\infty = 5$ denote a strong influence of Reynolds number on afterbody separation in the range of conditions covered by the present tests.

In figure 15(c) similar data from the shock tunnel are presented along with estimates obtained with the basic theory for two-dimensional flow. Data for $\alpha = 0^\circ$ cover the range shown by the barred symbols, while two points measured at $\alpha = 10^\circ$ are also shown. The theoretical estimate was calculated by the method of reference 22 and represents the Prandtl-Meyer expansion of a real gas in equilibrium. It was determined on the same geometric basis as discussed earlier. The experimental data and the theoretical estimates are in good agreement for $\alpha = 0^\circ$, and this result could be interpreted as an indication of attached afterbody flow. It will be remembered, however, that in an earlier section the likelihood of nonequilibrium flow over the afterbody was discussed. It is possible, therefore, that the present agreement is fortuitous and that the data represent a situation of separated flow on the afterbody with a reduction in pressure level due to a nonequilibrium expansion process. This possibility will be considered further in the treatment of convective heat-transfer measurements in a later section.

Circumferential pressure distribution.- In figure 16 pressure coefficients for $M_\infty = 5$ are presented as a function of azimuth angle, Φ, measured from the windward meridian of the afterbody at five longitudinal stations. Curves have been faired through the data at $\alpha = 10.6^\circ$ to illustrate the trends shown by the results. For angles of attack close to zero, the pressure is essentially constant over the conical surface. For $\alpha = 10.6^\circ$, where the flow is attached on the windward meridian, an interesting pattern develops with increasing distance from the shoulder. At the most forward station the pressures in the lee separated region are slightly higher than at $\Phi = 0^\circ$. As distance S'/r increases, a characteristic crossflow pattern emerges with separation apparently occurring near $\Phi = 90^\circ$. The leeward pressures are fairly constant and only slightly greater than at $\alpha = 0^{\circ}$. Thus, the flow on the afterbody is behaving much the same as for more conventional inclined bodies of revolution.

Real-gas effects on afterbody pressures.- The previous discussion of afterbody pressures has shown that measured surface pressures and pressure gradients appear to be part of a recognizable pattern which can be estimated with fair accuracy if the flow is attached. It is proposed then, to use the same method of analysis to indicate the effect of the enthalpy level of the flow field on afterbody pressures. The results of this analysis for $\alpha = 0^{\circ}$ are shown in figure 17 where the ratio of afterbody pressure to stagnation pressure is given as a function of free-stream Mach number. Mach number, rather than stagnation enthalpy, has been used as the independent variable to separate the results into several groups and to facilitate the discussion. The dashed curves represent theoretical results obtained for real-gas Prandtl-Meyer expansions (wherein chemical equilibrium is maintained) to the afterbody surface at the corner of the heat shield. The enthalpy level at any Mach number is specified, by implication, in terms of the static temperature level of the free stream. Curves are shown for stream temperatures of 100° R, 400° R, and 1200° R, which roughly correspond to wind-tunnel conditions, to flight conditions, and to the shock tunnel conditions of the present investigation, respectively. The solid curve shown in figure 17 is a reference curve which represents the variation of the ratio of free-stream to body-stagnation pressure with Mach number. This variation is the result of real-gas calculations which show that the ratio p_{∞}/p_s is only slightly affected by enthalpy level. The most important feature of the theoretical results is the apparent increase of afterbody pressure level with increasing enthalpy (Mach number). This finding implies, for example, that a pressure measured in a wind tunnel at $M_{\infty} = 5$ would underestimate, by a factor of 3, the pressure predicted at $M_{\infty} = 15$ in flight. In a similar manner a pressure measurement in the shock tunnel used in the present investigation overestimates the predicted afterbody pressure in flight at the same Mach number by virtue of the relatively higher static temperature of the stream. Thus within the limitations of this analysis it is indicated that pressure measurements on an afterbody configuration of this type in ground-based facilities are not, in general, directly applicable to flight conditions, even in the most simple case of attached flow in chemical equilibrium.

The experimental results from the present investigation and from references 14, 17, 18, 19, and 23 shown in figure 17 apply to the forward half of the conical surface as shown in the sketch. In general, the data are represented by a bar which indicates the range of pressures that was measured. Note that the curve for attached afterbody flow at $T_{\infty} = 100^{\circ}$ R is a good lower limit for the data from the various wind tunnels. (Higher measured pressures are indicative of flow separation.) This curve crosses the static-pressure curve at $M_{\infty} = 9.5$ and indicates that afterbody pressures will exceed the stream pressure at Mach numbers above this value.

Variation of afterbody pressures with angle of attack.- Pressure coefficients at several longitudinal stations on the windward and leeward meridians of the afterbody are shown as a function of body angle of attack in figure 18. Experimental results are compared with theoretical estimates for attached flow on the conical section, based on the two-dimensional form of the simplified analysis that was introduced in figure 15. The several parts of figure 18 are arranged in order of increasing Mach number and with the aid of results from references 14 and 18 cover the range from $M_\infty = 1.6$ to $M_\infty = 20$. Theory and experiment are in fair agreement both in trend and in magnitude on the windward meridian of the cone at the larger angles of attack and at the higher Mach numbers. The agreement is taken to indicate that the local flow is attached. At the smaller angles of attack and on the lee side of the body the agreement is not so good and, when combined with the available photographic evidence of the flow patterns, indicates that the afterbody flow is generally either partly or wholly separated. Measured pressures on the conical surface are in excess of theoretical predictions. The cylindrical portion of the afterbody is unique in that very substantial pressures can occur on this surface when the flow over the cone is apparently separated (see the windward meridian at α from 0° to 10° in fig. 18(b)). As mentioned earlier, this situation is indicative of flow reattachment on the cylinder and is thought to be related to the prior transition of the free boundary at the edge of the separated region as illustrated at $M_\infty = 4.0$ in figure 7(a). One additional feature of importance is shown in figure 18, namely, that the flow over the afterbody approaches attachment with increasing Mach number. Figures 18(a), (b), (c), and (e) illustrate this point, since the stream Reynolds number is about the same in all cases, while the Mach number increases from 1.6 to 6.0. At present this effect is not clearly understood.

To summarize these results briefly, it appears feasible to analyze the flow field in the region of this afterbody configuration and to account for many of the observed pressure variations. However, the analysis depends on a prior knowledge of flow separation which, even for wind-tunnel results, is difficult to predict in advance. The prediction, therefore, of the occurrence of flow separation in the high-enthalpy flow associated with a full-scale vehicle would be even more uncertain.

Longitudinal distribution of heat-transfer rates.- Longitudinal variations of heat-transfer coefficient along the windward and leeward meridians of the afterbody are presented in figure 19 for $M_\infty = 5$ and 6. The experimental results are compared with theoretical estimates obtained with the methods of references 24 and 25. For the laminar boundary-layer estimates, local Reynolds numbers are based on the length of run from the geometric stagnation point and the surface pressures are those shown in figure 15 for the appropriate theory for three-dimensional flow. For $M_\infty = 5$ and $\alpha = 0^\circ$, the experimental results indicate that the heating rates on the conical surface increase with increasing distance. This trend is opposite to that predicted for attached laminar flow but the level is similar (about 5 percent of the stagnation value). Estimates for laminar separated flow from the theory of reference 2 are also shown. This method indicates heat-transfer rates in a laminar separated region that are about one-half the value for attached flow. The results obtained with this theory indicate better agreement with the experimental results only at the most forward station, $S'/r = 0.43$. In addition, since the theories for either attached or separated flow indicate decreased heating rate with increased distance, the experimental results which show the opposite trend are interpreted to mean a separated flow region for which the free boundary is in a transitional state. An investigation of this phenomenon is reported in reference 26.

The variations in heating rate on the conical surface at $\alpha = 1^\circ$ and 2° are similar to those for $\alpha = 0^\circ$. It is noted, however, that the leeward heating rates increase more rapidly with angle of attack than those on the windward side. For example, for $\alpha = 2^\circ$, lee-side rates are about double those at $\alpha = 0^\circ$. This behavior is thought to result from the transitional nature of the separated flow and is also evidenced by unusually high recovery temperatures at this test condition. For α of the order of 10° windward heating rates are about 10 percent of the stagnation value, while leeward values drop again to about the $\alpha = 0^\circ$ level.

On the cylindrical section at small angles of attack the measured rates at one location are about one-fourth the stagnation point value. This rate is much above the prediction for attached laminar flow. For example, the theory indicates a heat-transfer coefficient for laminar flow of about 0.001, a value substantially less than that measured at $\alpha = 0^\circ$. For this reason the possibility of a reattached turbulent flow is indicated. The predicted rate at $\alpha = 0^\circ$ agrees with the measured value if turbulent flow is assumed to originate at $S'/r = 1.5$ and the local pressure is that for a conical compression from the three-dimensional pressure level for attached flow on the cone.

Results for $M_\infty = 6$ are similar to those for $M_\infty = 5$, and are shown in figure 19(b). The measured heating rate on the cylinder is high, particularly in view of the pressures measured at this Mach number. These pressures were nearly constant over the entire afterbody. The level of heating rate is again taken to mean at least a partial reattachment of the flow with a turbulent boundary layer on the cylindrical section.

One final point will be made concerning the longitudinal distribution of heat-transfer rate. The prevalence of separated flow and its apparent transitional nature at the Reynolds numbers of the present investigation raise the question of whether afterbody heating rates might not be sensitive to cooling of the boundary layer as it passes over the heat shield. To check this possibility one set of data was obtained on a model which had a solid copper heat shield in place of the normal thin steel shell. By means of the added thermal mass the temperature of the nose was held to a lower value during the reheat period when data were taken. The results are shown in figure 20 for both $M_\infty = 5$ and 6. Circle symbols denote results from a normal test in which the average afterbody-surface temperature was somewhat below the heat-shield temperature; square symbols denote results obtained for a condition where the reverse is true. Lower heating rates were measured with a relatively cold heat shield, especially on the cylindrical section. Under the present line of reasoning this change would denote a more widely separated flow. Increased separation might result if the boundary layer were more stable in the expansion region, and increased stability could exist by virtue of energy removal by the cold surface of the heat shield. This result tends to differ from that reported in reference 26 where, for a sharp-nosed body, transition Reynolds numbers in a separated flow region were consistently lowered by decreases in wall temperature. While the results presented herein are relatively meager, it might be well to note, nevertheless, that this effect (the influence of model surface temperature on the extent of separation) places an added limitation on the usefulness of wind-tunnel measurements in separated-flow regions behind blunt bodies.

Circumferential distribution of heating rates.- Representative heat-transfer coefficients are plotted as a function of azimuth angle in figure 21, and curves have been faired through the data at $\alpha = 2^\circ$. On the conical afterbody at $S'/r = 0.88$ and $\alpha = 2^\circ$ the highest rates were measured on the lee side of the body as noted earlier. Pressures measured at this location (see fig. 16) do not provide an explanation of this behavior. At $\alpha = 10.6^\circ$ the distribution is much like that on an inclined cylinder. On the cylinder at $S'/r = 1.93$ a small change in angle of attack gives rise to a very pronounced variation in heating rates. This variation is in large part ascribed to the effects of flow asymmetry on transition and reattachment of the flow boundary.

Variation of afterbody heating rates with angle of attack.- The effects of angle of attack on afterbody heating rates at two specific locations are shown in figure 22. Heating rates are presented in ratio form to facilitate comparisons. In figure 22(a) results are presented for the conical surface at $S'/r = 0.9$, roughly the midpoint. Two theoretical curves are shown; both are estimates for an attached laminar boundary layer and are based on the method of reference 24. The solid line represents estimates based on the pressure level for two-dimensional flow over the conical section, while the estimates shown by the dashed line include the three-dimensional pressure gradients predicted by reference 21. This latter estimate is consistent with the theoretical basis used in both figures 15 and 19. It is clear, that at negative and small positive values of α, the theoretical curves can show no more than order-of-magnitude agreement with the experimental results since all the data presented are probably subject to the effects of some degree of flow separation. On the windward side of the body, however, most of the experimental results approach the predicted trend of the three-dimensional variation at larger angles of attack. The single data point at $\alpha = 30^\circ$

from reference 17 suggests an approach to a more two-dimensional flow environment when the afterbody surface has a positive inclination to the free-stream direction. Several exceptions to the general trend are worthy of notice, particularly the higher enthalpy results of the present investigation and those of reference 18. Both sets of measurements indicate heating rates that are considerably lower, relative to the stagnation point reference value, than are predicted with the theory.[5] The magnitude of these differences is still of questionable significance, however, since the present results are probably subject to effects of nonequilibrium flow over the afterbody while those from reference 18 may be low for reasons that are discussed in that report. The results at $M_\infty = 3.5$ and $\alpha = 10^\circ$ and 15° taken from reference 23 are higher, by a factor of two, than the prediction of the theory and are believed to represent a boundary layer that is either in transition or is turbulent. Data points at $\alpha = 0^\circ$ and 5° from this same reference have an arrow attached to each symbol (in fig. 22(a)) to denote that local heating rates were below the minimum value that could be resolved by the data recording system used in those tests.

In figure 22(b) heat-transfer results are presented for the cylindrical surface of the afterbody at $S'/r = 1.9$. The solid line represents a variation in heating rates with angle of attack predicted by theory for a boundary layer that is both attached and laminar. The broken line is an estimated variation for a turbulent boundary layer that has been matched to the measured value at $M_\infty = 5$ and $\alpha = 0^\circ$ (as was shown in fig. 19). A large part of the experimental results appears to represent flows which are not only locally turbulent, but which also experience pressures that exceed those predicted by theory for three-dimensional attached flow. There is an obvious similarity between these results and the pressure distributions of figure 18. This correspondence of pressure and heating-rate distributions can be illustrated. Consider, for example, the measured heating rate of 0.78 at $M_\infty = 3.5$ and $\alpha = 0^\circ$ taken from reference 23 and shown in figure 22(b). With the corresponding measured pressure from reference 23 and with the assumption that the turbulent origin is at the junction of the conical and cylindrical sections of the afterbody, the theory of reference 25 can be used to predict a local heating rate which is 0.85 of the stagnation point value. Thus, the combination of turbulent flow and high local pressures can result in very substantial heating rates on this apparently sheltered surface.

Real-gas effects on heat-transfer rates to the afterbody.- The previous discussion of heating rates to the afterbody of the Mercury capsule has been confined almost entirely to low-enthalpy results.

---

[5] A small part of this difference can be attributed to the direct comparison on this figure of the $\dot{q}/\dot{q}_s$ ratios for these two higher enthalpy tests with the low-enthalpy h/h_s ratios, as discussed earlier. However, since local Mach numbers on the afterbody are in general less than 4, figure 6 (top) indicates the effect of this mode of comparison to be of the order of 10 percent or less.

A brief consideration will now be given to the heat-transfer rates in a high-enthalpy environment. In figure 23 the ratios of local heating rates to stagnation values are presented as a function of stagnation enthalpy. Data from the present investigation and from references 17, 18, 19, and 23 are presented for the midpoint of the afterbody. The results of several theoretical estimates are also shown in figure 23. The curve for equilibrium attached flow was obtained from the flat-plate solution of reference 27 for two-dimensional flow of a dissociated stream and the corresponding stagnation point heating rate from reference 13. As such, the curve is basically an extension of the previous theoretical estimates for low-enthalpy test conditions. For want of a more exact method, the analytical result of reference 2 was used without modification to derive the curve for equilibrium separated flow; that is, heating rates for attached flow were reduced by a factor of about 2 to account for flow separation. The curve for frozen attached flow was obtained from the expression of reference 28 which relates the heat flux in a frozen flow and at a noncatalytic wall to the heat flux in an equilibrium flow by the equation

$$\frac{\dot{q}_F}{\dot{q}} = \frac{H_{F_l} - H_{F_w}}{H_l - H_w}$$

where the quantity $(H_{F_l} - H_{F_w})$ can be approximated by the term $c_p(T_l - T_w)$ and the specific heat, c_p, does not include the chemical or dissociation energy.[6] It will be remembered from appendix B that for the tests in the 2-inch shock tunnel it is likely that the inviscid flow over the afterbody of the model was not in chemical equilibrium. The concept of frozen flow that is introduced here is the limiting case of nonequilibrium flow and makes the maximum allowance for this effect. The curve for frozen separated flow was obtained with the arbitrary assumption that the ratio of heating rates for this type of flow to that for attached flow is a composite of the two previous effects and that there is negligible interaction between them. Thus, at any value of stagnation enthalpy, the heating-rate ratio due to separation was multiplied by the heating-rate characteristic of attached frozen flow.

---

[6] The use of this equation rests upon two additional assumptions which, at present, can be supported only by qualitative arguments. First, the boundary layer (or separated flow) on the afterbody is assumed to depart from chemical equilibrium and, second, the surface is assumed to be noncatalytic. The first assumption is based on the analysis of reference 28 which indicates that chemical nonequilibrium can occur in a boundary layer (e.g., in the stagnation region) even before such effects are encountered in the local inviscid flow. The assumption of a noncatalytic surface is also reasonable, since the afterbodies of the shock tunnel models used to measure heat transfer were made of a plastic material. In general, the literature indicates that such materials usually have a much reduced catalytic effect as compared to metallic or metal oxide surfaces.

The experimental results that are available from the present investigation and from the several references at $\alpha = 0^\circ$ are not sufficient to verify the numerous assumptions employed in the theoretical analysis. The purpose of the analysis is merely to approximate the level of heating recorded in the shock tunnel tests of the present investigation. However, it can be seen that the curves for flow in chemical equilibrium indicate an increase in heating rate, relative to that at the stagnation point, with increasing enthalpy. Conversely, the effect of relatively long times of chemical accommodation is to reduce the local heating-rate ratio as enthalpy is increased. The data obtained in the shock tunnel (the diamond symbol and bar) appear to represent an afterbody flow which is separated and essentially in the frozen state. On the basis of this very approximate analysis, then, the effect of increasing enthalpy on afterbody heating rates appears to depend upon the degree to which the local flow departs from chemical equilibrium. While the resultant changes are indicated to be relatively small in absolute magnitude, at least at the location chosen and for the assumptions made, it may be possible for the combined effects of flow separation and chemical accommodation to influence local rates by a factor of 5 or more at stagnation enthalpies approaching that for satellite velocity.

A489

Afterbody Flow Regimes

In the present paper liberal use has been made of the experimental results of several other investigations. The fact that such data were available has permitted the development, herein, of a more general analysis of the body flow field and the convective heat-transfer rates than would otherwise be possible. It has been found that reasonable estimates of local rates can be made if the character of the afterbody flow is known either from pressure measurements or visual evidence. However, the usefulness of these results for application at full scale is obviously hampered by uncertainty as to the occurrence and extent of flow separation at conditions different from those specifically investigated. Therefore, it appeared logical that an attempt should be made to correlate test results from the various referenced investigations with those of the present survey in a manner that might indicate regimes in which the afterbody flow is either attached or separated. An attempt at this correlation is presented in figure 24. The parameters employed are the enthalpy ratio H_w/H_s for the heat shield, and a characteristic Reynolds number. This Reynolds number, R_*, is based on equilibrium-flow properties at sonic speed in the expansion at the edge of the heat shield and on the length of run to that point. It is reasoned that the condition of the boundary layer in this region will have a strong influence on the nature of the afterbody flow. Likewise, the ratio of surface enthalpy to some enthalpy characteristic of the stream, in this case stagnation enthalpy, is also pertinent to boundary-layer development.[7] The test points represent three classifications of afterbody flow - attached, partially attached (or reattached), and separated, as indicated by the filled, half filled, and open symbols, respectively. In practice it was not always possible to make such classifications on the basis of visual evidence alone so that, where possible, both pressures and heating rates were used for added verification. Important additions to the test points shown in figure 24 are three curves which show the histories of enthalpy ratio and Reynolds number for a typical entry trajectory of a Mercury capsule and for the entry of an Atlas-boosted research and development vehicle. The calculated trajectory is represented by the two broken-line curves which are for assumed wall temperatures of 500° R and 2000° R. The solid curve represents a portion of the trajectory of the flight vehicle and was obtained from the results of references 29, 30, and 31.

Although the results presented in figure 24 do not show any clear-cut correlation, there are several indicated trends that are worthy of mention and that relate the test data to the reference curves. The study indicates (as might be expected) that the flow regime on the afterbody depends on the character of the boundary layer in this region. This dependence is reflected in the trend toward attached flow with increasing Reynolds number, at constant enthalpy ratio, shown in the figure. Presumably, the boundary-layer flow over the afterbody changes from laminar to turbulent as the Reynolds number at the corner increases by one to two orders of magnitude. In reference 32 a similar change from separated to attached flow was found to occur when the surface of the heat shield was roughened. The two test points illustrating this result (which was obtained at $M_\infty = 3.3$) are shown in figure 24 at R_* just under one million and at H_W/H_S of about 0.3. A somewhat analogous change seems to occur in the case of the full-scale research vehicle. The particular portion of the entry flight shown by the solid curve in figure 24 spans a time interval of about 35 seconds during which the flight Mach number dropped from about 21 to 12.5 and the altitude changed from about 220,000 to 150,000 feet. In this interval the measured heating rates at various locations on the afterbody increased so as to become equal to or greater than the corresponding estimated values for attached laminar flow. This behavior is illustrated in figure 12 of reference 31 and could be the result of a gradual reattachment, with increasing Reynolds number, of a previously separated afterbody flow.

The observed trend noted above is violated by several test points at the higher Reynolds numbers shown in figure 24. In general, these data represent tests at $M_\infty < 5$ where, as was mentioned earlier in the discussion of figure 18, the afterbody flow apparently changes from separated to attached with increasing M_∞. Again, a similar result has been reported in reference 32. This latter result is represented in figure 18 by the open square symbol at R_* about 10^6 (which is for $M_\infty = 3.3$) and the two filled square symbols at slightly lower Reynolds numbers, which represent higher Mach number test conditions in this same free-flight facility.

---

[7] It is recognized that the chosen parameters, while similar to those used in the literature to define boundary-layer transition on continuous surfaces, may not be sufficient to describe all factors which influence the behavior of separated flows.

For similar reasons, the flow regime on the afterbody seems to depend on wall enthalpy. Some tendency for a decrease of separation with decreasing enthalpy ratio can be seen in figure 24, for example, at R_* of about 10^5. This effect might conceivably be related to the phenomenon of transition reversal. The regime of partially attached flow covers a surprisingly wide range of enthalpy ratios. This regime might well be characterized by free-boundary transition in a separated afterbody flow followed by reattachment on the cylindrical section. This flow pattern has been discussed in several preceding sections of the present report. It is apparent, however, that additional information of a more systematic nature will be required to establish an adequate correlation of this type. In particular, most of the present results apply to a steady flight attitude at $\alpha = 0^\circ$, whereas it has been shown in reference 32 that a nonsteady or oscillating flight behavior can strongly affect the afterbody-flow development. There is also the distinct possibility that the chemistry of the flow over the afterbody could influence the separation behavior. This question has only been touched upon in the present report, and then in connection with small models for which the flow residence time is very brief.

Despite the numerous qualifications which have been placed on the experimental results shown in figure 24, there is strong evidence from both wind-tunnel and flight tests that the afterbody flow will not be separated throughout all of the entry flight of a full-scale capsule. The reference curves and the data presented indicate that the flow over the afterbody of the capsule could progress from the separated to the attached phase. The region of maximum convective heating to the stagnation point might well occur within the regime of partially attached flow. This combination of events could be expected to result in substantial heating rates on the cylindrical section of the afterbody.

CONCLUSIONS

An experimental investigation has been conducted to determine the convective heat-transfer rates and the surface pressures on a blunt-nosed body of revolution closely comparable to the Mercury capsule re-entry configuration. The following conclusions have been drawn from test results which were obtained for Mach numbers from 3.4 to 14.7, angles of attack from 0° to 10°, and stagnation enthalpies up to 5000 Btu per pound:

1. Stagnation-point heat-transfer rates, at angles of attack near zero, are about 13 percent in excess of nominal values for a spherical stagnation region due to increase in velocity gradient. The measured rates agree with theoretical estimates based on measured pressure distributions. These results can be correlated in a manner that shows a relatively minor dependence on stagnation enthalpy level.

2. The heating-rate distribution over the nose (heat shield) develops a substantial asymmetry with increasing angle of attack. Present results, when considered in conjunction with those of other investigations, indicate that this asymmetry in heating rate can be attributed to effects of the flow expansion at the edge of the heat shield on the pressure distribution and local-flow velocities over the heat-shield surface.

3. Afterbody pressures and pressure gradients may be estimated with fair accuracy if the boundary layer is not separated. The occurrence of boundary-layer separation, particularly at small angles of attack, can cause relatively large increases in afterbody pressures.

4. Afterbody heat-transfer rates at low-enthalpy test conditions varied from about 5 to 10 percent of the stagnation heating rate over most of the afterbody surfaces. In some cases, however, the effects of flow separation were such that values from 2 percent to almost 40 percent of the stagnation value were encountered. The magnitude of the convective heating rates to the afterbody can be estimated from measured pressure distributions if the nature of the afterbody flow, whether attached or separated, is known. Similar estimates for high-enthalpy conditions should make allowance for the effects of any chemical nonequilibrium in the local flow.

5. Boundary-layer separation is the most important single factor affecting afterbody pressures and heat-transfer rates. It is related to the existence of a laminar boundary-layer condition at the edge of the heat shield and a laminar free-boundary condition over the afterbody. When separation occurs, it is often followed by transition to turbulent flow within the free boundary at relatively low Reynolds numbers and a subsequent flow reattachment. This situation is characteristic of the test configuration and gives rise to very substantial afterbody heating rates. Test results indicate the possibility of this type of afterbody flow during a substantial portion of a normal entry flight.

Ames Research Center
National Aeronautics and Space Administration
Moffett Field, Calif., Nov. 20, 1961

APPENDIX A

CALIBRATION OF THE 2-INCH SHOCK TUNNEL

Recent studies of the physics and chemistry of high-energy gases have shown that during the expansion of a gas from high temperature and pressure in a reservoir to high velocity in a supersonic nozzle, a local condition of chemical nonequilibrium may be encountered. If reservoir enthalpy is sufficiently high to cause dissociation of part of the gas, it appears that as the flow expands through the nozzle the chemical composition will freeze at some intermediate value for which the chemical reaction times become large compared to the flow residence time. When this occurs, some portion of the gas remains in the dissociated state. Therefore, the test stream can be considerably different from that which would result from an isentropic equilibrium expansion. One additional factor that influences the test stream of a high-energy gas flow facility is the loss of heat to the reservoir and nozzle walls. This heat loss can be easily evaluated by calibration of the test stream, if the flow is in chemical equilibrium. However, for the case of nonequilibrium flow, it is difficult to separate the effects of this nonadiabatic process from those of the nonequilibrium process.

A489

One method for evaluation of these nonadiabatic, nonequilibrium effects on the flow in the shock tunnel used in the present investigation will now be considered. The method consists of two sets of nozzle flow calculations, each with a simplified model of the expansion process, which can be used to place limits on the actual flow behavior. The first of these simplified models is based on the assumption that the flow is nonadiabatic by virtue of heat loss to the nozzle walls and that this heat loss will account for any discrepancies in measured stream properties; the second model makes use of the assumptions that heat loss to the walls is negligible and that any lack of agreement among the measured stream properties can be attributed entirely to a departure from local equilibrium of the chemical and vibrational energies in the flow.

As a starting point in the analysis it can be shown that the nozzle flow does not correspond to an equilibrium isentropic expansion. The measured reservoir and stream conditions are as follows: a reservoir pressure of 823 atmospheres (12,100 psia), a stagnation pressure behind a normal shock in the test stream of 74 psia, a corresponding static pressure of about 0.81 psia, and a stream velocity of 14,400 feet per second. The air in the reservoir was compressed from room temperature and from an initial pressure of 10 psia which led to a nominal reservoir enthalpy of 5,410 Btu per pound. For an equilibrium isentropic flow, gas expanding from the noted reservoir conditions to the measured stream velocity would have the properties shown in case 1 of table II. In particular, stagnation pressure behind a normal shock wave would be 3-1/2 times greater, and stream static pressure would be 12 times greater than the values that were measured. For this reason the flow is known to be nonisentropic.

In the present discussion, it will be considered first that the differences between the measured pressures and those for an isentropic expansion are due to the effects of nonadiabatic flow; specifically, the total enthalpy and the entropy of the test stream were varied to match certain fixed test conditions as outlined below. Results of calculations by this method are shown as cases 2, 3, and 4 of table II. (Note that entropy (S/R) can decrease or increase from the reservoir value, if the net effect is that of heat removal or heat addition.) In case 2 the measured pitot pressure, velocity, and the nominal stagnation enthalpy were held constant while the static pressure and entropy level of the stream were allowed to vary. In case 3 the stream total enthalpy was unrestricted but the entropy level was fixed at about the nominal reservoir value. Finally, in case 4 the entropy level was also unrestricted and iteration proceeded until the measured stream static and pitot pressures were satisfied. The estimates were found to agree with the measured set of stream conditions at a stream total enthalpy of 4445 Btu per pound and at an entropy level (S/R) of 29.80. For this value of total enthalpy, a stream Mach number of 8.39 was obtained, as shown in case 4. Thus, a loss in total enthalpy of some 18 percent is indicated during the expansion process, if, of course, the flow is assumed to be in equilibrium.

It will now be considered that the difference between the measured stream properties and those for an isentropic equilibrium flow is due to the effects of local nonequilibrium flow. In these estimates, it will be assumed, after the method of reference 33, that the energies of both molecular vibration and dissociation are made unavailable by freezing of the nozzle flow. In the calculations, it is considered that the flow is in equilibrium until some point in the expansion and that it is frozen downstream of that point. The area ratio A/A_*, at the point of the freeze, was used as a parameter in the calculations. It was also assumed that in each case the frozen flow expanded to the geometric nozzle-exit area ratio which was 315. The freeze was assumed to occur at area ratios of 100, 10, and 1 and the calculated results are shown as cases 6, 7, and 8 in table II and in figure 25. The limiting case of equilibrium flow is included for comparison as case 5 in table II. As can be seen in figure 25, both the measured stream velocity (14,400 fps) and the measured static pressure (range of values from 0.73 to 0.86 psia) indicated that the departure from chemical equilibrium, in effect, occurs at an area ratio of approximately 5. The resultant conditions are shown as case 9 in table II where the corresponding Mach number is seen to be 8.4, while the Reynolds number is 1.1×10^6 per foot. The molecular-weight

[redacted]

ratio and the distribution of enthalpy, also as functions of the nozzle-area ratio, are presented in figure 26. If the flow freezes at $A/A_* \approx 5$, it can be seen that about 1000 Btu per pound will be unavailable.[1]

It is somewhat surprising that these stream conditions, based on the assumption of nonequilibrium nozzle flow, correspond so closely to those obtained earlier for the equilibrium nonadiabatic case (case 4, table II). Note, however, that the available energy in both cases is nearly the same and that, since only about one third of the oxygen is dissociated in the nonequilibrium case, the two gas streams are not widely dissimilar. Thus, it is apparent that the measured stream properties could represent either of the two test streams; one, an equilibrium-gas flow with substantial heat losses in the reservoir and nozzle; the other, a stream which does not lose heat to its surroundings but is not in chemical equilibrium. Now, each of these possibilities is a somewhat idealized situation, since the flow is not likely to be either completely frozen or completely in equilibrium. Additional information is required to resolve the problem of what are the actual stream properties. For example, in order to make a more quantitative estimate of the heat loss it is necessary to have an additional independent measurement that is characteristic of the test stream. At present, stagnation heating rate is the only such measurement available. Therefore, at the sacrifice of the traditional independence between stream calibration and the test program, and to the accuracy inherent in the theory of reference 13, stagnation heating rate will be used to define the total enthalpy of the test stream. It is assumed here that the flow behind the normal portion of the bow shock is in chemical equilibrium. From reference 13, the stagnation heat rate, $\dot{q}_s$, is a function only of gas properties at stagnation temperature, stagnation pressure, and body surface temperature. Since stagnation pressure and surface temperature are known, the heating rate can be used to define the stream total enthalpy. The results of this method are shown in figure 27, where stagnation heating rate is shown as a function of stagnation enthalpy. The measured rate indicates the probable stream total enthalpy, in this case, to be about 5000 Btu per pound. The difference between this value and the reservoir enthalpy, about 400 Btu per pound, is a measure of heat lost to the nozzle and test-section walls. The difference between the 5000 Btu per pound and the value computed for the equilibrium case (~4450 Btu/pound) is about the same magnitude as the dissociation energy shown in figure 26 at $(A/A_*)_F = 5$. Whether or not this correspondence is significant is open to question at present, although it should be noted that the vibrational energies are likely to be in local equilibrium at these flow conditions.

---

[1] A somewhat similar result has been found in the theoretical analysis of reference 34, where the expansion of a pure oxygen stream in a 15° hyperbolic nozzle from a reservoir pressure of 642 atmospheres and temperature of 10,620° R was calculated to depart from chemical equilibrium at an area ratio of about 5. The stream was indicated to be essentially frozen at A/A_* of about 25 with about one third of the oxygen in the dissociated state.

[redacted]

DE[redacted]SSIFIED

Now, since both the upper and lower limiting stream conditions that match the measured properties have close to the same Mach number and Reynolds number, it is postulated that these two parameters will be about the same at the intermediate enthalpy defined by the above analysis. The only bit of evidence outstanding that has been obtained and not used is the shock-wave angle from the sharp leading edge of a plate used to measure static pressure. With reference 35 as a guide, along with the assumed unit Reynolds number and the appropriate distance from the leading edge, it was found that the shock angle should be inclined at about 1-1/2 times the Mach angle. Application of this ratio to the measured shock-wave angle resulted in an indicated Mach number of 8.5

A
4
8
9

It is concluded, therefore, that the test stream in the shock tunnel during this investigation was not in chemical equilibrium and that the stream is best approximated by the conditions listed as case 10 in table II.

[redacted]

APPENDIX B

CHEMICAL EQUILIBRIUM IN MODEL FLOW FIELD

It has been shown in appendix A that the test stream of the 2-inch shock tunnel is probably not in a condition of chemical equilibrium. A related condition may also exist in the flow about the test models in this facility. Consider first the region between the normal portion of the shock wave and the stagnation point of the body, the dimensions of which are characterized by the shock-detachment distance. Now, the shock-detachment distance has been shown to be primarily a function of the density ratio that exists across the shock wave. (See, e.g., refs. 36 and 37.) Therefore, the detachment distance should be an indicator of flow properties, since shock-density ratio is influenced by chemical nonequilibrium. Measured values of detachment distance for the present investigation are shown as a function of stagnation to free-stream density ratio in figure 28(a). For comparison, a composite theoretical curve for hemispheres is shown, along with a modification of this variation to account for the "sonic corner effect" of the Mercury capsule configuration.[1] The adjusted curve appears to predict the trend of the data but is slightly low in magnitude. Note that the shock-tunnel data are in agreement with the relatively low-enthalpy wind-tunnel and free-flight data at point ②, where, as shown in the legend, the flow upstream of the shock wave is assumed to be frozen while that downstream of the shock wave is assumed to be in equilibrium. Figure 28(b) shows the effect of stagnation enthalpy on the variation of detachment distance with Mach number, with the theoretical curves that represent equilibrium flow derived from the adjusted Δ/R variation (the solid curve) of figure 28(a). These curves were obtained by computing the density ratio ρ_s/ρ_∞ for a given M_∞ and H_s and finding the corresponding Δ/R from the reference curve. Data are also shown from references 17 and 18. Again, point ② appears in best agreement with the average of the measured results from the shock tunnel and indicates that the measured Δ/R is that for which the flow approaching the stagnation point of the body is in equilibrium.

An alternate approach to the question of flow composition in the stagnation region is to estimate the time required for the shock-heated gas to achieve equilibrium and compare this to the time required for the gas to travel from the shock wave to the body. This has been done in an approximate fashion, using the relaxation data of references 38 and 39 as a guide, and the results indicate that the flow should be close to equilibrium by the time it reaches the body. Thus, within the accuracy of these two estimates, it would appear that the stagnation region of a model in the shock tunnel is enveloped in a gas which is in chemical equilibrium.

---

[1] The effect of sonic flow at the corner of the heat shield is covered in some detail in the main body of this report.

[redacted]

This method of flow analysis has also been applied to the flow field downstream of the stagnation point. (See also ref. 40.) The results of this analysis indicate that the inviscid flow approaching the corner of the heat shield makes only a small departure from the equilibrium condition. On the conical afterbody, for the case of a fairly complete expansion at the corner, the flow is indicated to be well into the frozen-flow regime. On the basis of this analysis, then, heat-shield data should be representative of equilibrium flow, while afterbody data may reflect substantial nonequilibrium effects in the local flow.

[redacted]

REFERENCES

1. Faget, Maxime A., Garland, Benjamine J., and Buglia, James J.: Preliminary Studies of Manned Satellites-Wingless Configuration: Nonlifting. NACA RM L58E07a, 1958.

2. Chapman, Dean R.: A Theoretical Analysis of Heat Transfer in Regions of Separated Flow. NACA TN 3792, 1956.

3. Sprinks, T.: A Review of Work Revelant to the Study of Heat Transfer in Hypersonic Separated Flows. Univ. of Southampton U.S.A.A. No. 138, June 1960.

4. Reller, John O., Jr., and Seegmiller, H. Lee: Convective Heat Transfer to a Blunt Lifting Body. NASA TM X-378, 1960.

5. Eggers, A. J., Jr., and Nothwang, George J.: The Ames 10- by 14-Inch Supersonic Wind Tunnel. NACA TN 3095, 1954.

6. Cunningham, Bernard E., and Kraus, Samuel: Experimental Investigation of the Effect of Yaw on Rates of Heat Transfer to Transverse Circular Cylinders in a 6500-Foot-Per-Second Hypersonic Air Stream. NACA RM A58E19, 1958.

7. Seiff, Alvin: A Free-Flight Wind Tunnel for Aerodynamic Testing at Hypersonic Speeds. NACA Rep. 1222, 1955.

8. Douglas, Thomas B., and Dever, James L.: Enthalpy and Specific Heat of Four Corrosion-Resistant Alloys at High Temperatures. Jour. Res. NBS, vol. 54, no. 1, Jan. 1955, Research Paper 2560, pp.15-19.

9. Kivel, Bennett: Radiation from Hot Air and Stagnation Heating. AVCO Res. Lab., Res. Rep. 79, Oct. 1959.

10. Hansen, C. Frederick: Approximations for the Thermodynamic and Transport Properties of High-Temperature Air. NACA TN 4150, 1958.

11. Cooper, Morton, Mayo, Edward E., and Julius, Jerome D.: The Influence of Low Wall Temperature on Boundary-Layer Transition and Local Heat Transfer on 2-Inch-Diameter Hemispheres at a Mach Number of 4.95 and a Reynolds Number per Foot of 73.2×10^6. NASA TN D-391, 1960.

12. Lees, Lester: Laminar Heat Transfer Over Blunt-Nosed Bodies at Hypersonic Flight Speeds. Jet Propulsion, vol. 26, no. 4, Apr. 1956, pp. 259-269.

13. Fay, J. A., and Riddell, F. R.: Theory of Stagnation Point Heat Transfer in Dissociated Air. AVCO Res. Lab., Res. Rep. No. 1, 1957.

[redacted]

14. Newlander, Robert A., Taylor, Nancy L., and Pritchard, E. Brian: Pressure Distribution on Two Models of a Project Mercury Capsule for a Mach Number Range of 1.60 to 6.01 and an Angle-of-Attack Range of 0° to 180°. NASA TM X-336, 1960.

15. Moeckel, W. E., and Weston, Kenneth C.: Composition and Thermodynamic Properties of Air in Chemical Equilibrium. NACA TN 4265, 1958.

16. Minzner, R. A., Champion, K. S. W., and Pond, H. L.: The ARDC Model Atmosphere, 1959. Air Force Cambridge Res. Cen., AFCRC-TR-59-267 ARDC, Aug. 1959.

17. Pritts, O. R., and Mallard, S. R.: Pressure and Heat Transfer Distribution on a One-Tenth Scale Mercury Capsule at Mach Number 8. AEDC-TN-59-164, Jan. 1960.

18. Wallace, A. R., and Swain, W. N.: Static Stability, Heat Transfer, and Pressure Distribution Tests of NASA-McDonnell Mercury Models at Mach Numbers 17 to 21. AEDC-TN-59-157, Jan. 1960.

19. Everhart, Philip E., and Bernot, Peter T.: Measurements of the Surface Flows, Heat Transfer, Pressure Distribution, and Longitudinal Stability of a Mercury Capsule Model at Mach Numbers of 6.9 and 9.6. NASA TM X-458, 1960.

20. Kemp, Nelson H., Rose, Peter H., and Detra, Ralph W.: Laminar Heat Transfer Around Blunt Bodies in Dissociated Air. AVCO Res. Lab., Res. Rep. 15, May 1958.

21. Syvertson, Clarence A., and Dennis, David H.: A Second-Order Shock-Expansion Method Applicable to Bodies of Revolution Near Zero Lift. NACA TR 1328, 1957.

22. Feldman, Saul: Hypersonic Gas Dynamic Charts for Equilibrium Air. AVCO Res. Lab., Jan. 1957.

23. Taylor, Nancy L., Hodge, Ward F., and Burbank, Paige B.: Heat Transfer and Pressure Measurements of a 1/7-Scale Model of a Mercury Capsule for an Angle-of-Attack Range of 0° to 20° at Mach Numbers of 3.50 and 4.44. NASA TM X-522, 1961.

24. Van Driest, E. R.: The Laminar Boundary Layer With Variable Fluid Properties. North Amer. Aviation, Inc., Rep. AL-1866, Jan. 19, 1954.

[redacted]

25. Lee, Dorothy B., and Faget, Maxime A.: Charts Adapted from Van Driest's Turbulent Flat-Plate Theory for Determining Values of Turbulent Aerodynamic Friction and Heat-Transfer Coefficients. NACA TN 3811, 1956.

26. Larson, Howard K., and Keating, Stephen J., Jr.: Transition Reynolds Numbers of Separated Flows at Supersonic Speeds. NASA TN D-349, 1960.

27. Romig, Mary F., and Dore, F. J.: Solutions of the Compressible Laminar Boundary Layer Including the Case of a Dissociated Free Stream. Convair Rep. ZA-7-012, Aug. 4, 1954.

28. Goodwin, Glen, and Chung, Paul M.: Effects of Nonequilibrium Flows on Aerodynamic Heating During Entry Into the Earth's Atmosphere From Parabolic Orbits. Advances in Aeronautical Sciences, vol. 4; Proc. Second Int. Cong. for Aeronautical Science, Pergamon Press, 1961, pp. 997-1018.

29. O'Neal, Robert L., and Rabb, Leonard: Heat-Shield Performance During Atmospheric Entry of Project Mercury Research and Development Vehicle. NASA TM X-490, 1961.

30. Stephens, Emily W.: Afterbody Heating Data Obtained From an Atlas-Boosted Mercury Configuration in a Free Body Reentry. NASA TM X-493, 1961.

31. Weston, Kenneth C., and Swanson, Joanna E.: A Compilation of Wind-Tunnel Heat-Transfer Measurements on the Afterbody of the Project Mercury Capsule Reentry Configuration. NASA TM X-495, 1961.

32. Sommer, Simon C., Short, Barbara J., and Compton, Dale L.: Free-Flight Measurements of Static and Dynamic Stability of Models of the Project Mercury Re-entry Capsule at Mach Numbers 3 and 9.5. NASA TM X-373, 1960.

33. Yoshikawa, Kenneth K., and Katzen, Elliott D.: Charts for Air Flow Properties Equilibrium and Frozen Flows in Hypervelocity Nozzles. NASA TN D-693, 1961.

34. Hall, J. Gordon, and Russo, Anthony L.: Studies of Chemical Nonequilibrium in Hypersonic Nozzle Flows. Cornell Aeronautical Lab. Rep. No. AD-1118-A-6, Nov. 1959.

35. Kendall, James M., Jr.: An Experimental Investigation of Leading-Edge Shock-Wave-Boundary-Layer Interaction at Mach 5.8. Jour. Aero. Sci., vol. 24, no. 1, Jan. 1957, pp. 47-56.

[redacted]

36. Hayes, Wallace D.: Some Aspects of Hypersonic Flow. Ramo-Wooldridge Corp., Jan. 1955.

37. Maslen, S. H., and Moeckel, W. E.: Inviscid Hypersonic Flow Past Blunt Bodies. Jour. Aero. Sci., vol. 24, no. 9, pp. 683-693, Sept. 1957.

38. Logan, Joseph G., Jr.: Relaxation Phenomena in Hypersonic Aerodynamics. Cornell Aero. Lab., Inc., IAS Preprint 728, 1957.

39. Camac, M., Camm, J., Keck, J., and Petty, C.: Relaxation Phenomena in Air Between 3000 and 8000° K. AVCO Res. Lab., Res. Rep. 22, Mar. 1958.

40. Boison, J. Christopher: Experimental Investigation of the Hemisphere-Cylinder at Hypervelocities in Air. AEDC-TR-58-20, Nov. 1958.

[redacted]

[redacted]

TABLE I.- FREE-STREAM AND STAGNATION POINT CONDITIONS

Facility	Free stream			Stagnation point				Model Dia., in.
	Mach no.	Velocity, fps	Reynolds no.[a]	Pressure, psfa	Enthalpy, Btu/lb	Temperature, °R	Mol. wt. ratio	
10- by 14-inch wind tunnel	3.50[b]	2150	1.68×10^{6}	2603	129	540	1	2.0
	3.99[b]	2215	1.33×10^{6}	1718	129	540	1	2.0
	5.03	2575	5.87×10^{5}	764	159	665	1	2.0
	5.96	2910	2.86×10^{5}	372	191	800	1	2.0
2-inch shock tunnel	8.4[c]	14400	4.60×10^{4}	10580	5410	10620	1.24	.50
	8.4[d]	14400	4.60×10^{4}	10580	5000	10210	1.22	.50
	8.4[e]	14400	4.60×10^{4}	10580	4445	9410	1.20	.50
1-foot shock tunnel	10[b]	13800	7.35×10^{3}	406	4020	7960	1.208	1.50
SSFF	3.38[b]	3790	2.49×10^{6}	25480	409	1662	1	1.65
	5.34[b]	4480	3.31×10^{6}	23800	473	1892	1	1.65
	5.80[b]	4915	2.20×10^{6}	65050	552	2180	1	.45
	9.93[b]	6630	1.49×10^{6}	36900	926	3460	1	.45
	14.71[b]	10060	2.05×10^{6}	84600	2074	6390	1.02	.45
Full scale	15	16580	5.57×10^{5}	540	5620	9740	1.28	74.5
	22	23034	2.09×10^{5}	258	10696	11175	1.59	74.5

[a] Based on maximum diameter.

[b] Schlieren or shadowgraph photographs only.

[c] Frozen test stream.

[d] Nominal test stream used herein.

[e] Equilibrium test stream.

[redacted]

DECLASSIFIED

TABLE II.- CALIBRATION OF TEST STREAM IN THE SHOCK TUNNEL

[Measured quantities: p_T = 12100 psia, V_∞ = 14400 ft/sec, p_s = 74.0 psia, p_∞ = 0.81 psia]

Case no.	Reservoir					Stream quality	Test stream								$\left(\frac{A}{A_*}\right)_F$	Stagnation point				
	p_T, psia	H_T, Btu/lb	T_T, ^oR	Z_T	$(S/R)_T$		p_∞, psia	H_∞, Btu/lb	T_∞, ^oR	$(S/R)_\infty$	Z_∞	V_∞, fps	M_∞	R_∞/ft		p_s, psia	H_s, Btu/lb	T_s, ^oR	Z_s	$(S/R)_s$
1	12100	5410	12960	1.148	32.75	Equil.	9.7	1270	4380	32.75	1	14400	4.80	1.8×10^6	---	265	5410	11160	1.223	37.30
2	↓	↓	↓	↓	↓	↓	2.7	1270	4350	34.00	1	↓	4.80	5.2×10^5	---	74.0	5410	10620	1.238	38.80
3	↓	↓	↓	↓	↓	↓	2.1	900	3330	32.80	1	↓	5.40	6.0×10^5	---	↓	5040	10260	1.223	38.40
4	↓	↓	↓	↓	↓	↓	.81	305	1260	29.80	1	↓	8.39	1.1×10^6	---	↓	4445	9410	1.197	37.45
5	↓	↓	↓	↓	↓	↓	1.65	782	2970	32.75	1	15200	5.75	6.05×10^5	315	↓	5410	---	---	---
6	↓	↓	↓	↓	↓	Frozen	1.40	630	2410	---	1.000	15150	5.85	6.66×10^5	100	↓	↓	---	---	---
7	↓	↓	↓	↓	↓	↓	.93	380	1540	---	1.047	14700	7.80	9.68×10^5	10	↓	↓	---	---	---
8	↓	↓	↓	↓	↓	↓	.42	146	610	---	1.137	13500	10.20	1.61×10^6	1	↓	↓	---	---	---
9	↓	↓	↓	↓	↓	↓	.81	295	1200	---	1.068	14400	8.40	1.1×10^6	5	↓	↓	10670	1.240	38.85
10	↓	↓	↓	↓	↓	Non-equil.	.81	295	1200	---	---	14400	8.40	1.1×10^6	---	↓	5000	10210	1.222	38.27

[redacted]

A
4
8
9

DE[redacted]SSIFIED

MODEL SKIN IS
STAINLESS STEEL
TYPE 321

Thermocouple Number	Skin Thickness
1	.0094 in.
2	.0093
3	.0094
4	.0061
5	.0062
6	.0065
7	.0062
8	.0063
9	.0063
10	.0062
11	.0060
12	.0065
13	.0060
14	.0062
15	.0059

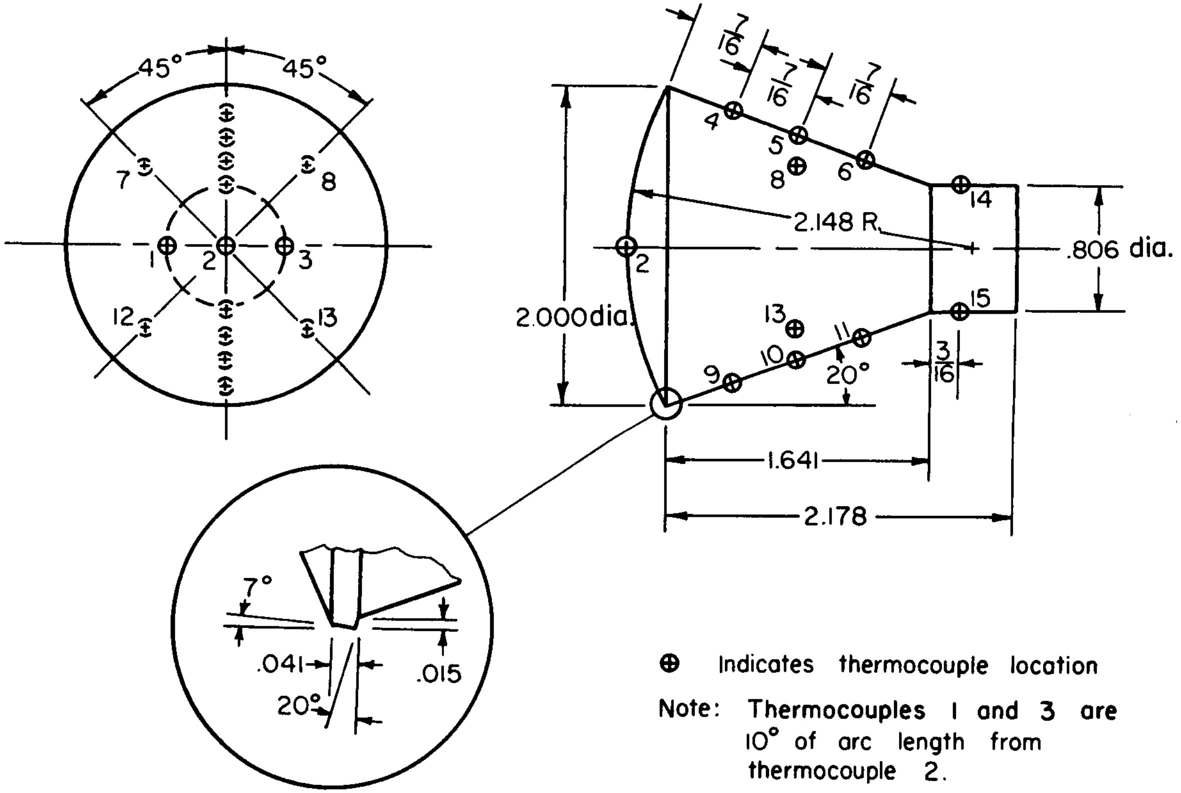
45°
45°
1
2
3
4
5
6
7
8
9
10
11
12
13
14
15
7/16
7/16
7/16
2.148 R
2.000dia.
.806 dia.
20°
3/16
1.641
2.178
7°
.041
.015
20°

⊕ Indicates thermocouple location

Note: Thermocouples 1 and 3 are 10° of arc length from thermocouple 2.

(a) Heat-transfer model for the wind tunnel.

Figure 1.- Test models. (All dimensions in inches.)

[redacted]

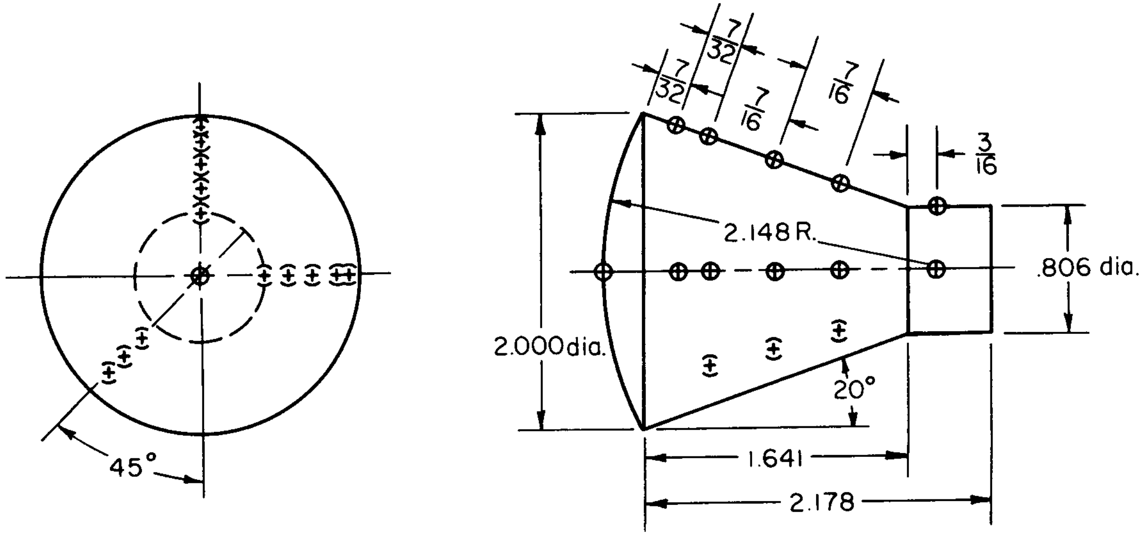
45°
7/32
7/32
7/16
7/16
3/16
2.148 R.
.806 dia.
2.000 dia.
20°
1.641
2.178

⊕ Indicates location of pressure tap

Note: Pressure tap on nose of model has .016" diameter orifice. All others have .042" diameter orifices.

(b) Pressure model for the wind tunnel.

Figure 1.- Continued.

[redacted]

DEC[redacted]SIFIED

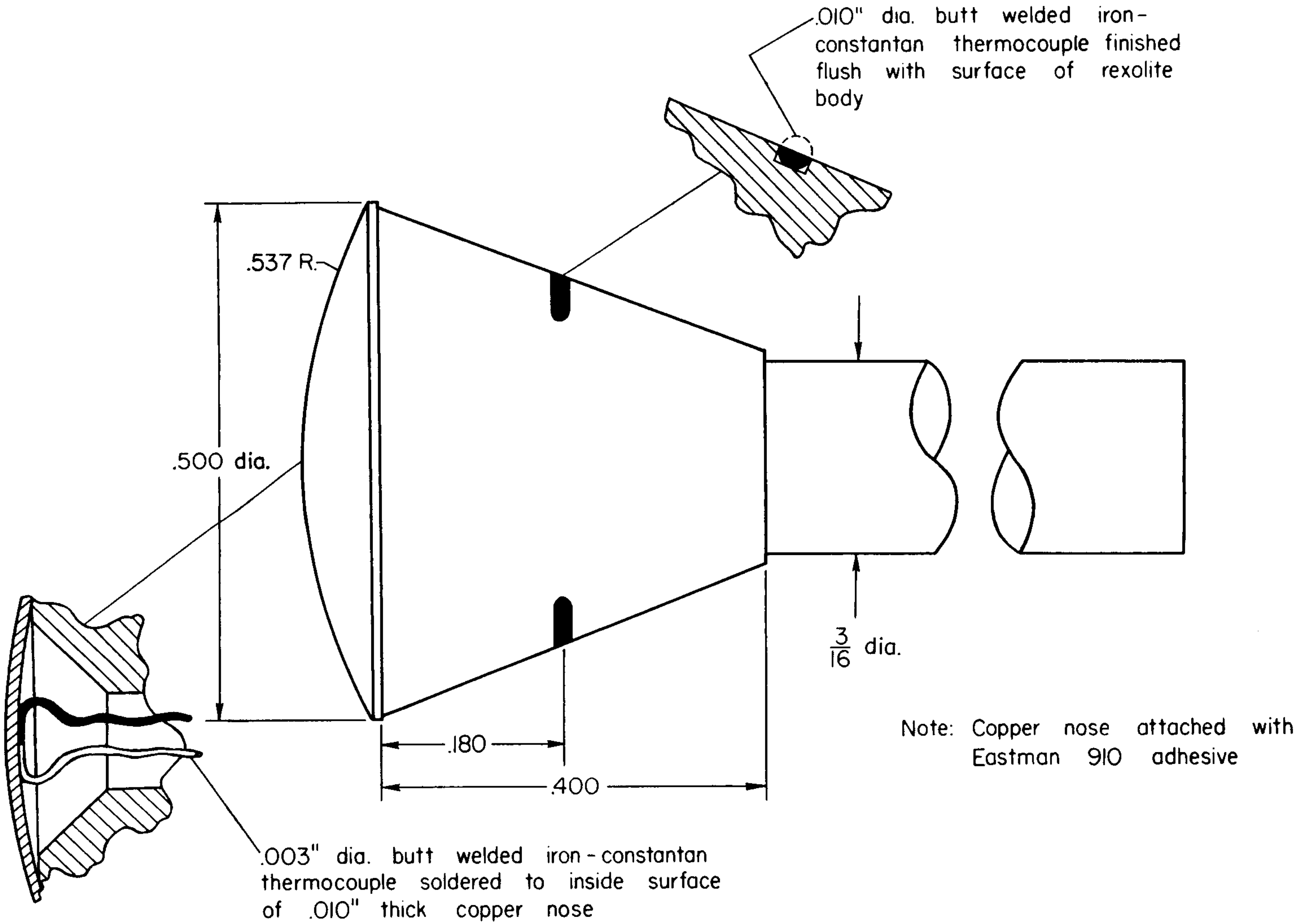
.010" dia. butt welded iron-constantan thermocouple finished flush with surface of rexolite body
.537 R.
.500 dia.
.180
.400
3/16 dia.
Note: Copper nose attached with Eastman 910 adhesive
.003" dia. butt welded iron-constantan thermocouple soldered to inside surface of .010" thick copper nose

(c) Heat-transfer model for the 2-inch shock tunnel.

Figure 1.- Continued.

[redacted]

DECLA[redacted]IED

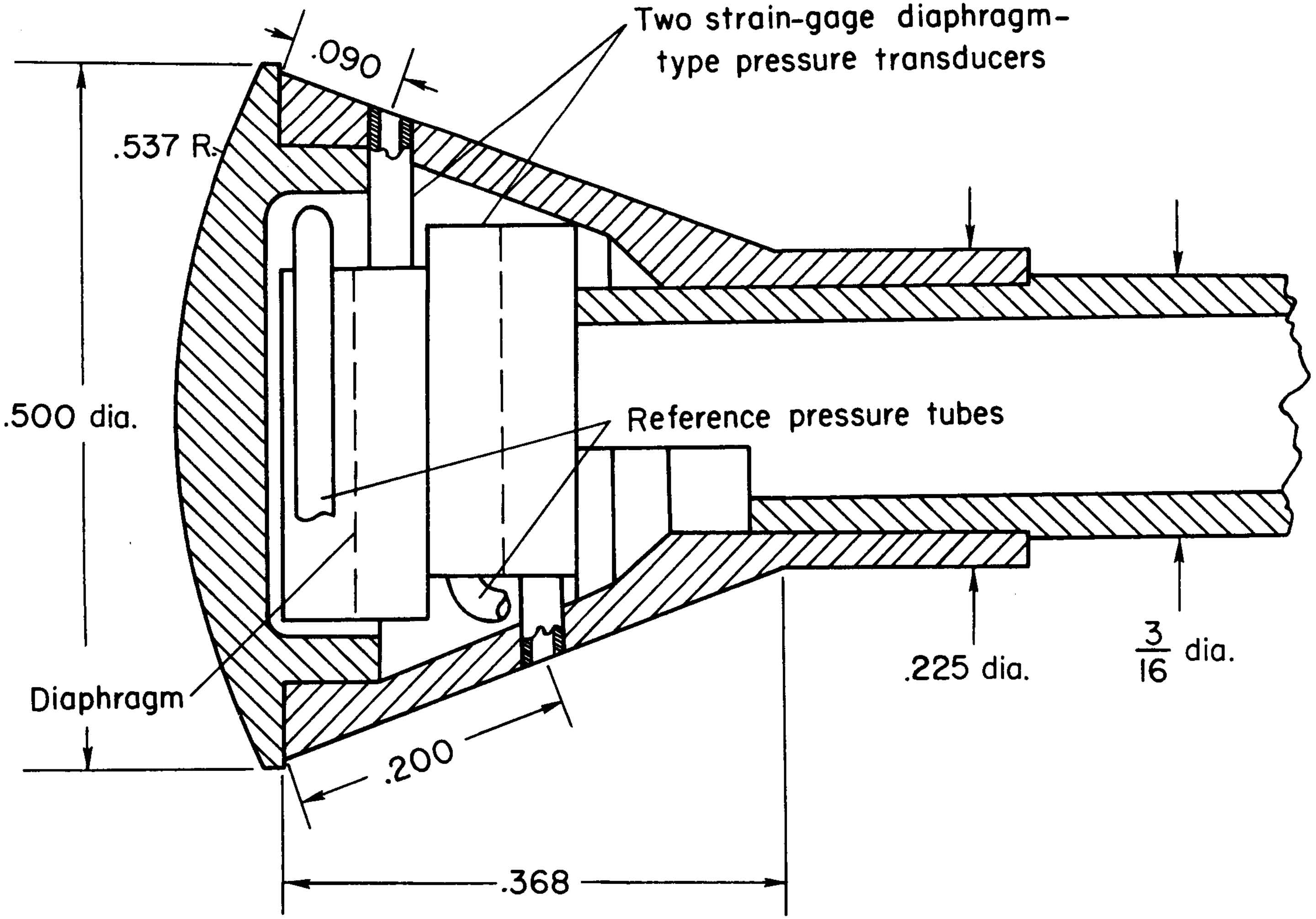
Two strain-gage diaphragm-type pressure transducers
.090
.537 R.
.500 dia.
Reference pressure tubes
Diaphragm
.200
.368
.225 dia.
$\frac{3}{16}$ dia.

(d) Afterbody pressure model for the 2-inch shock tunnel.

Figure 1.- Continued.

[redacted]

DEC[redacted]SIFIED

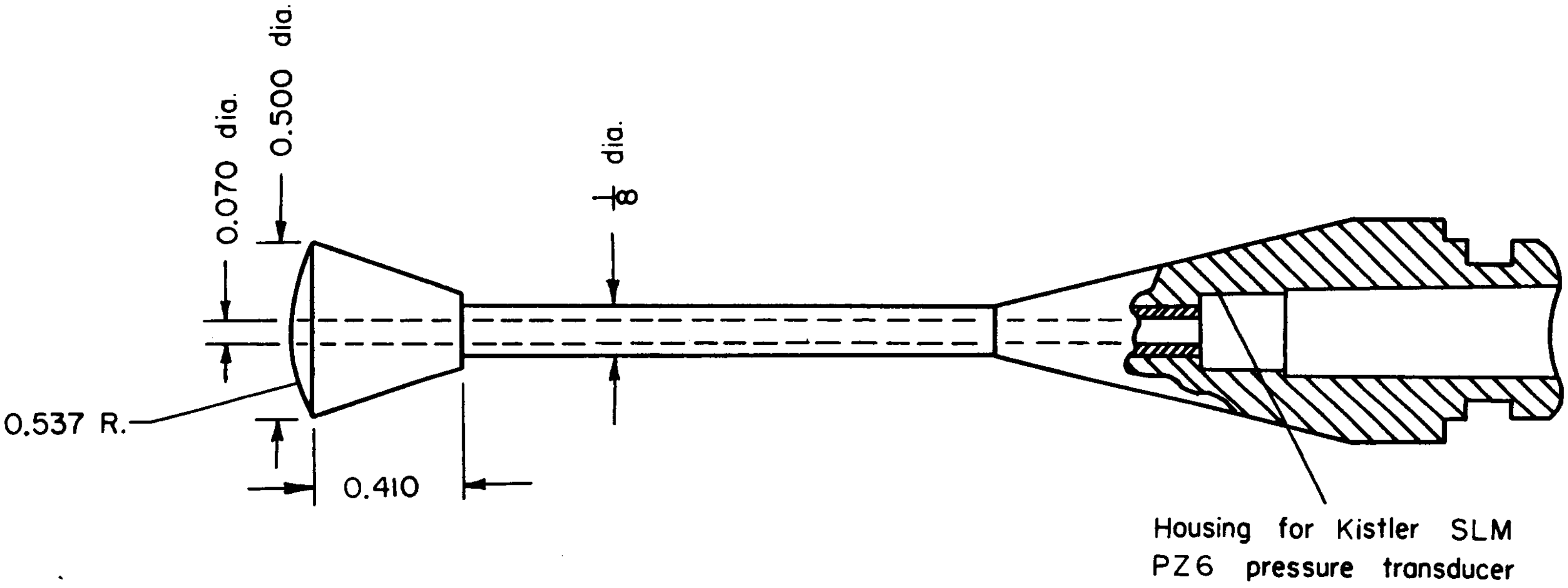
0.070 dia.
0.500 dia.
$\frac{1}{8}$ dia.
0.537 R.
0.410
Housing for Kistler SLM PZ6 pressure transducer

(e) Stagnation pressure model for the 2-inch shock tunnel.

Figure 1.- Concluded.

[redacted]

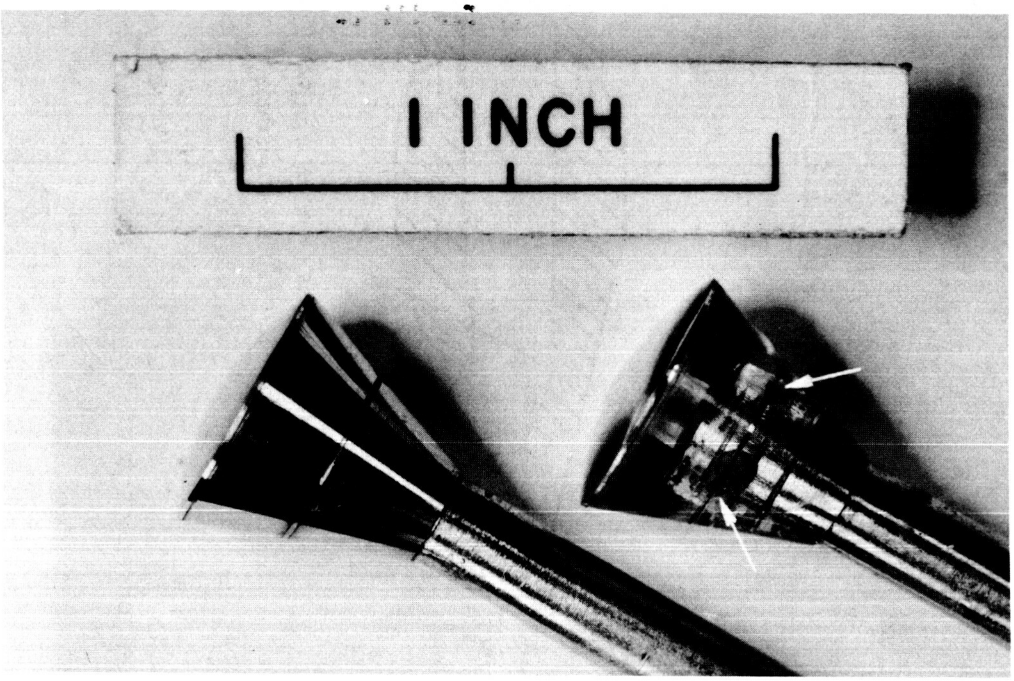

A-25213.1

(a) Afterbody thermocouple installation.

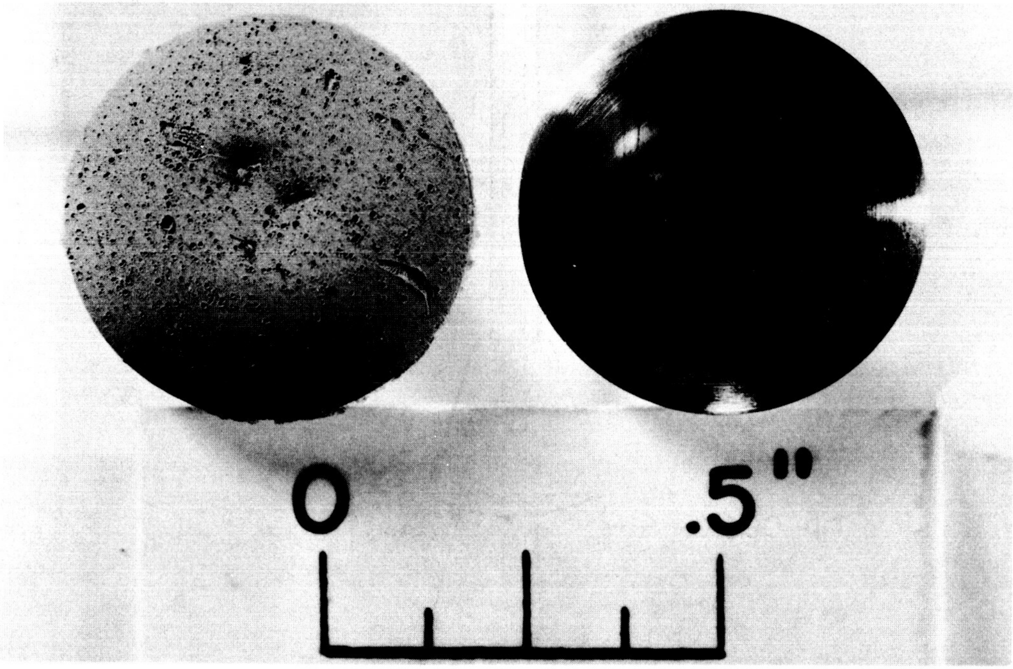

A-25212

(b) Condition of copper heat shield before and after test.

Figure 2.- Heat-transfer models for the 2-inch shock tunnel.

[redacted]

A
4
8
9

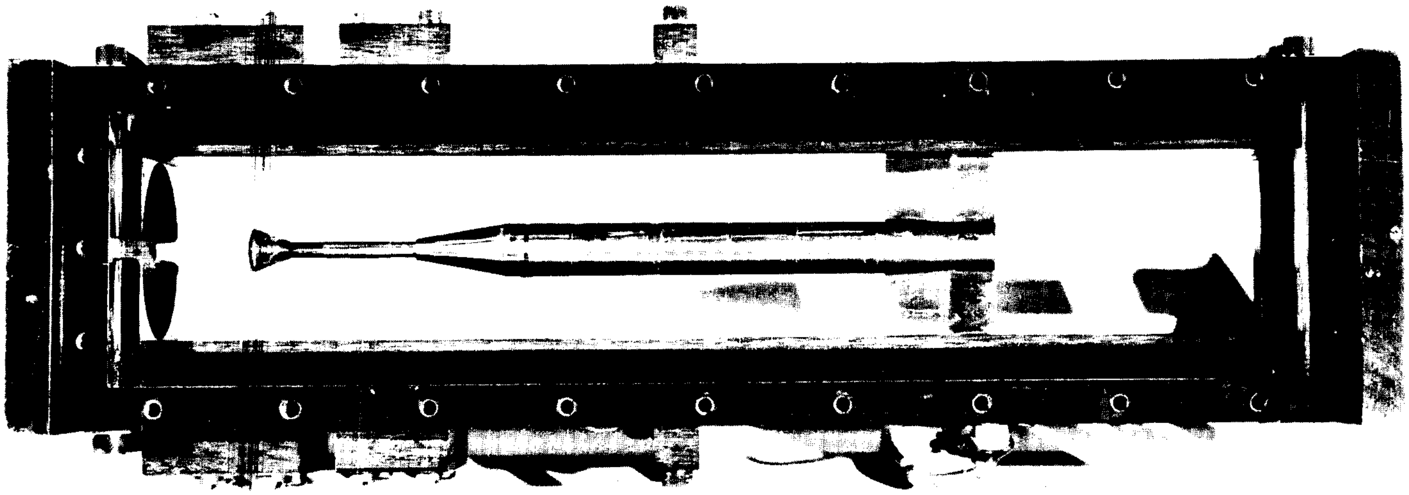

A-25242

Figure 3.- Heat-transfer model mounted in test section of the 2-inch shock tunnel.

[redacted]

[redacted]

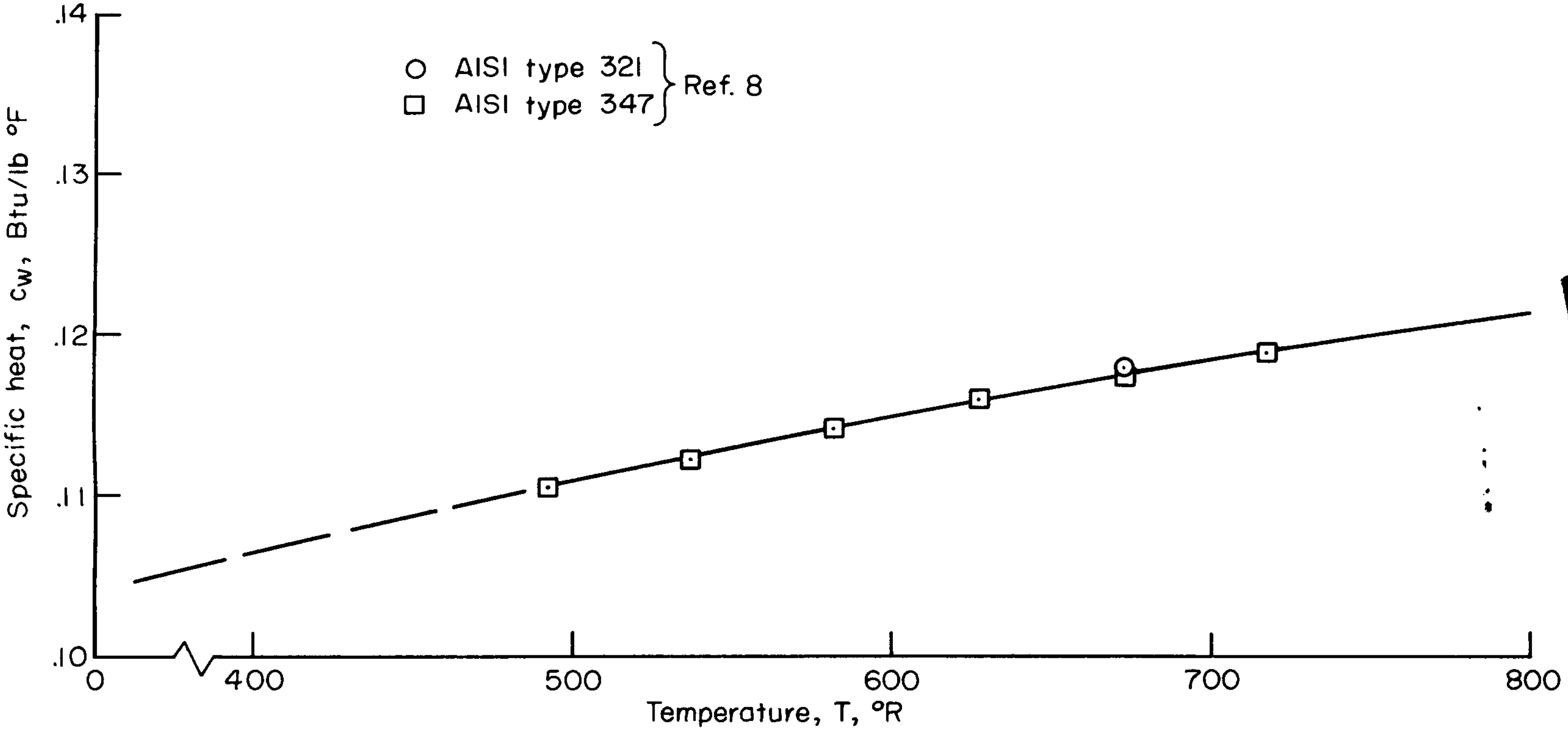

Figure 4.- Specific heat of model shell material.

[redacted]

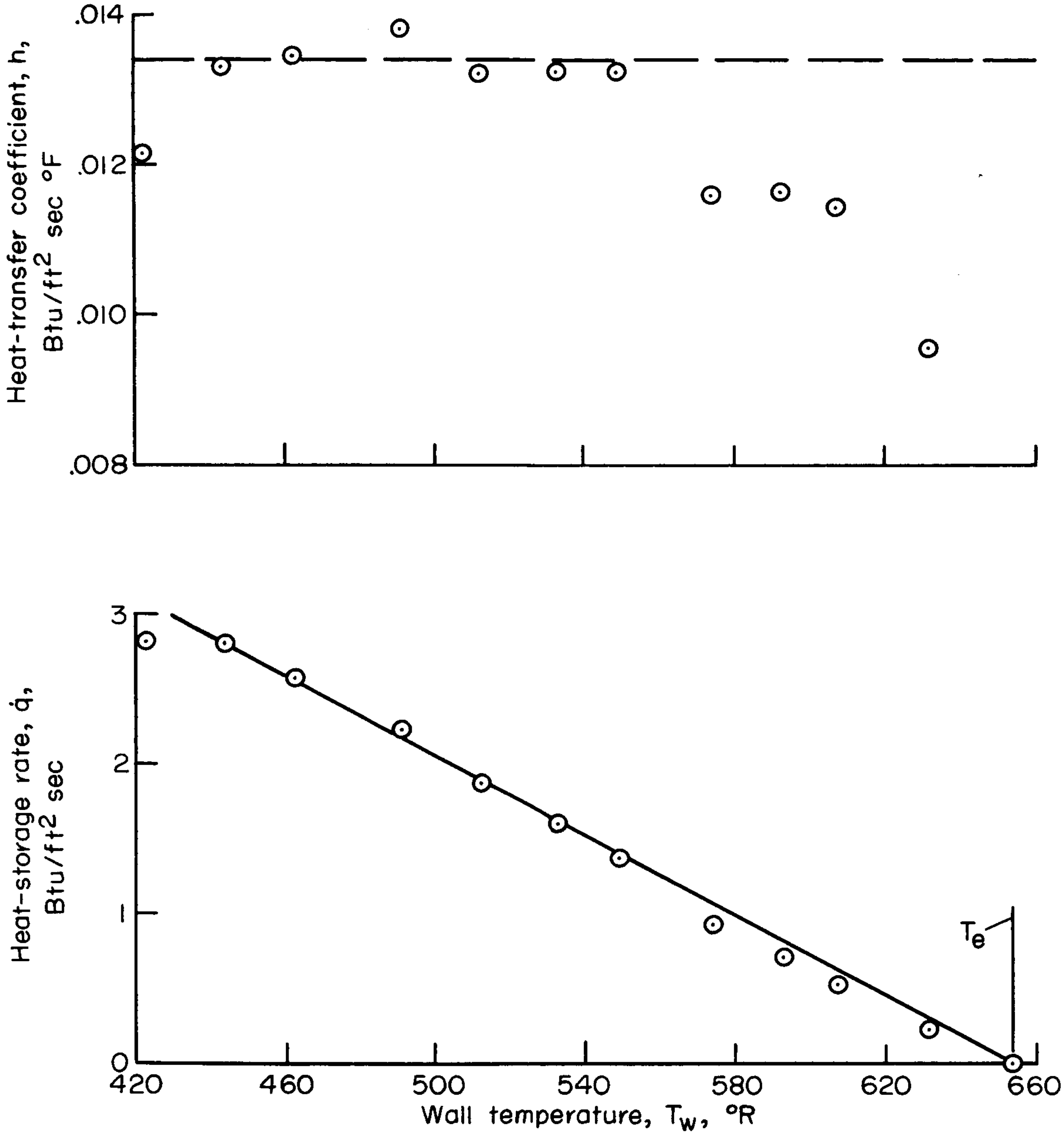

(a) Heat shield thermocouple.

Figure 5.- Analysis of oscillograph record for a typical reheat cycle.

[redacted]

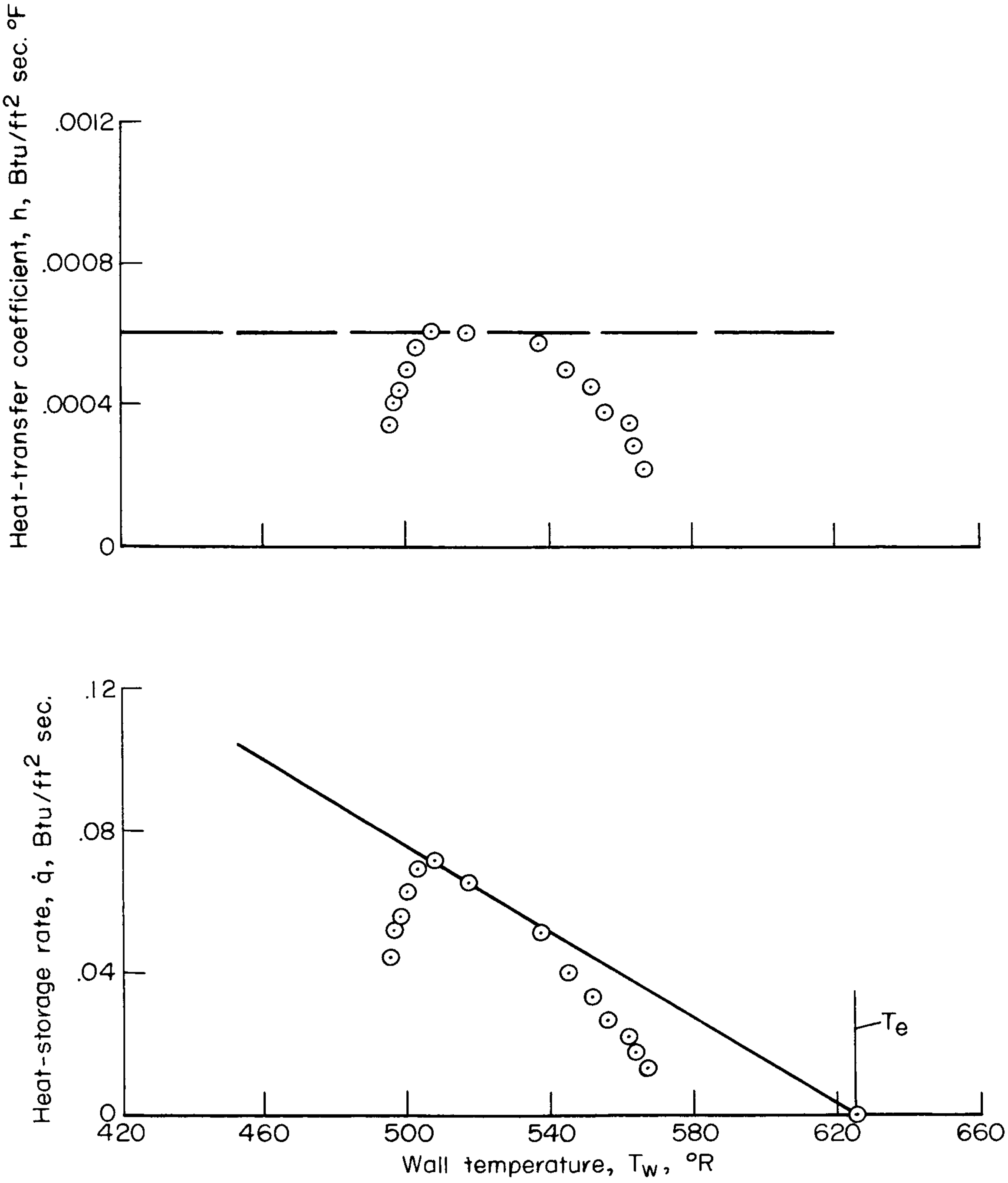

(b) Conical afterbody thermocouple.

Figure 5.- Concluded.

[redacted]

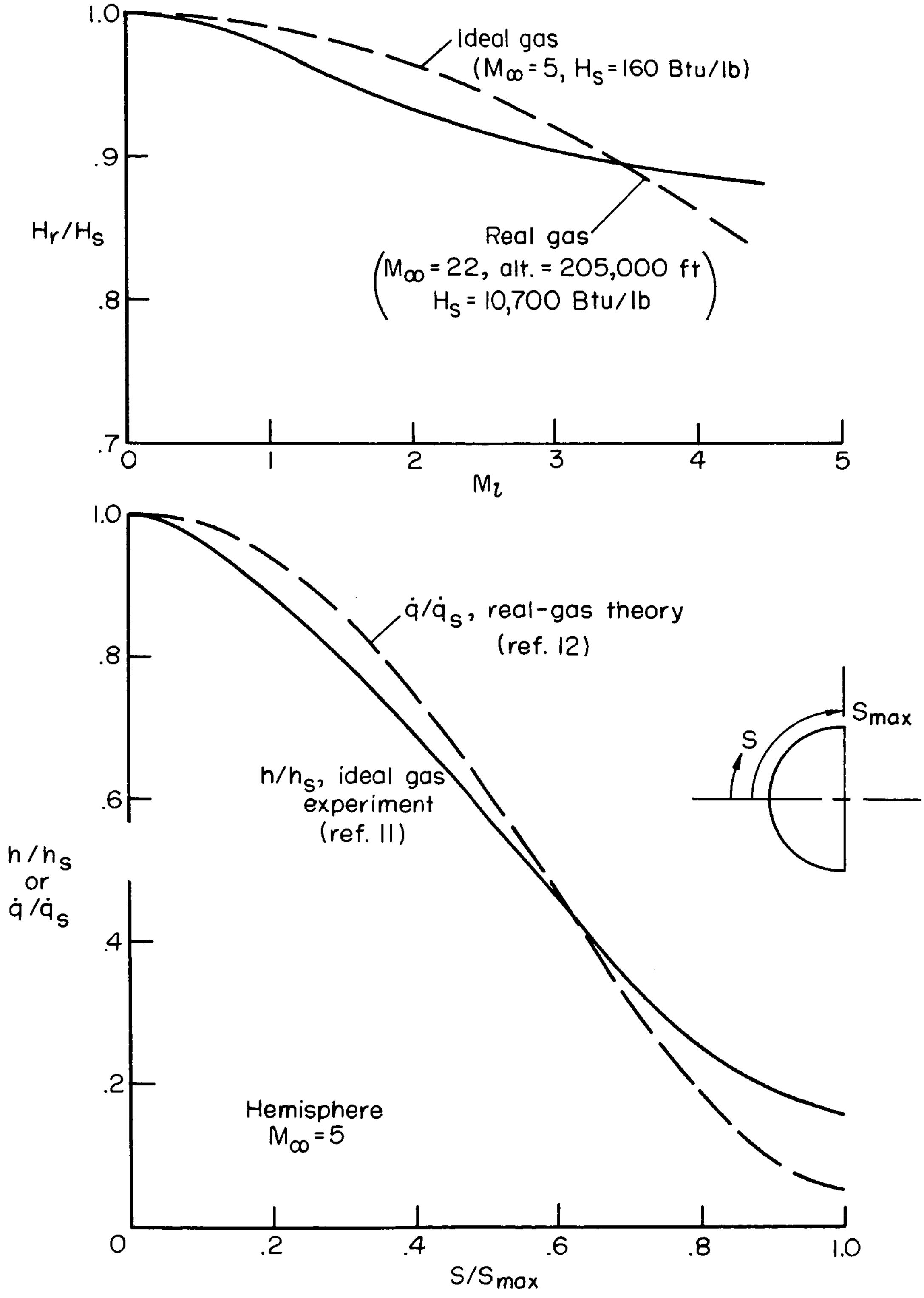

Figure 6.- Comparison of measured ideal-gas heating rates with real-gas predictions; laminar boundary layer.

[redacted]

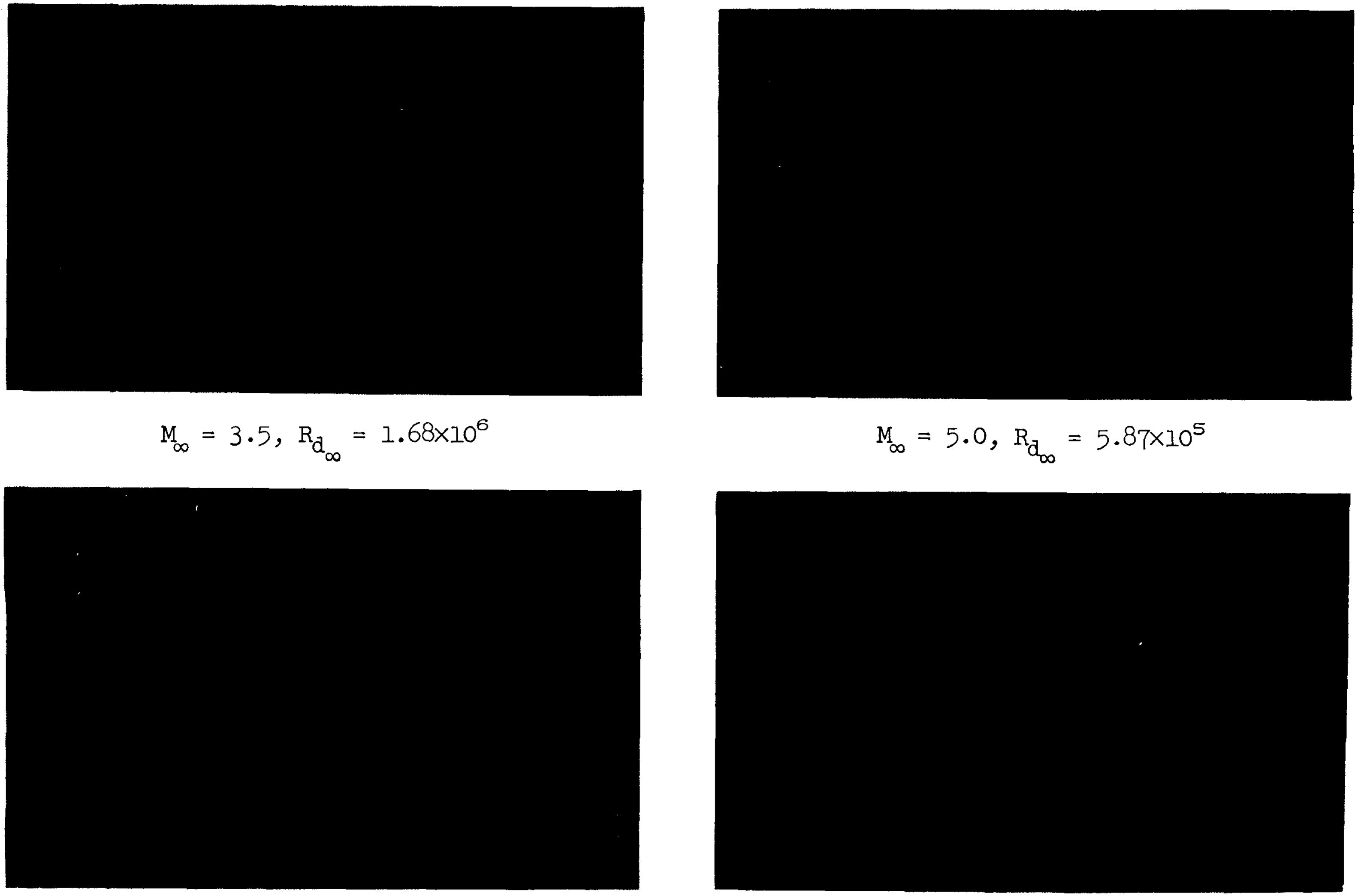

$M_\infty = 3.5$, $R_{d_\infty} = 1.68\times10^6$

$M_\infty = 5.0$, $R_{d_\infty} = 5.87\times10^5$

$M_\infty = 4.0$, $R_{d_\infty} = 1.33\times10^6$

$M_\infty = 6.0$, $R_{d_\infty} = 2.86\times10^5$

(a) $\alpha = 0^\circ$

Figure 7.- Shadowgraph pictures of flow about Mercury capsule model in the wind tunnel.

[redacted]

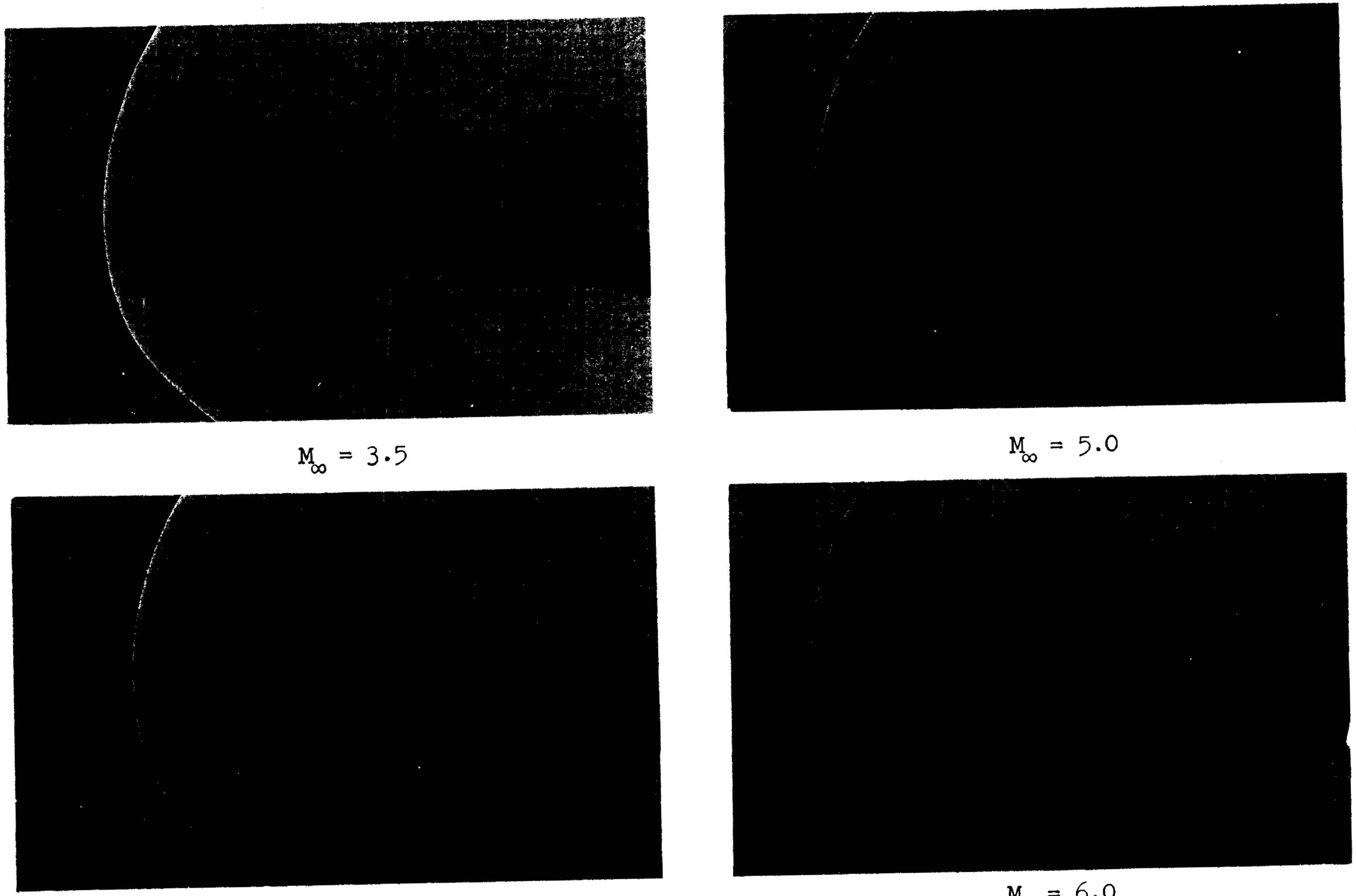

$M_\infty = 3.5$

$M_\infty = 5.0$

$M_\infty = 4.0$

$M_\infty = 6.0$

(b) $\alpha = 10.6^\circ$

Figure 7.- Concluded.

[redacted]

A
4
8
9

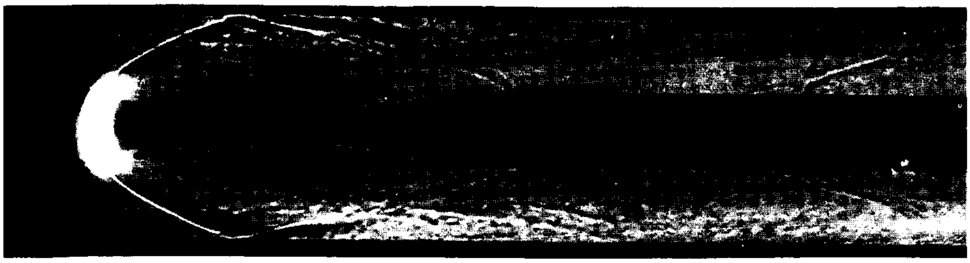

Schlieren picture, $\alpha = 0^\circ$

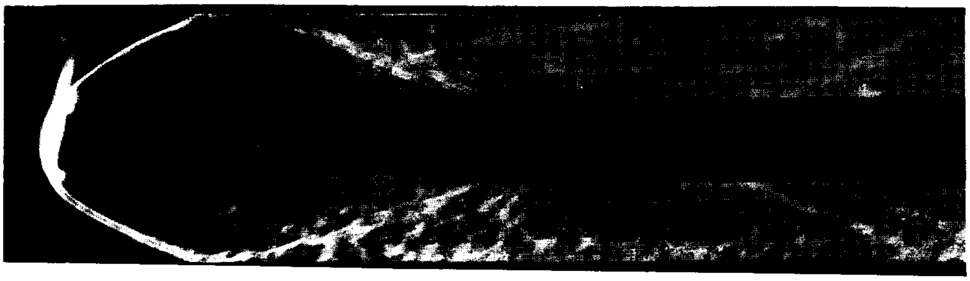

Schlieren picture, $\alpha = 10.6^\circ$

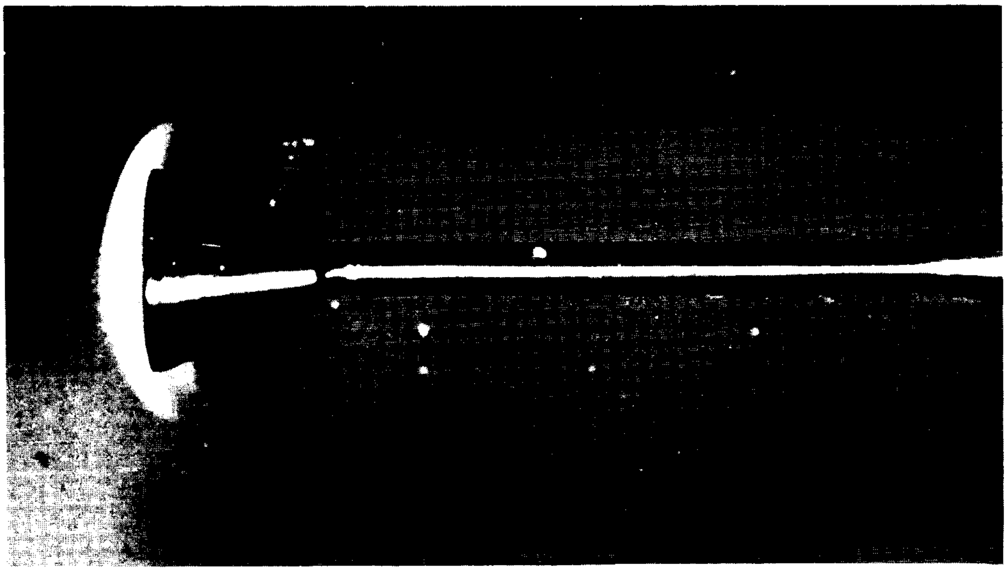

A-25667

Glow picture, $\alpha = 0^\circ$

Figure 8.- Visualization of flow about Mercury capsule models in the 2-inch shock tunnel; $M_\infty = 8.4$, $R_{d_\infty} = 4.6\times10^4$.

[redacted]

DECLASSIFIED [redacted]

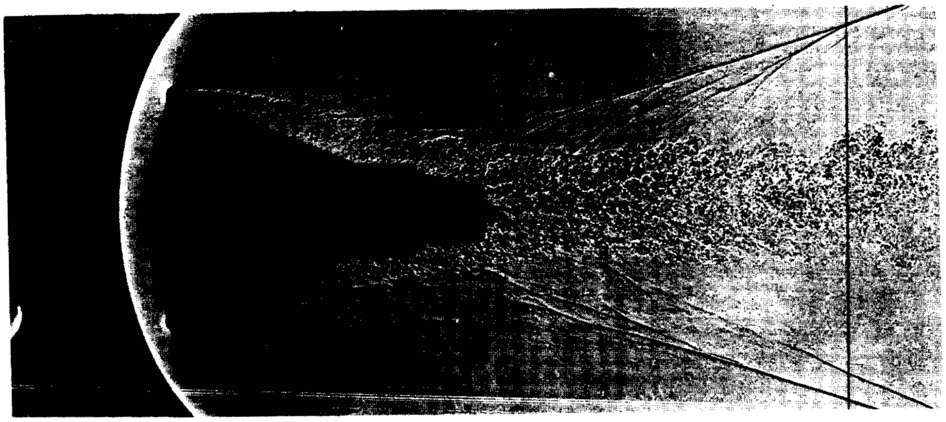

A-25027

(a) $M_\infty = 3.38$, $R_{d_\infty} = 2.49\times10^6$

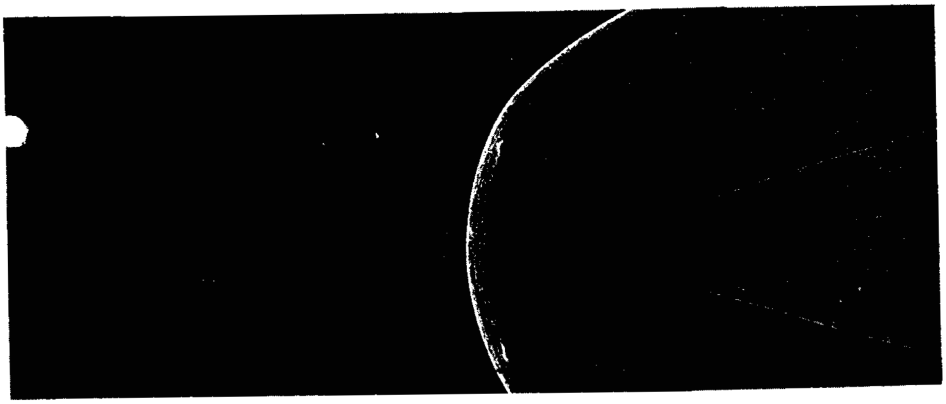

A-26040

(b) $M_\infty = 5.34$, $R_{d_\infty} = 3.31\times10^6$

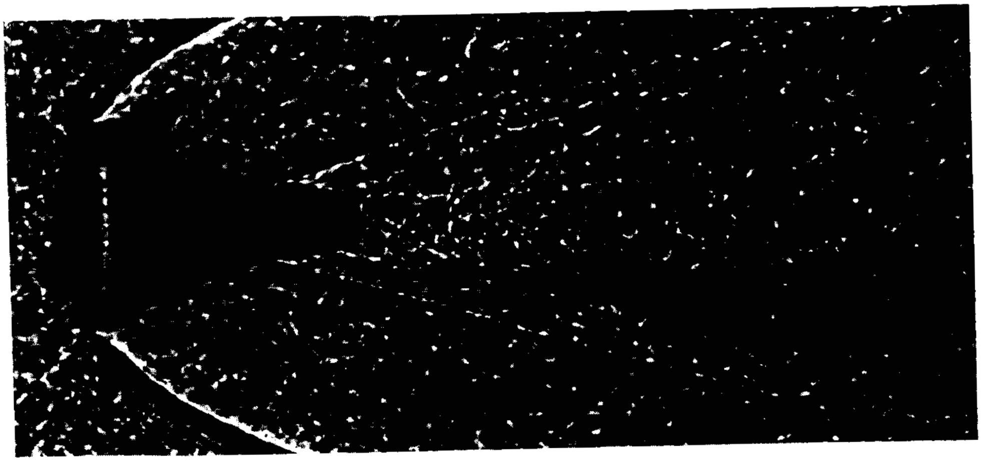

(c) $M_\infty = 5.80$, $R_{d_\infty} = 2.20\times10^6$

Figure 9.- Shadowgraph pictures of flow about Mercury capsule models in the free-flight wind tunnel; $\alpha \approx 0^\circ$.

[redacted]

DECLASSIFIED [redacted]

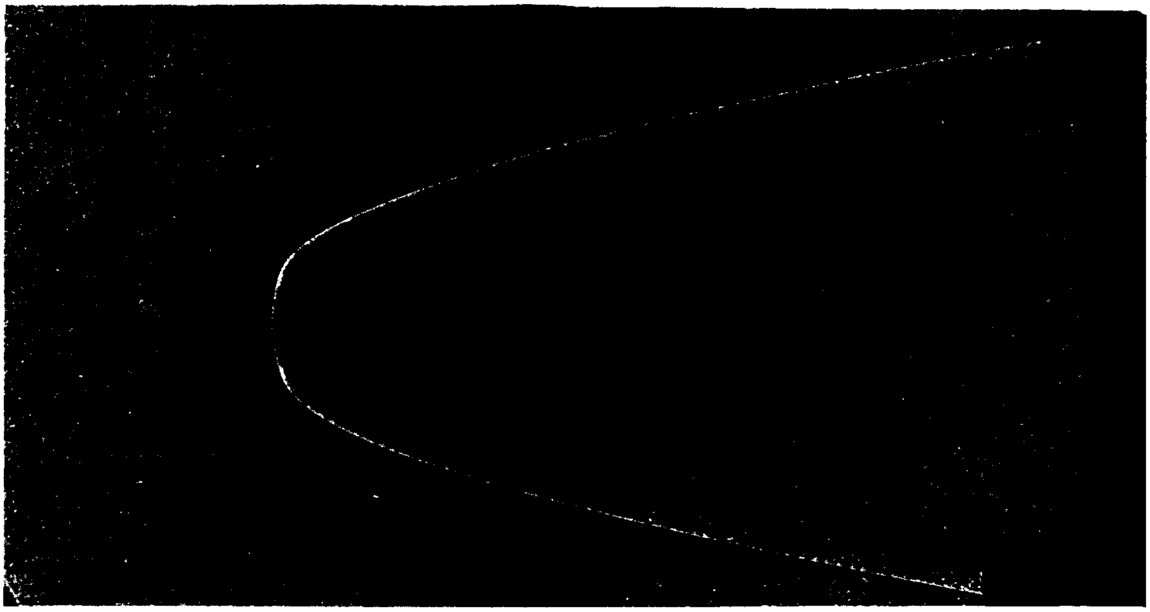

(d) $M_\infty = 9.93$, $R_{d_\infty} = 1.49\times10^6$

A-25025

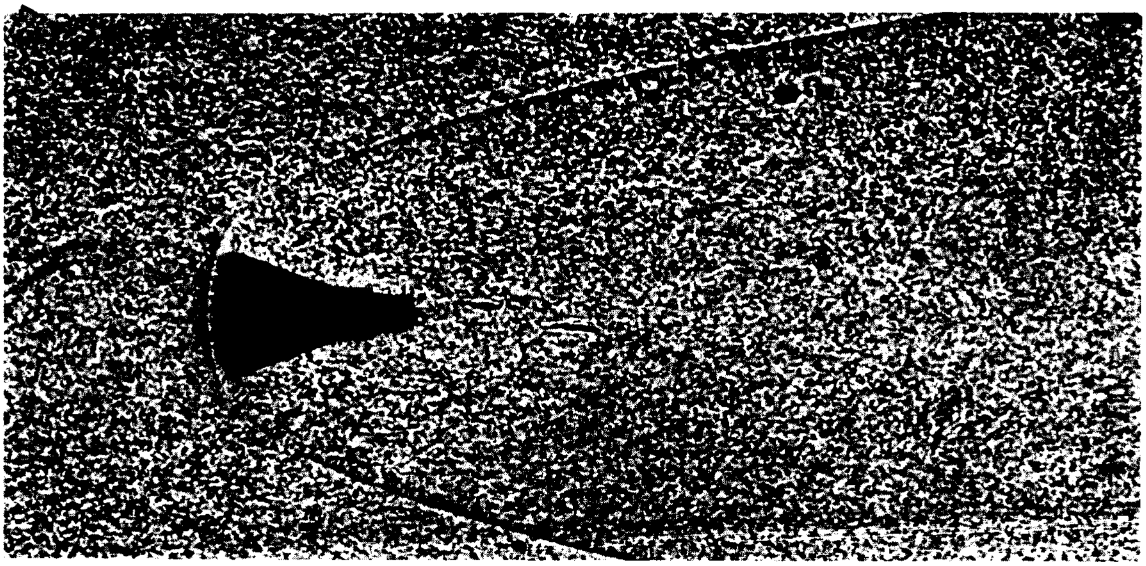

(e) $M_\infty = 14.71$, $R_{d_\infty} = 2.05\times10^6$

Figure 9.- Concluded.

DE[redacted]SIFIED

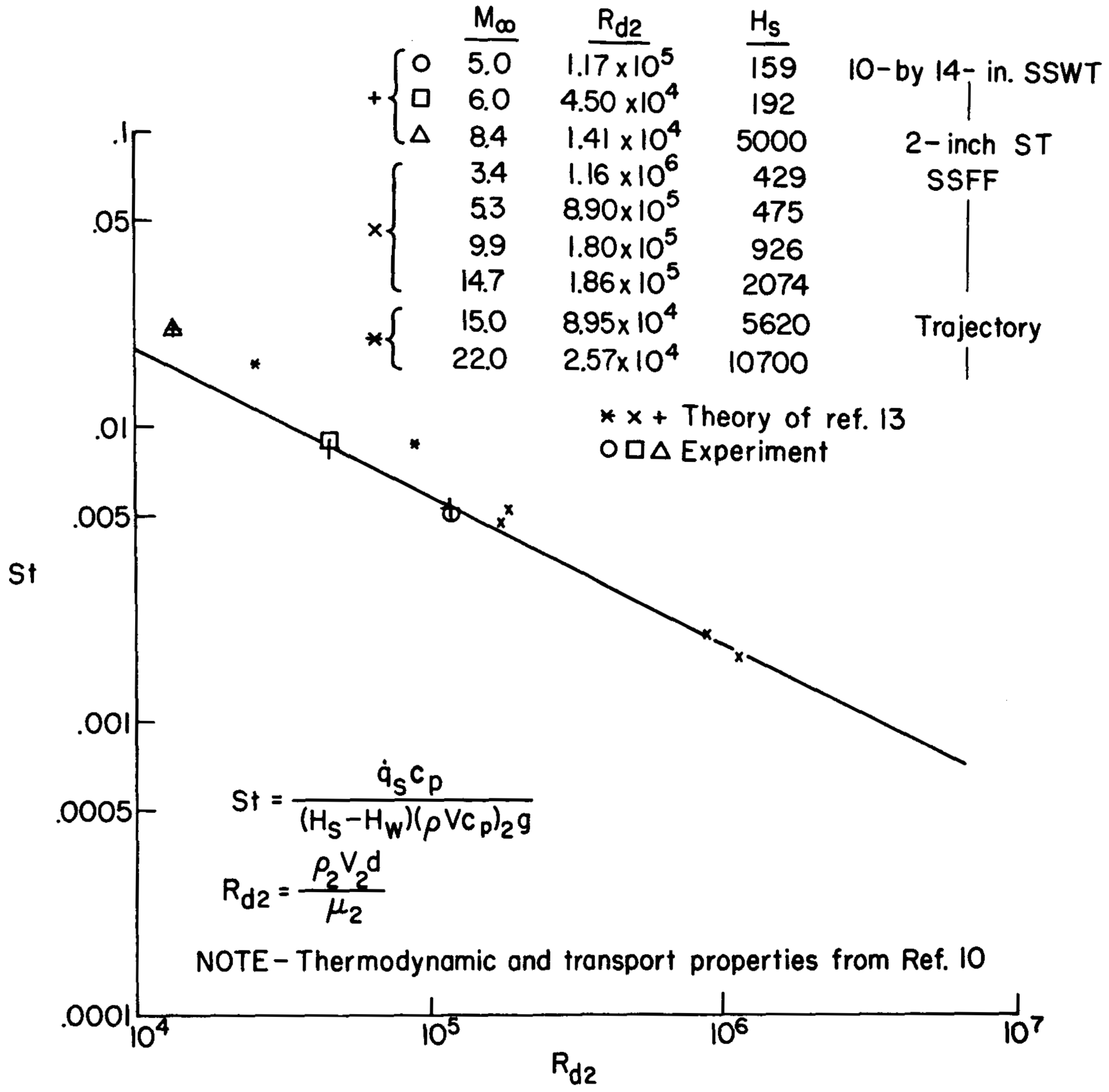

(a) Reynolds number dependence.

Figure 10.- Correlation of heating rates at stagnation point; $\alpha = 0^\circ$.

[redacted]

[redacted]

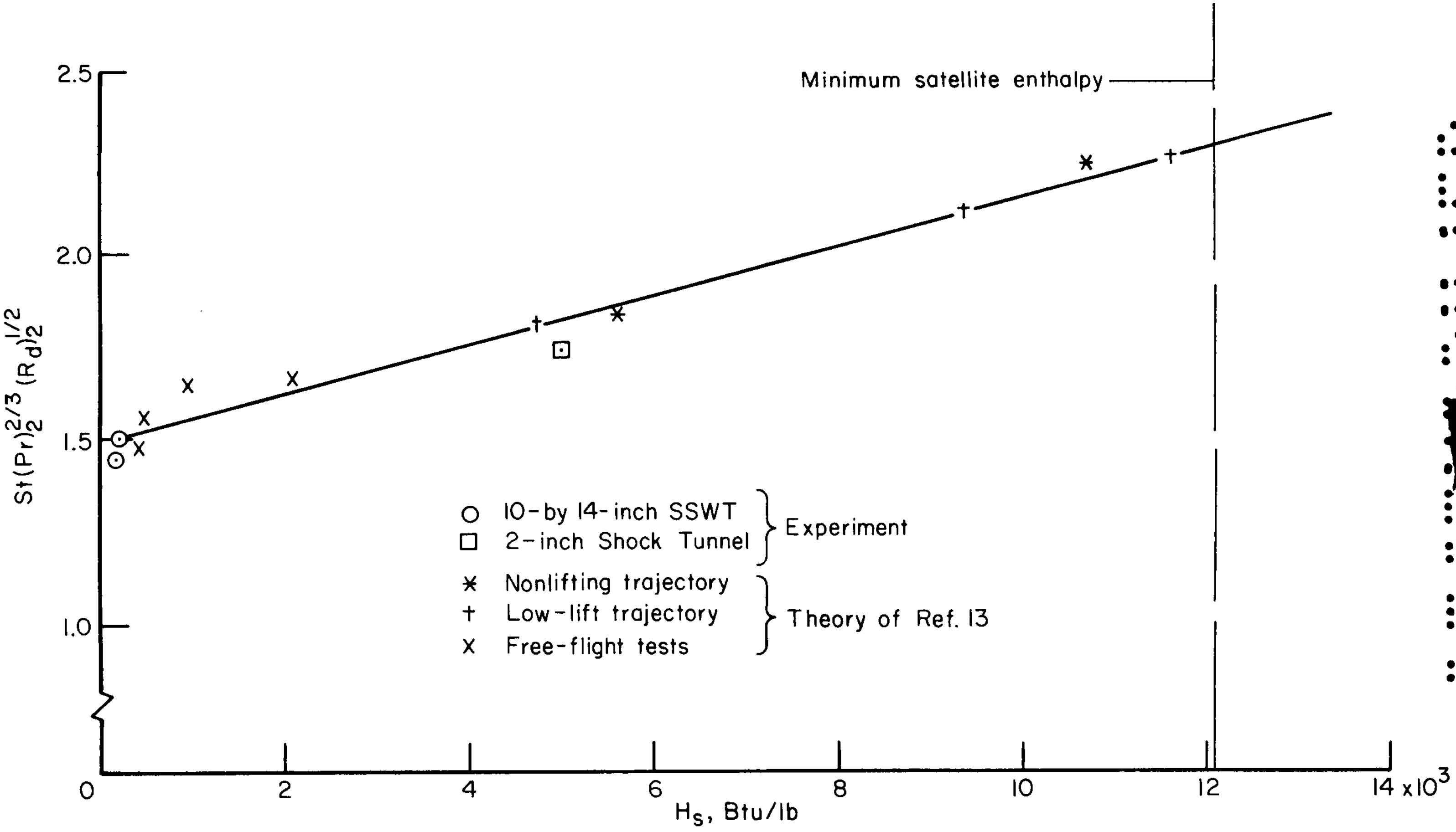

(b) Enthalpy dependence.

Figure 10.- Concluded.

DECLASSIFIED [redacted]

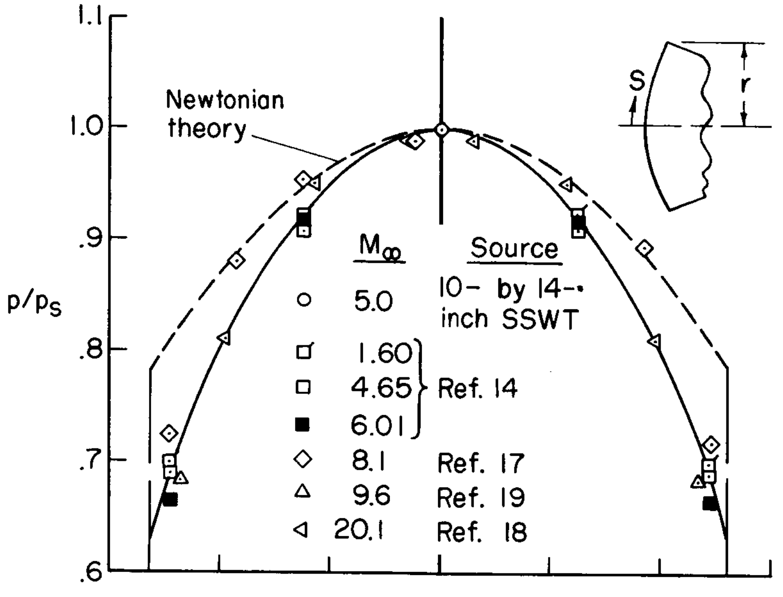

(a) α = 0°

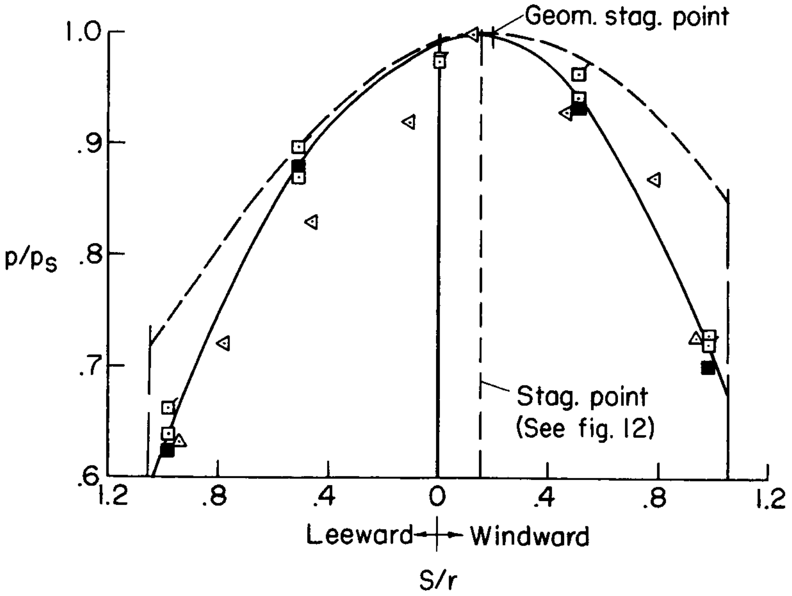

(b) α = 5°

Figure 11.- Pressure distribution on heat shield.

[redacted]

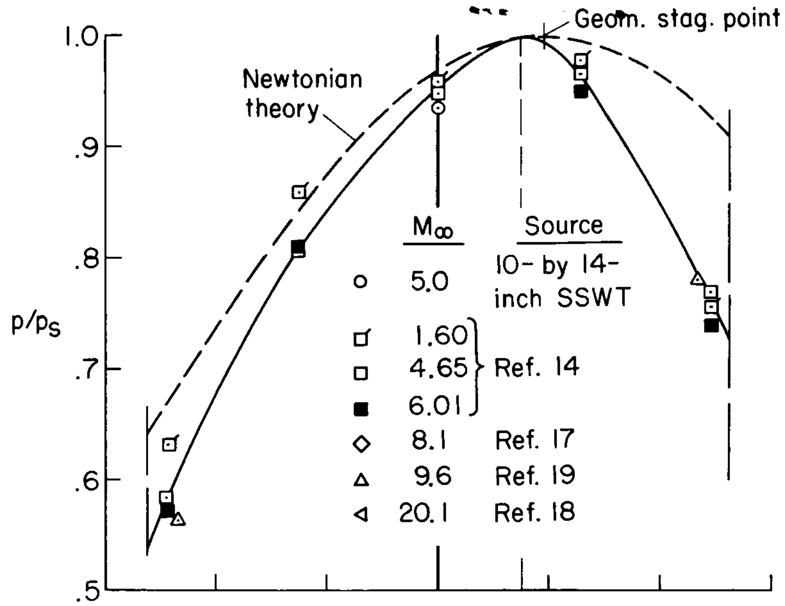

(c) α = 10°

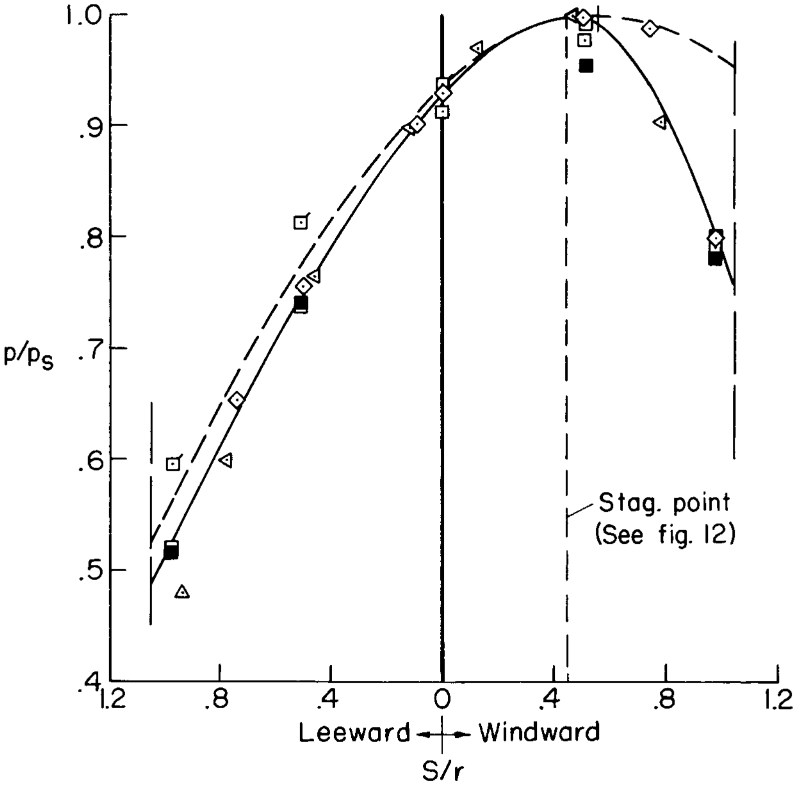

(d) α = 15°

Figure 11.- Concluded.

[redacted]

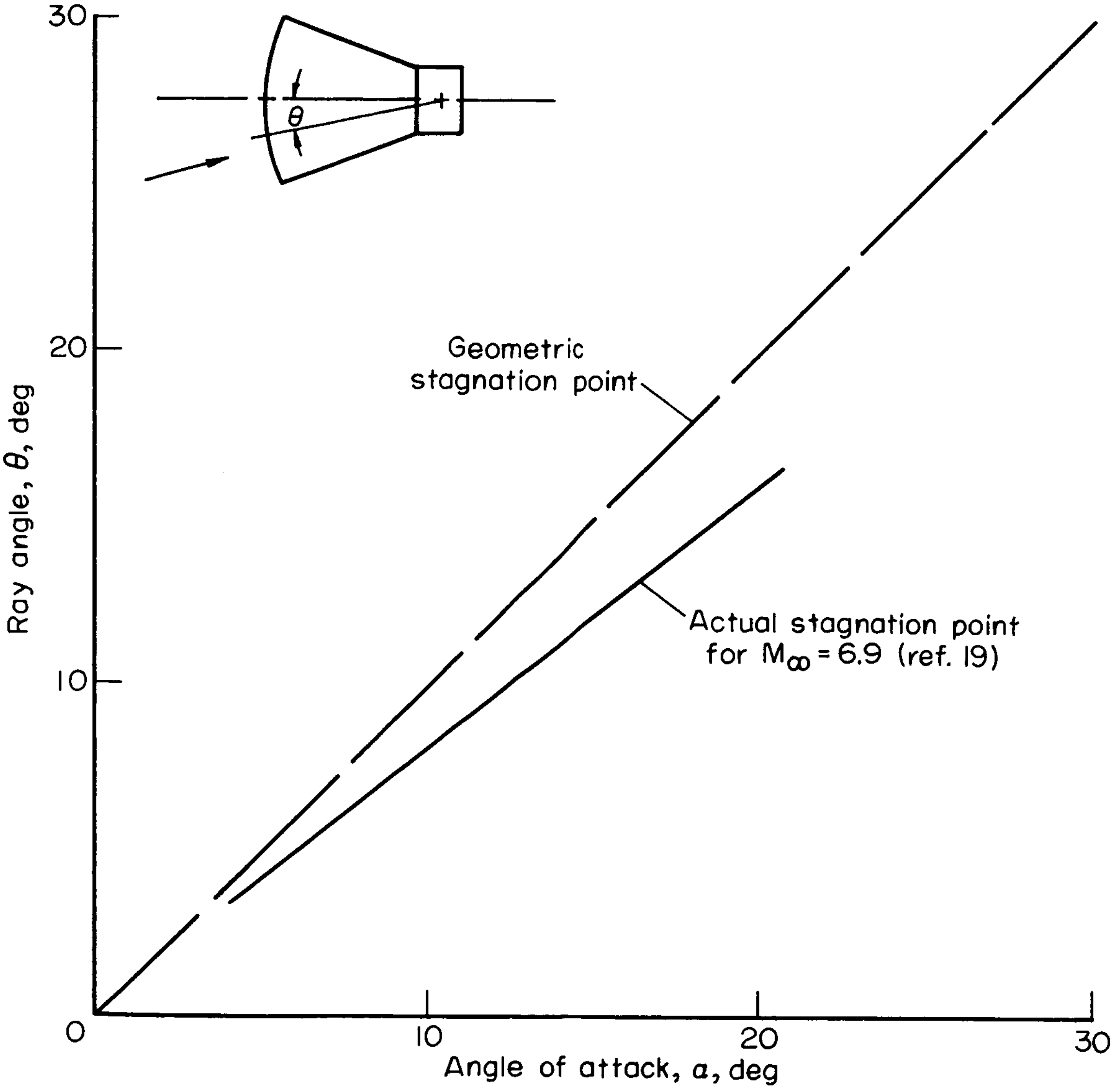

Figure 12.- Variation of stagnation point location with angle of attack.

[redacted]

DECLASSIFIED [redacted]

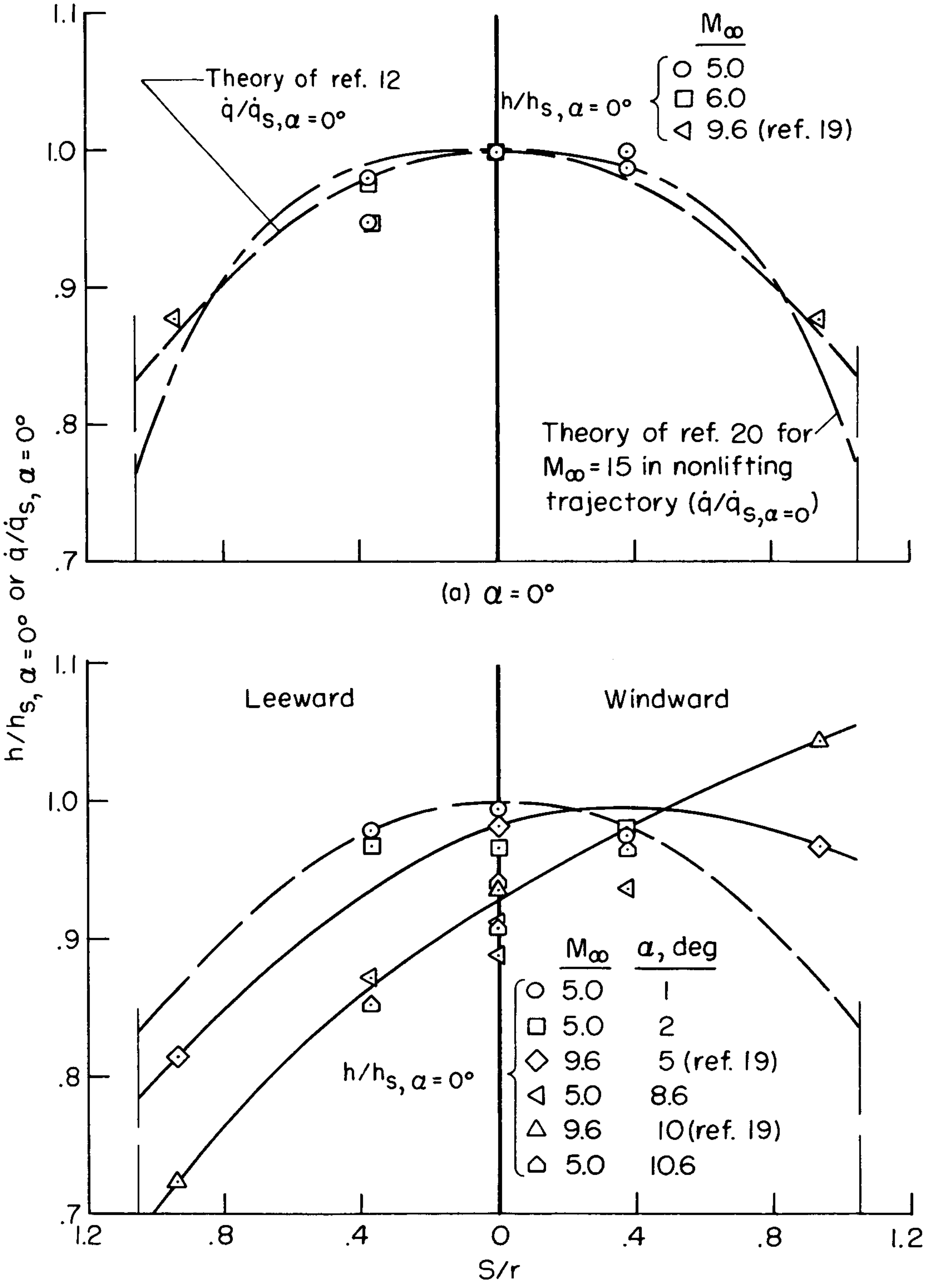

(a) α = 0°

(b) α = 0° to 10.6°

Figure 13.- Heating-rate distribution on the heat shield.

[redacted]

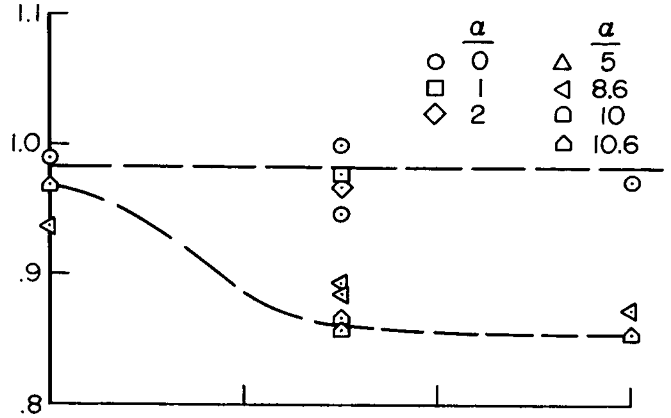

(a) $M_\infty = 5.0$, $S/r = 0.38$

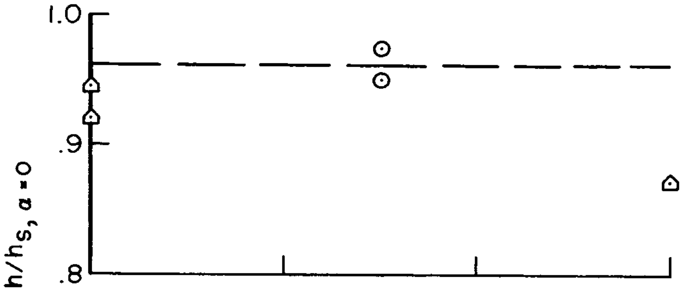

(b) $M_\infty = 6.0$, $S/r = 0.38$

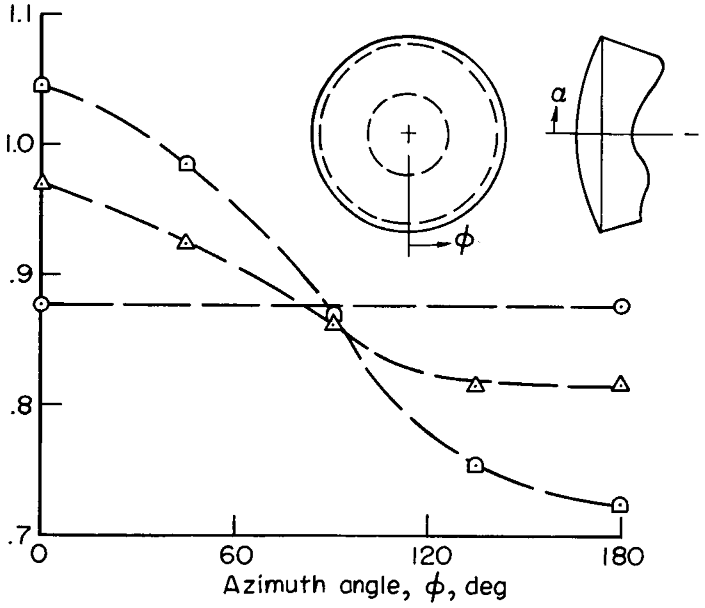

(c) $M_\infty = 9.6$, $S/r = 0.94$ (ref. 19)

Figure 14.- Heating rate on the heat shield as a function of azimuth angle.

[redacted]

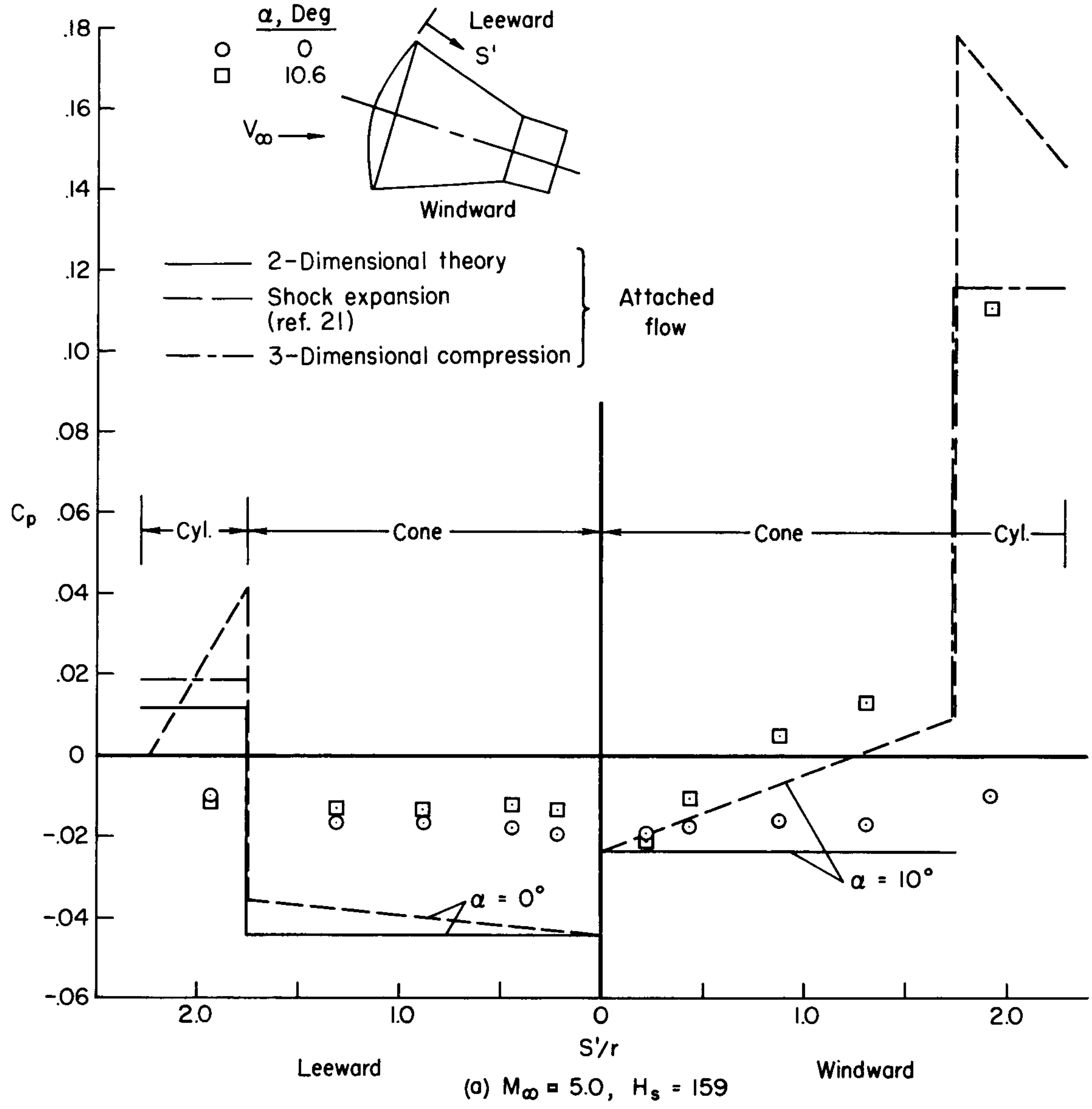

Figure 15.- Longitudinal pressure variation on afterbody.

[redacted]

[redacted]

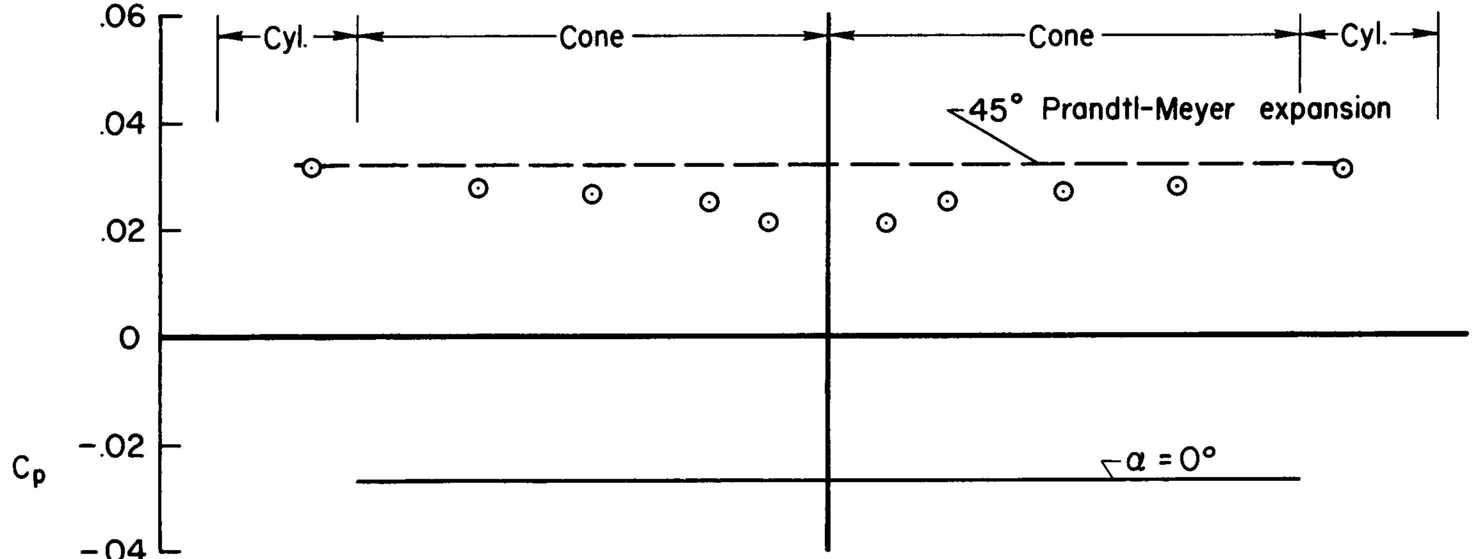

(b) $M_\infty = 6.0,\ H_s = 192$

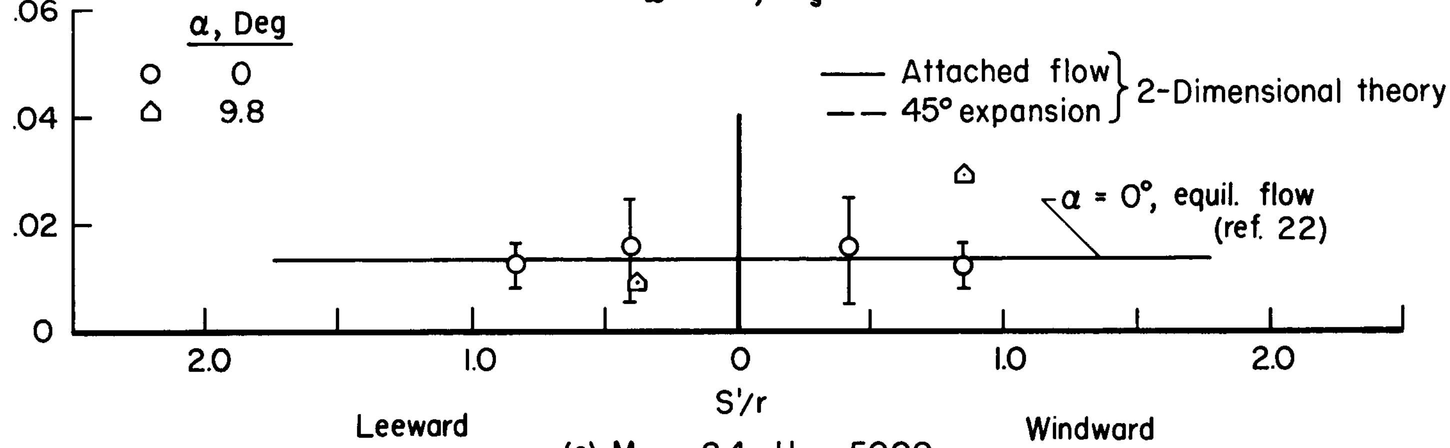

(c) $M_\infty = 8.4,\ H_s = 5000$

Figure 15.- Concluded.

DECLASSIFIED [redacted]

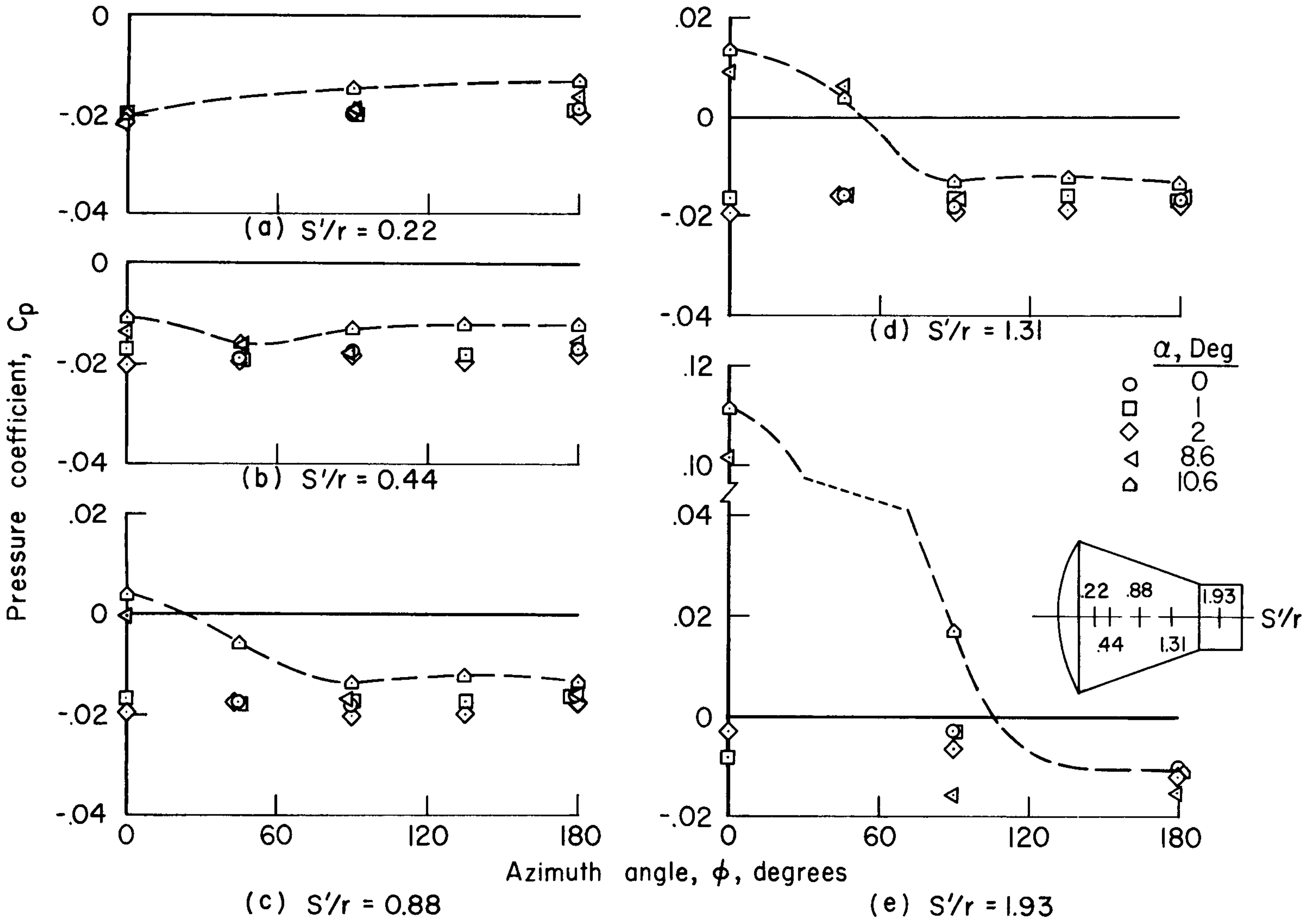

(a) S′/r = 0.22

(b) S′/r = 0.44

(c) S′/r = 0.88

(d) S′/r = 1.31

(e) S′/r = 1.93

Figure 16.- Circumferential distribution of pressures on the afterbody; $M_\infty = 5.0$.

[redacted]

[redacted]

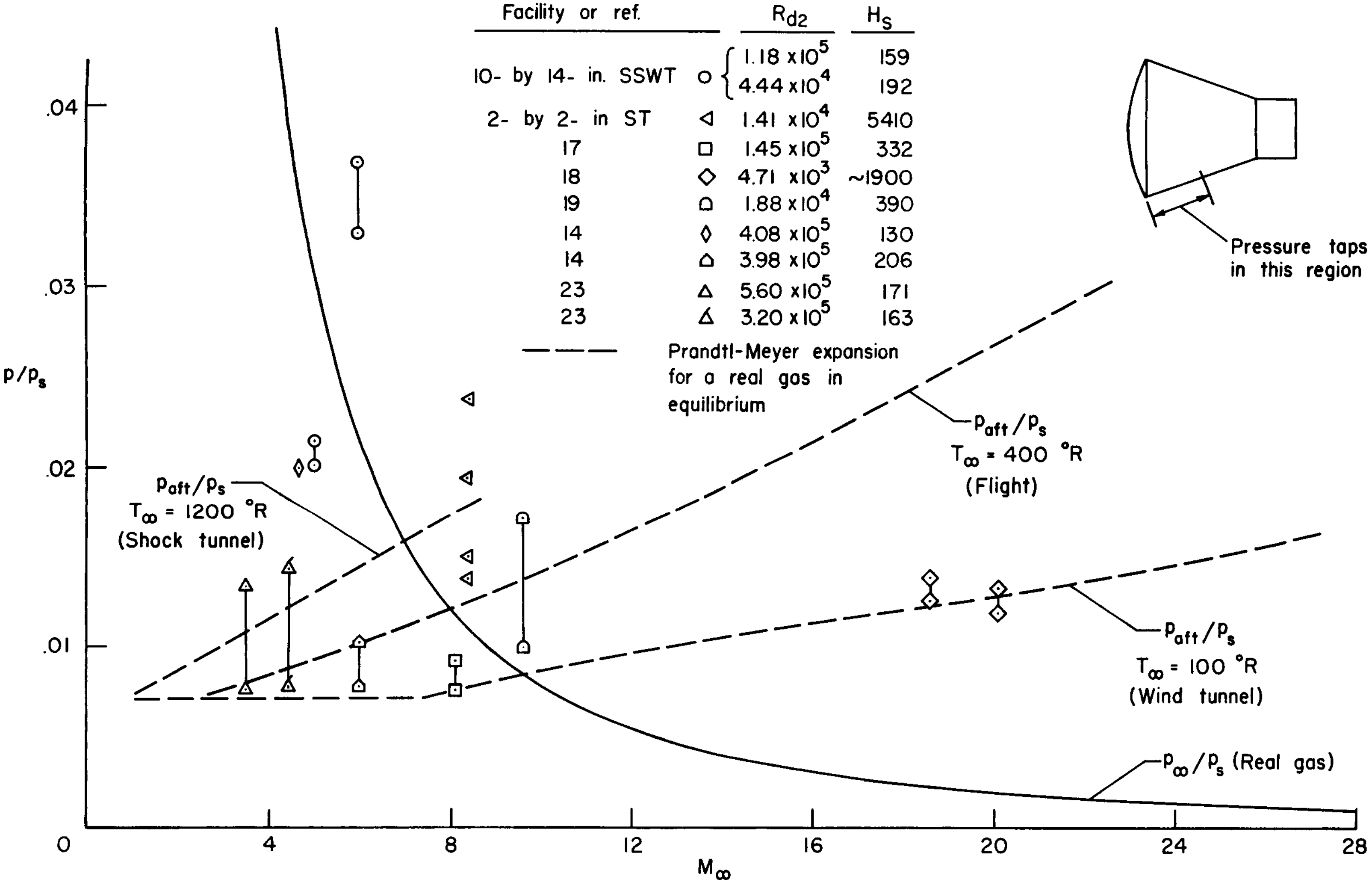

Figure 17.- Theoretical estimate of pressures on conical afterbody; attached flow, $\alpha = 0^\circ$.

[redacted]

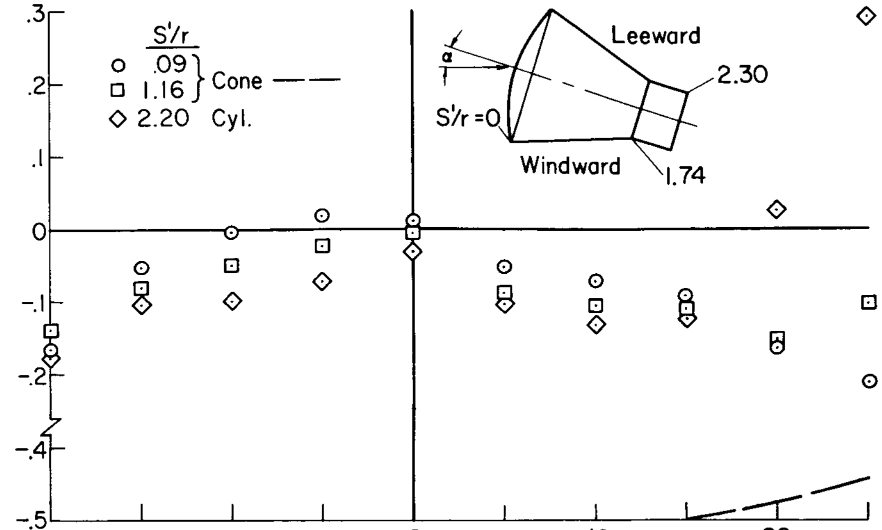

(a) $M_\infty = 1.60$, $R_{d_\infty} = 2.68 \times 10^6$ (ref. 14)

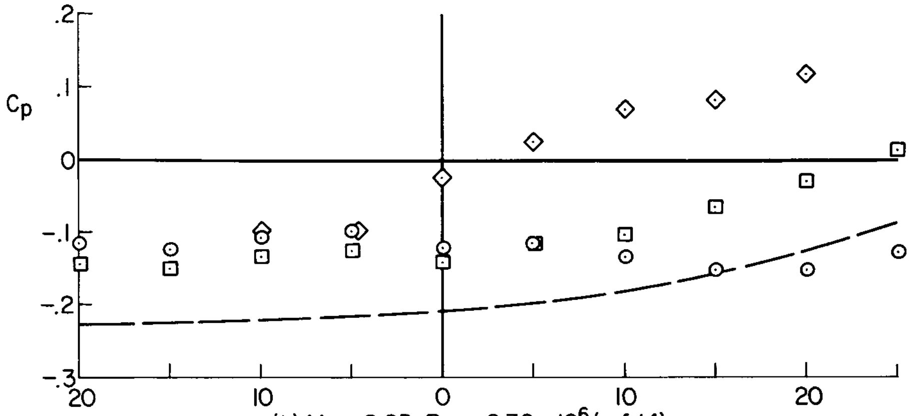

(b) $M_\infty = 2.85$, $R_{d_\infty} = 2.38 \times 10^6$ (ref. 14)

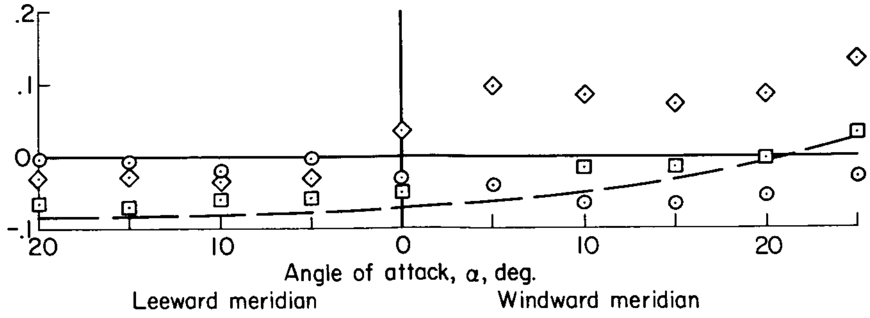

(c) $M_\infty = 4.65$, $R_{d_\infty} = 2.05 \times 10^6$ (ref. 14)

Figure 18.- Afterbody pressures at angle of attack and comparison with theory for attached flow.

[redacted]

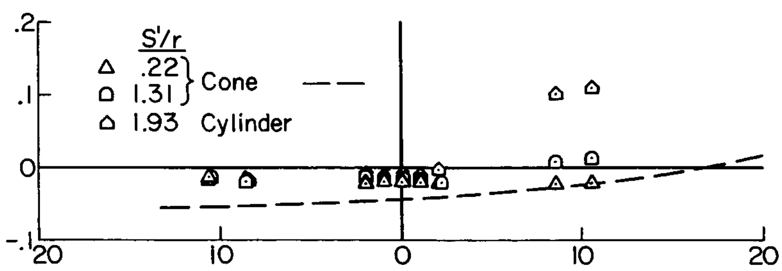

(d) $M_\infty = 5.03$, $R_{d_\infty} = 5.87 \times 10^5$, $H_s = 159$

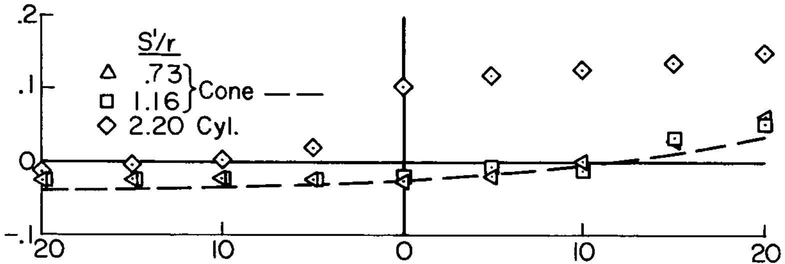

(e) $M_\infty = 6.01$, $R_{d_\infty} = 2.52 \times 10^6$ (ref. 14)

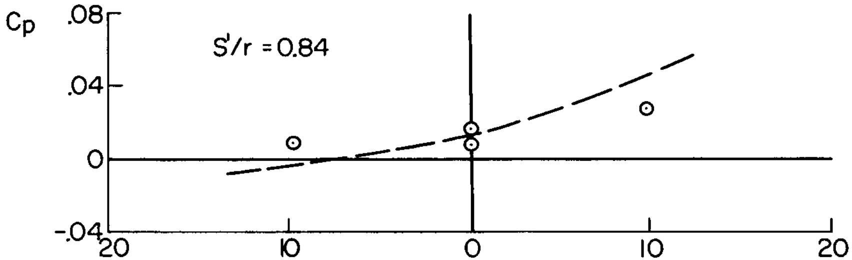

(f) $M_\infty = 8.4$, $R_{d_\infty} = 4.58 \times 10^4$, $H_s = 5000$

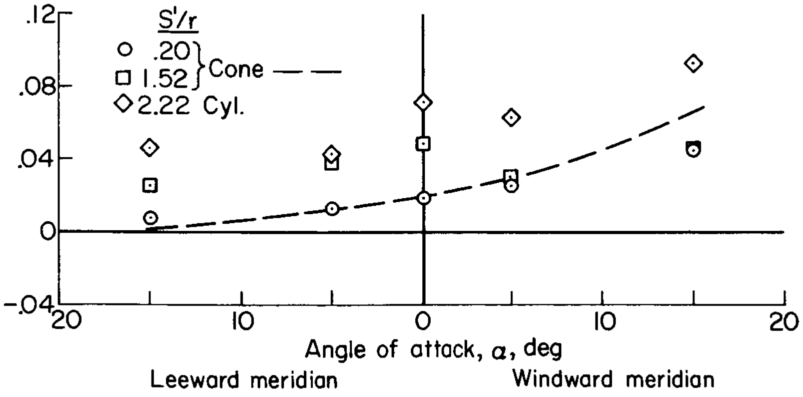

(g) $M_\infty = 20.0-20.3$, $R_{d_\infty} = 0.91 \times 10^5 - 1.17 \times 10^5$, $H_s = 1730-1900$
(ref. 18)

Figure 18.- Concluded.

[redacted]

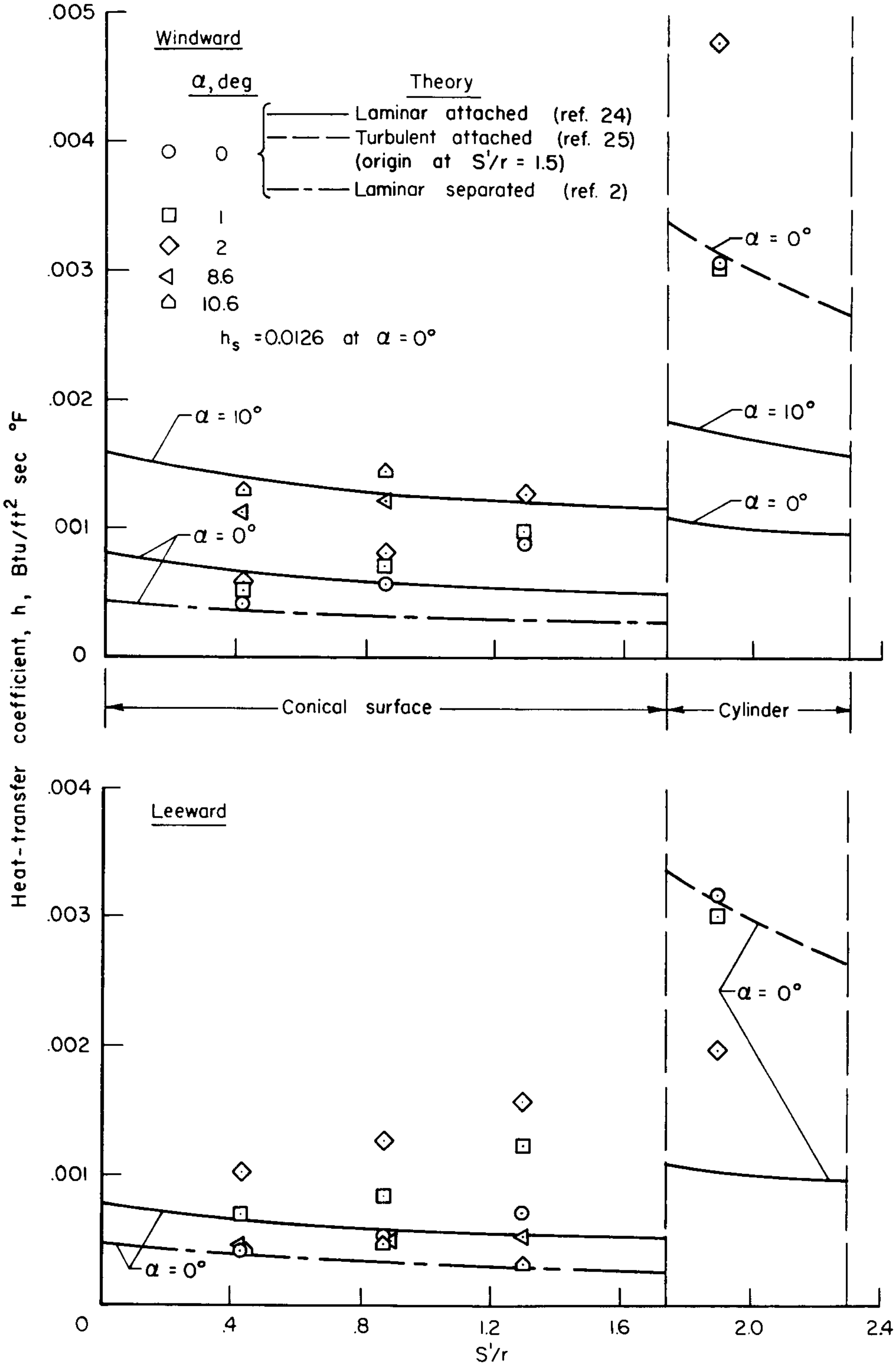

(a) $M_\infty = 5.0$, $R_{d_\infty} = 5.87\times10^5$, $H_s = 159$

Figure 19.- Longitudinal distribution of heating rates on afterbody.

[redacted]

DECL[redacted]SIFIED

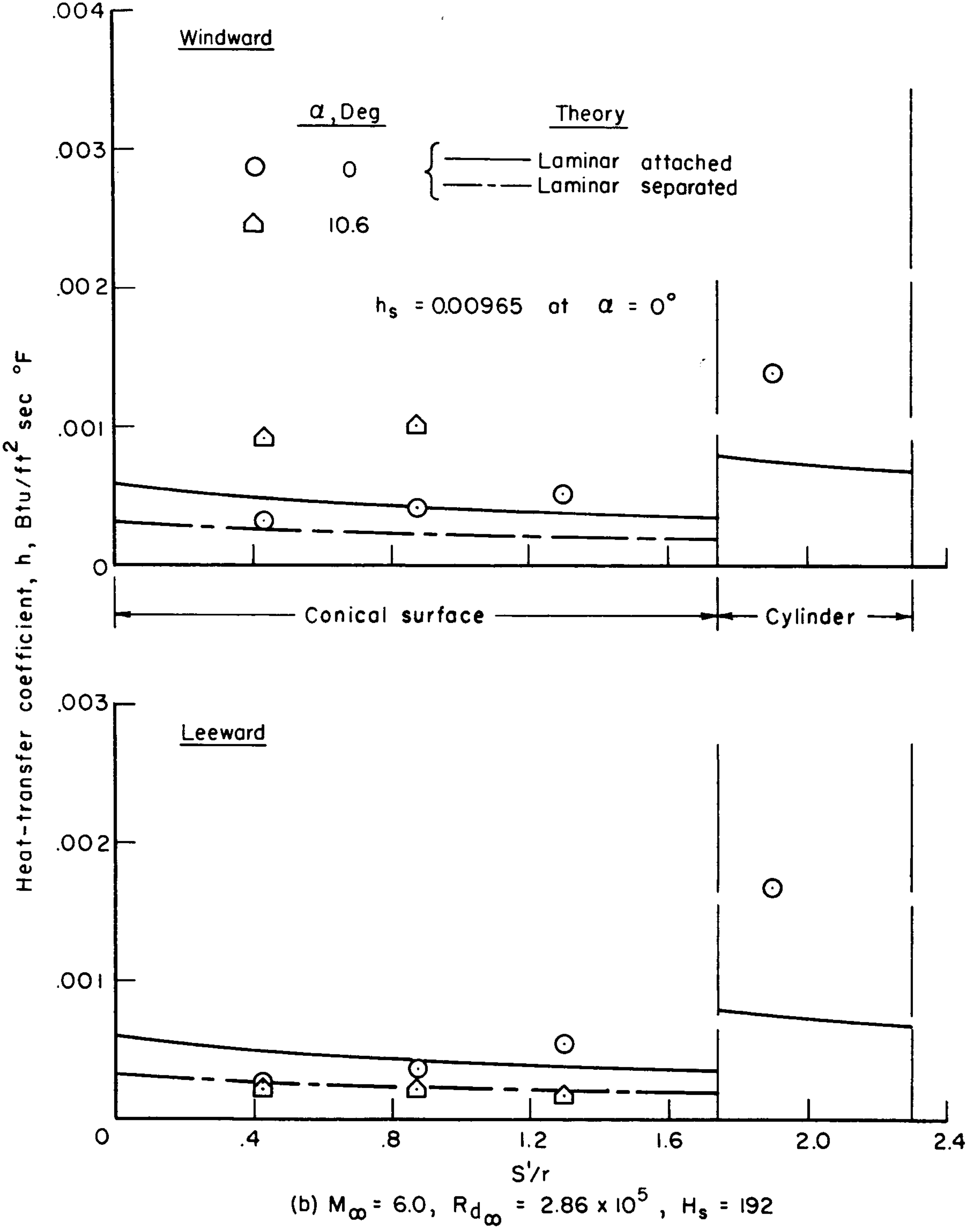

(b) $M_\infty = 6.0$, $R_{d_\infty} = 2.86 \times 10^5$, $H_s = 192$

Figure 19.- Concluded.

[redacted]

DECLASSIFIED

[redacted]

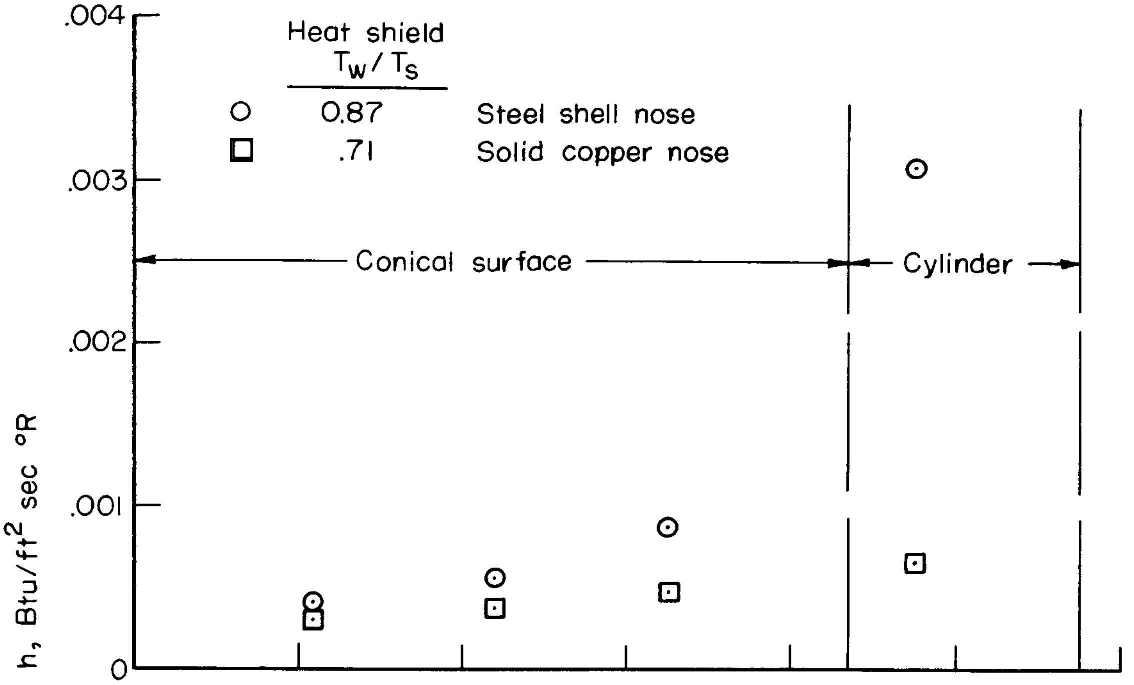

(a) $M_\infty = 5$

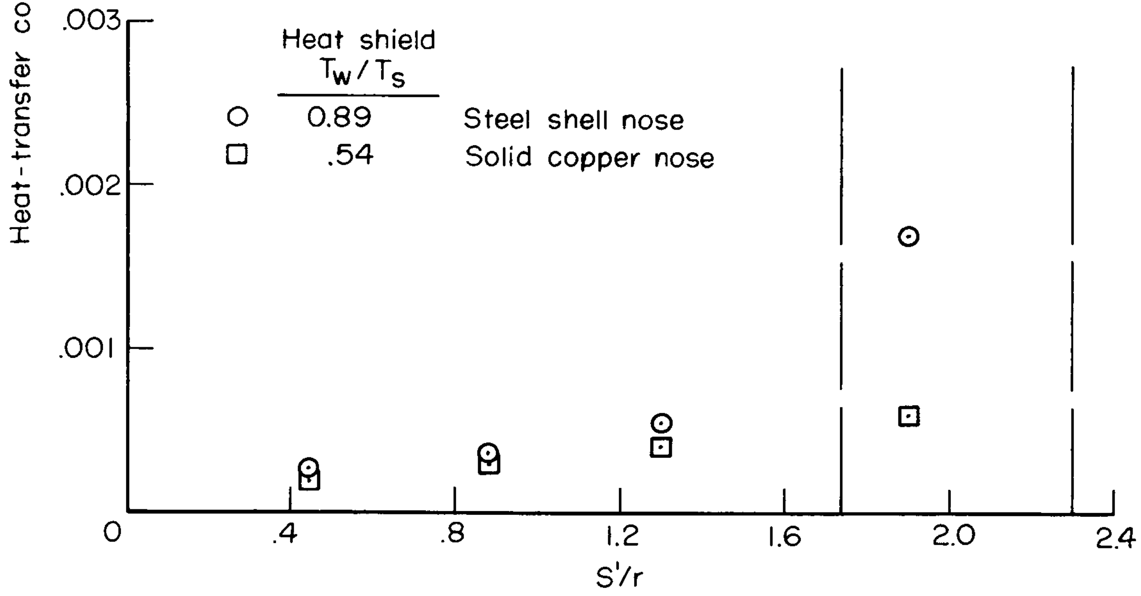

(b) $M_\infty = 6$

Figure 20.- Effect of heat shield temperature on afterbody heating rates; $\alpha = 0^\circ$.

[redacted]

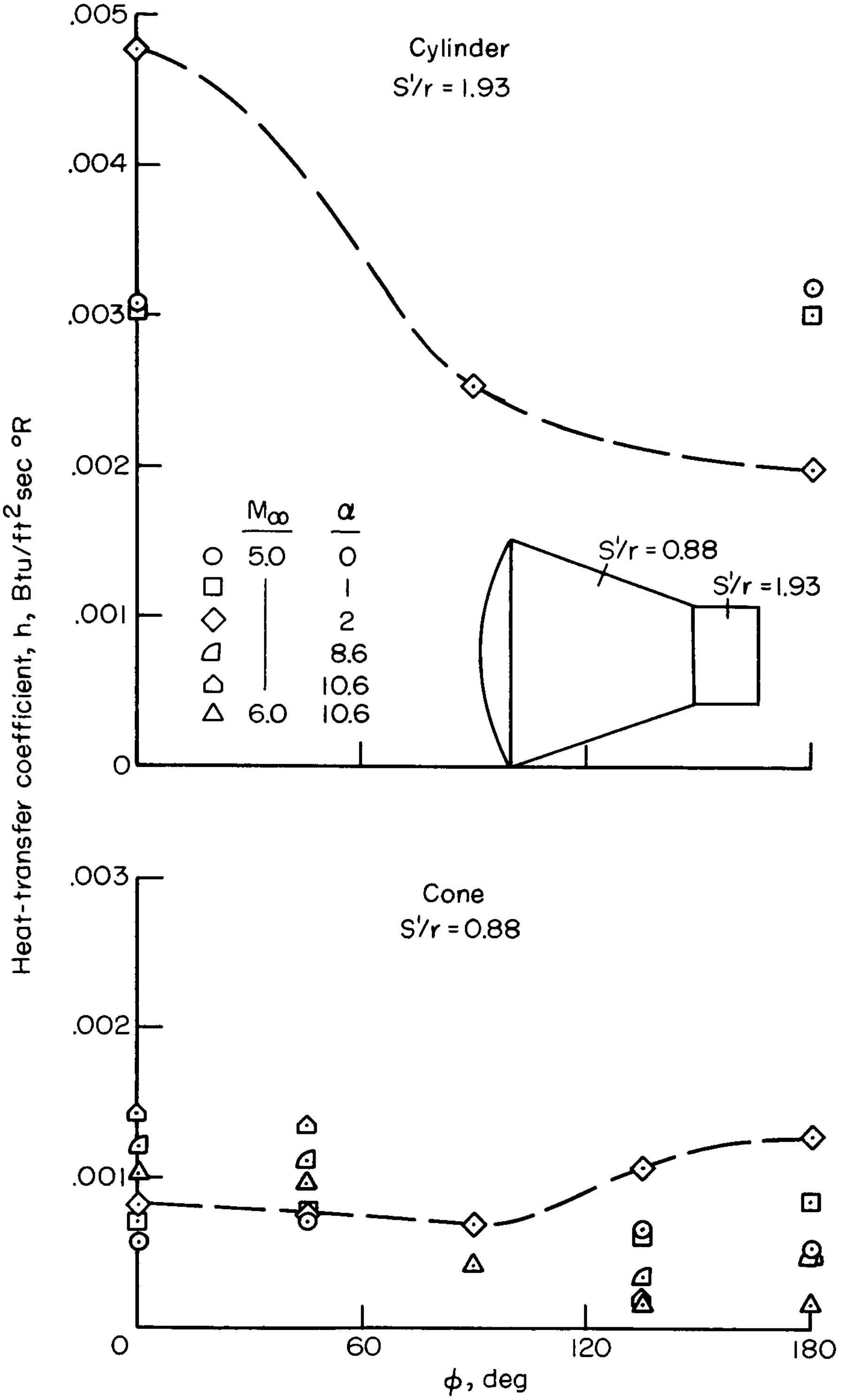

Figure 21.- Circumferential distribution of heating rates on the afterbody; ideal gas.

[redacted]

DECLASSIFIED
~~CONFIDENTIAL~~

[redacted]

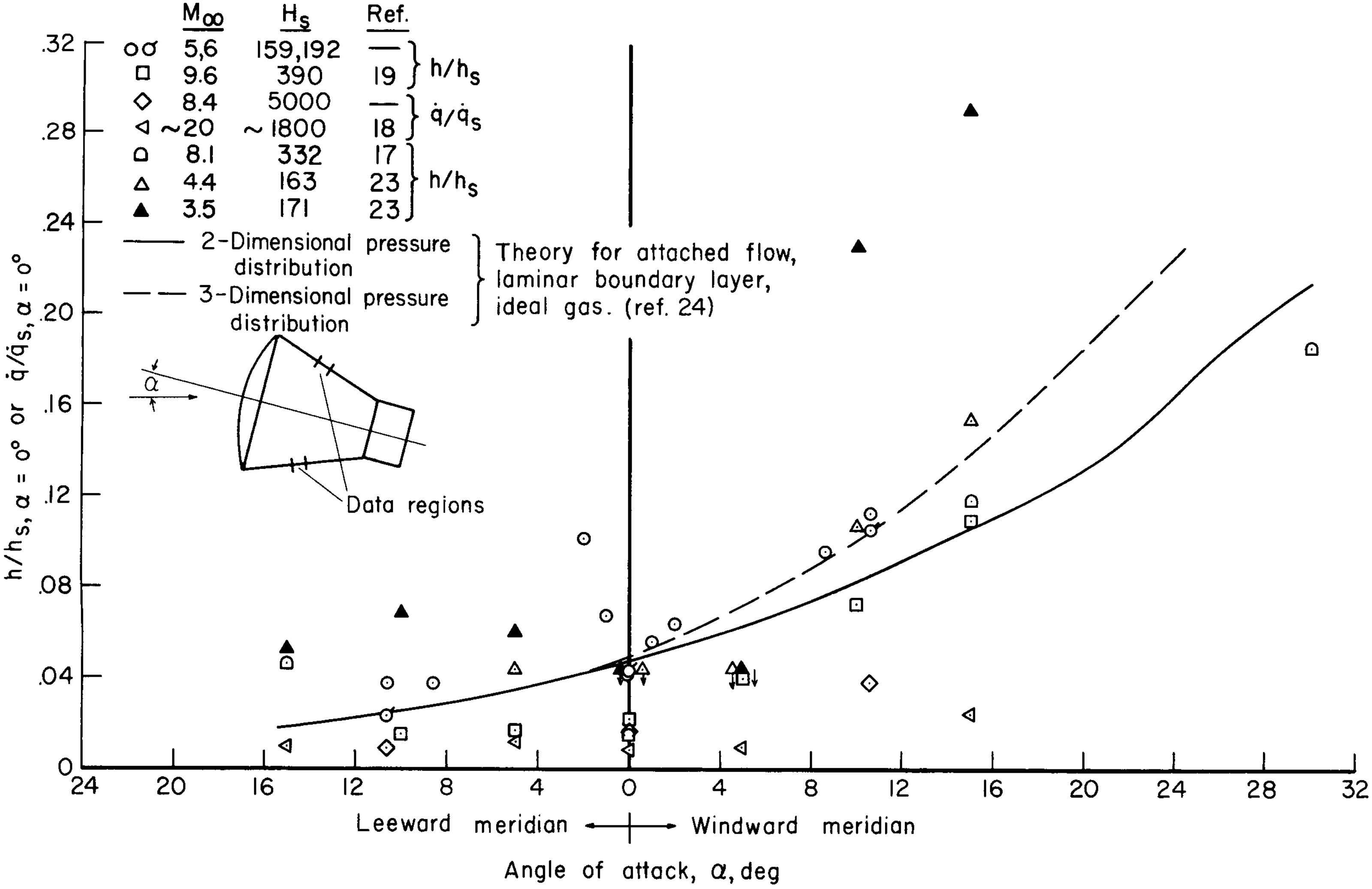

(a) Conical surface, $S'/r \approx 0.9$.

Figure 22.- Variation of afterbody heating rates with angle of attack.

[redacted]

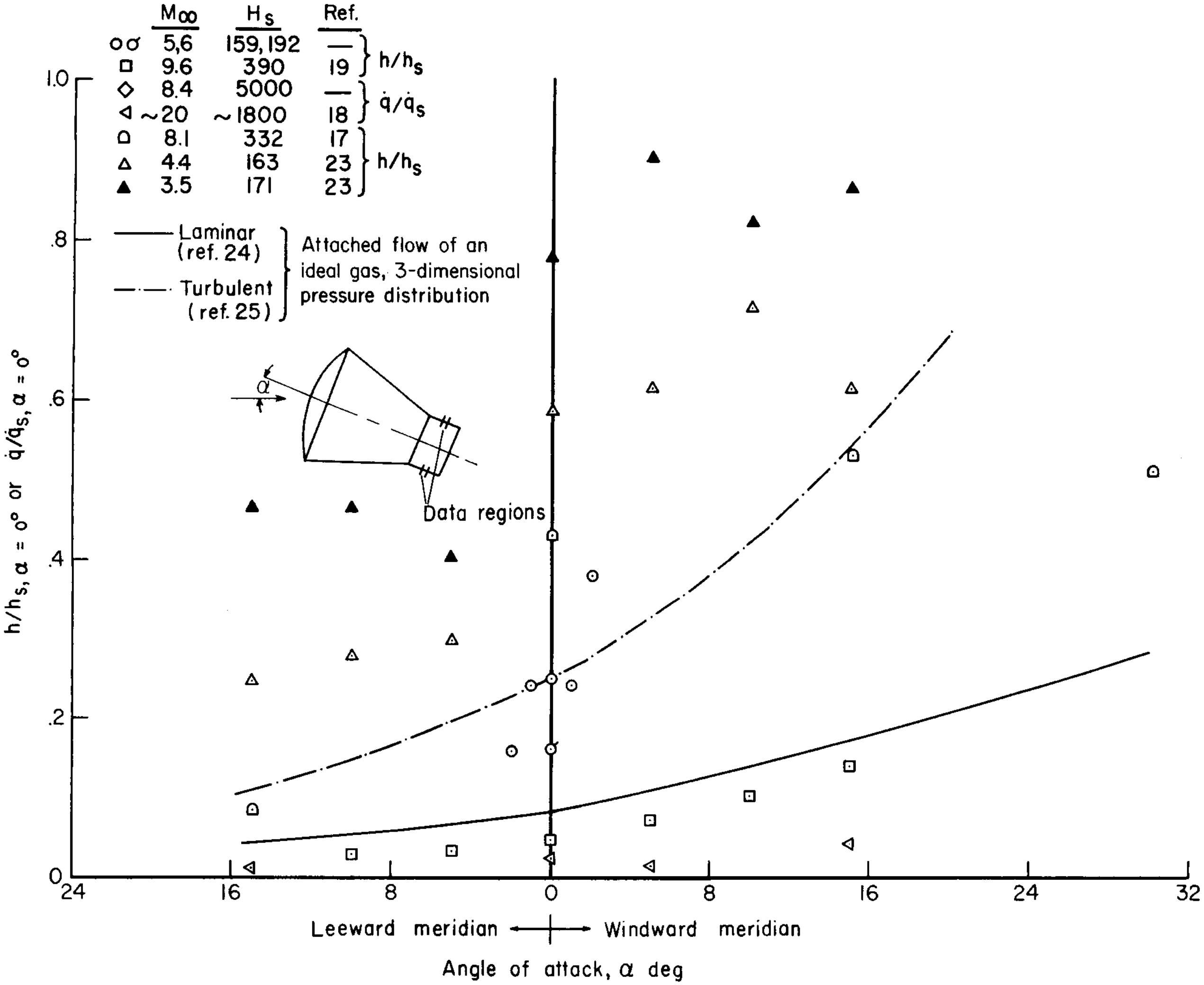

(b) Cylindrical section, S'/r ≈ 1.9.

Figure 22.- Concluded.

[redacted]

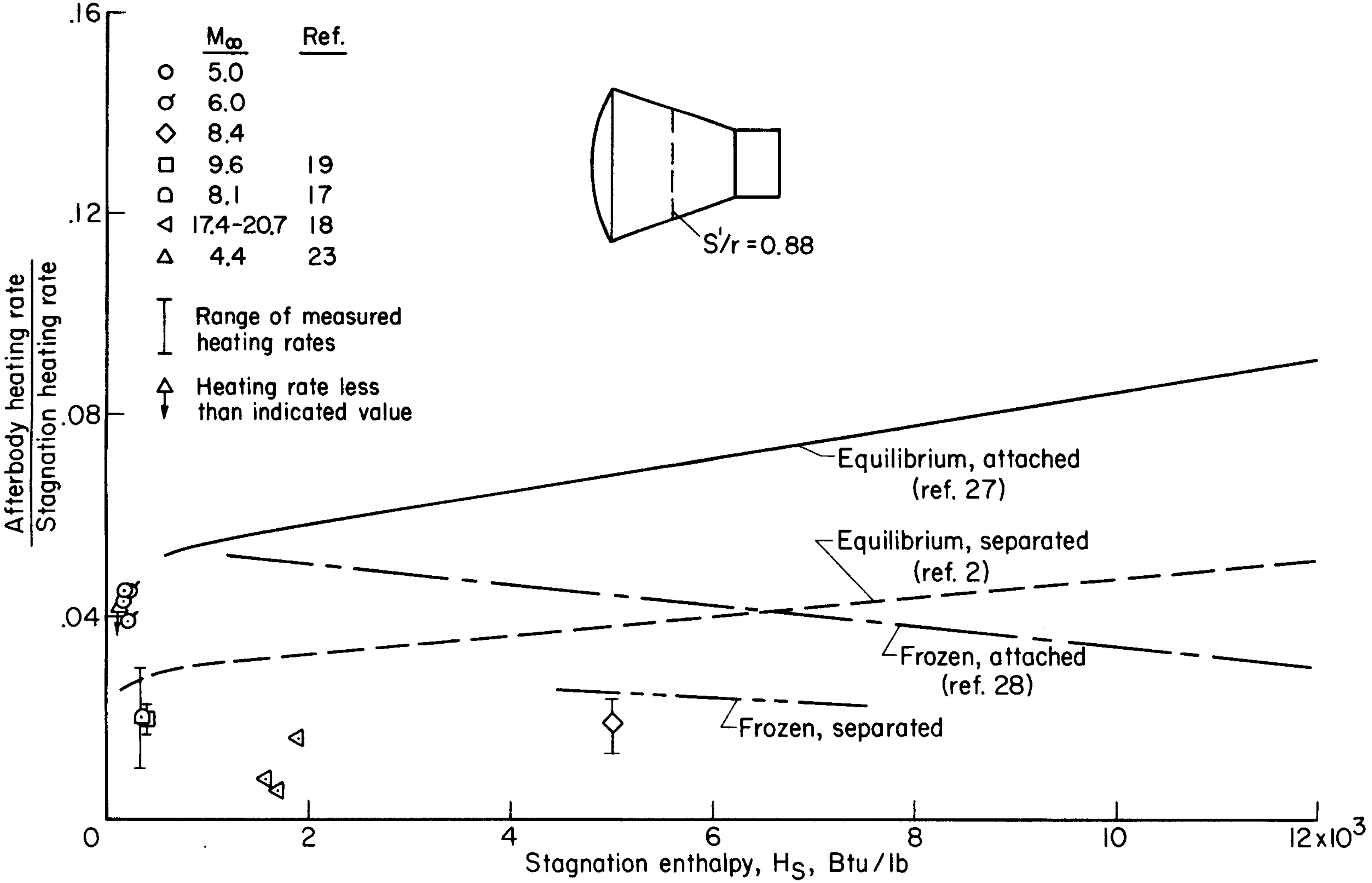

Figure 23.- Variation of heating rate on conical afterbody with stagnation enthalpy, laminar boundary layer; α = 0°.

[redacted]

DEC[redacted]SIFIED

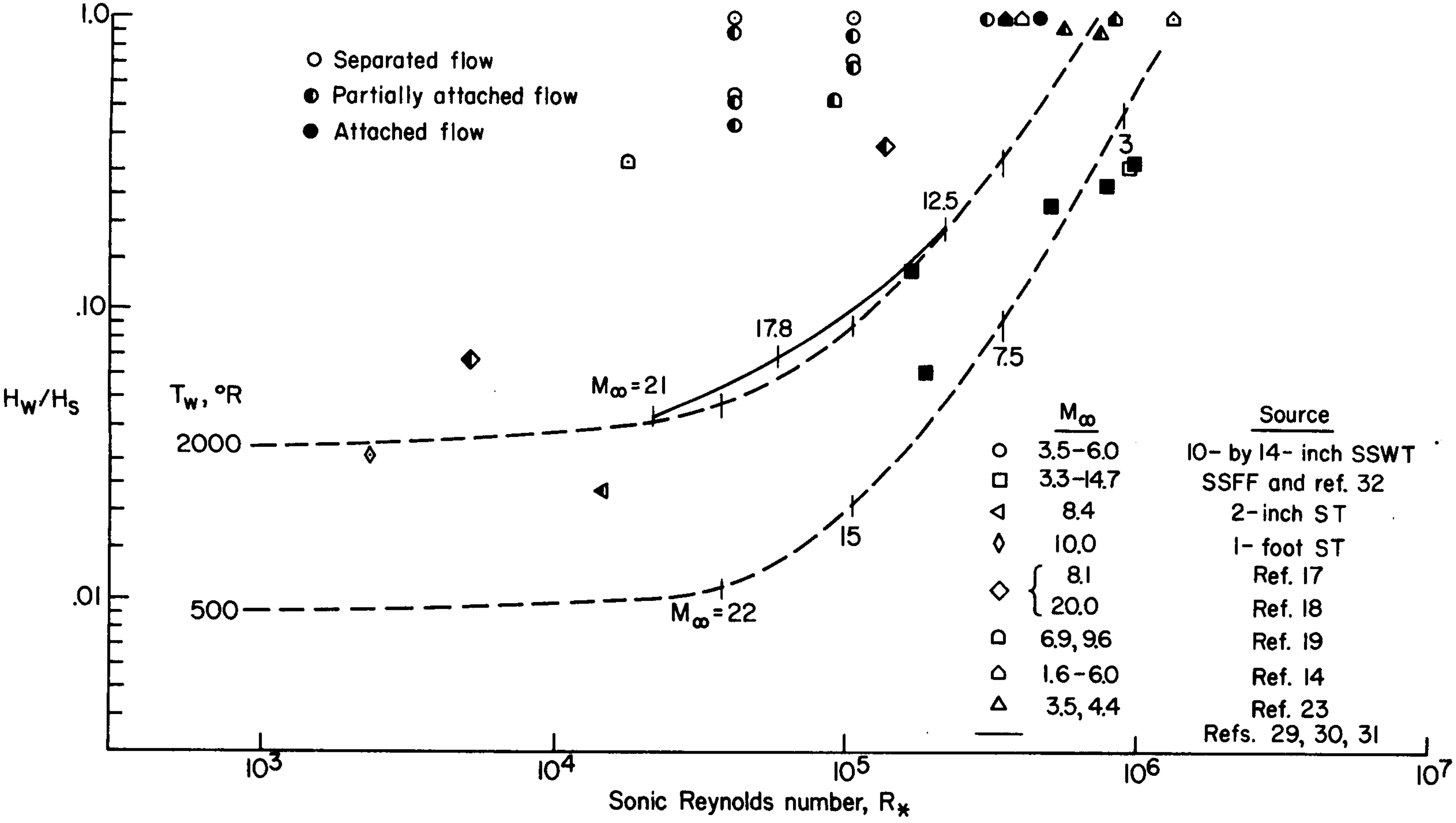

Figure 24.- Afterbody flow regimes; α = 0°.

[redacted]

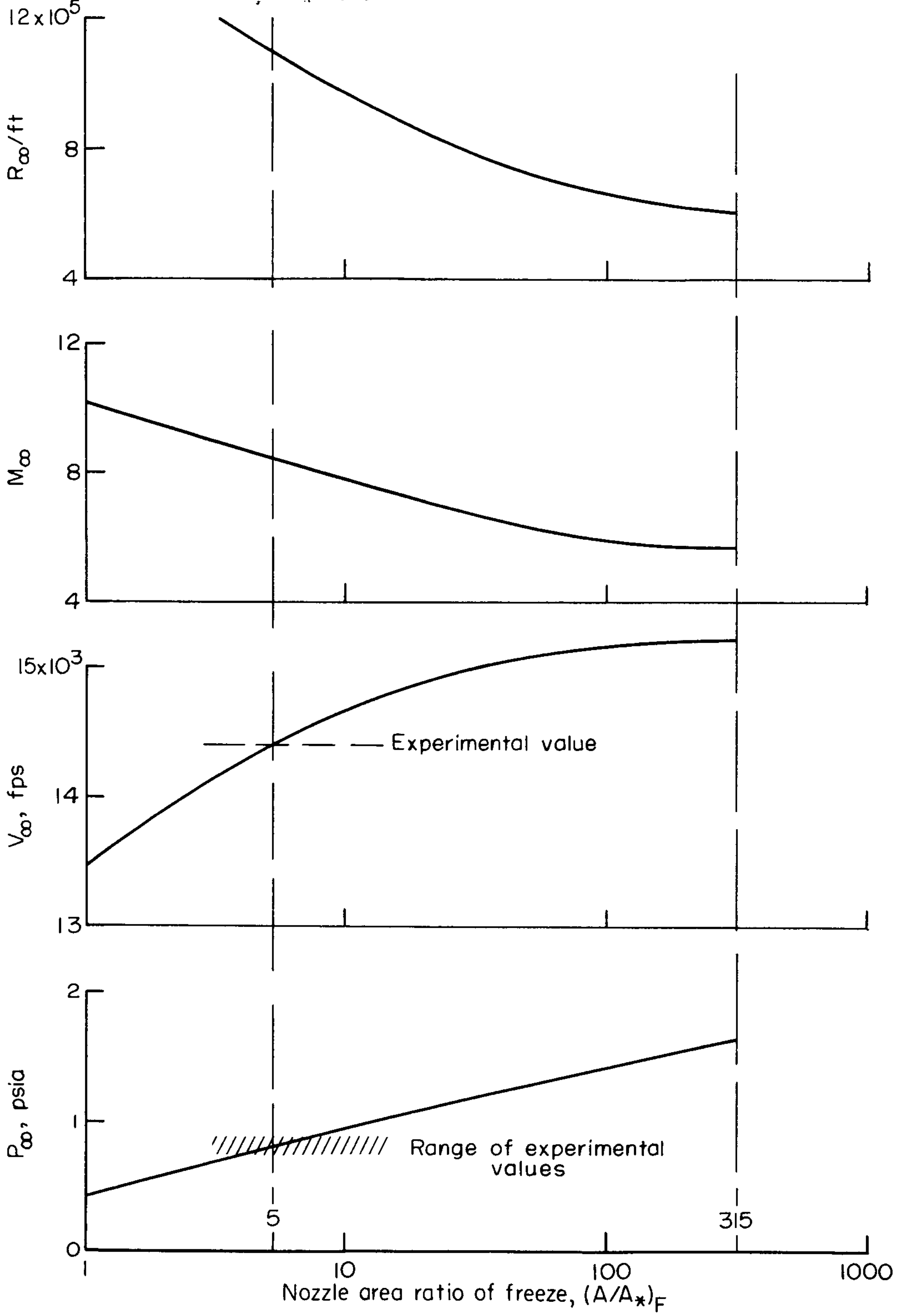

Figure 25.- Shock-tunnel stream conditions for nonequilibrium flow.

[redacted]

DECLASSIFIED [redacted]

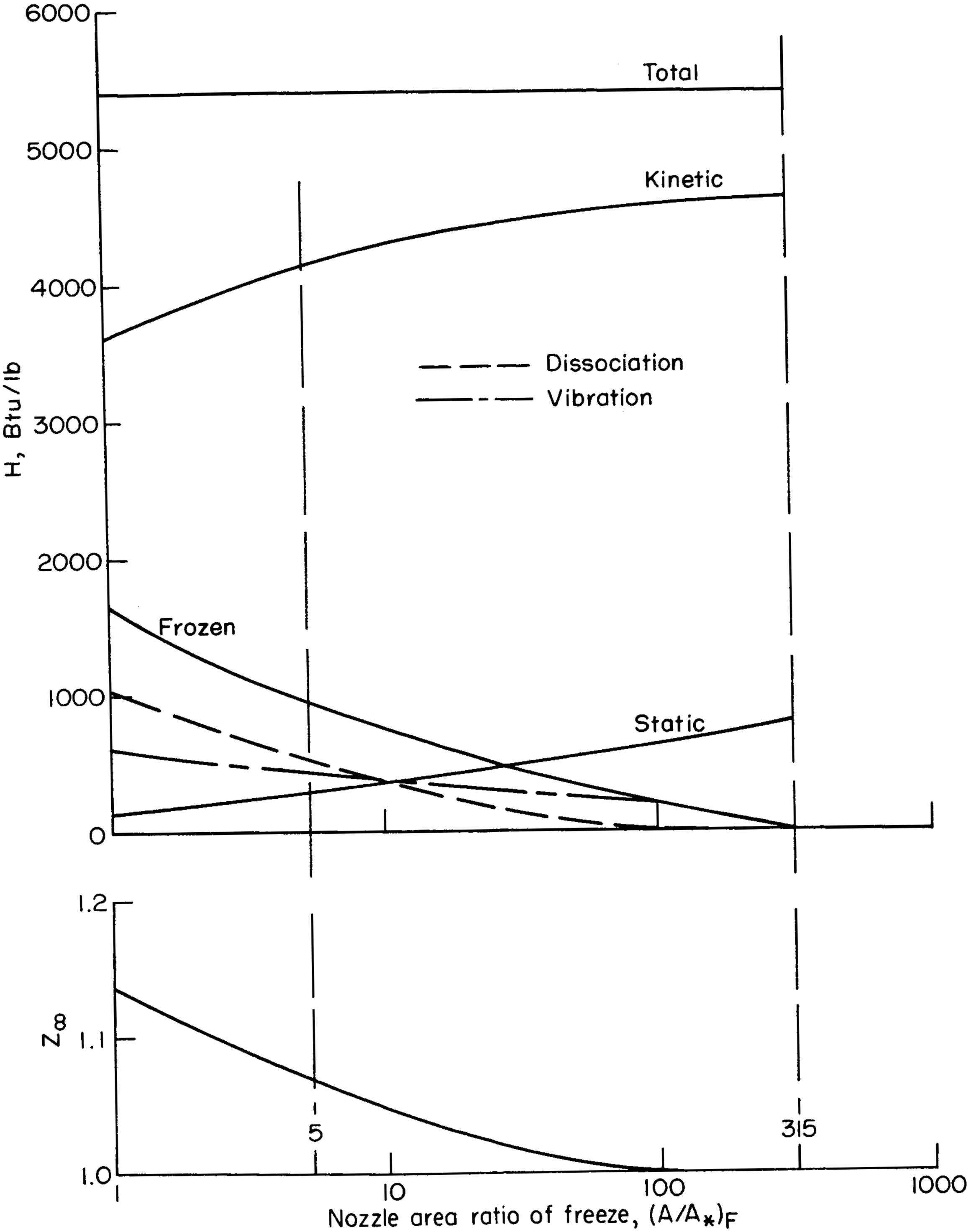

Figure 26.- Energy distribution in nonequilibrium flow.

[redacted]

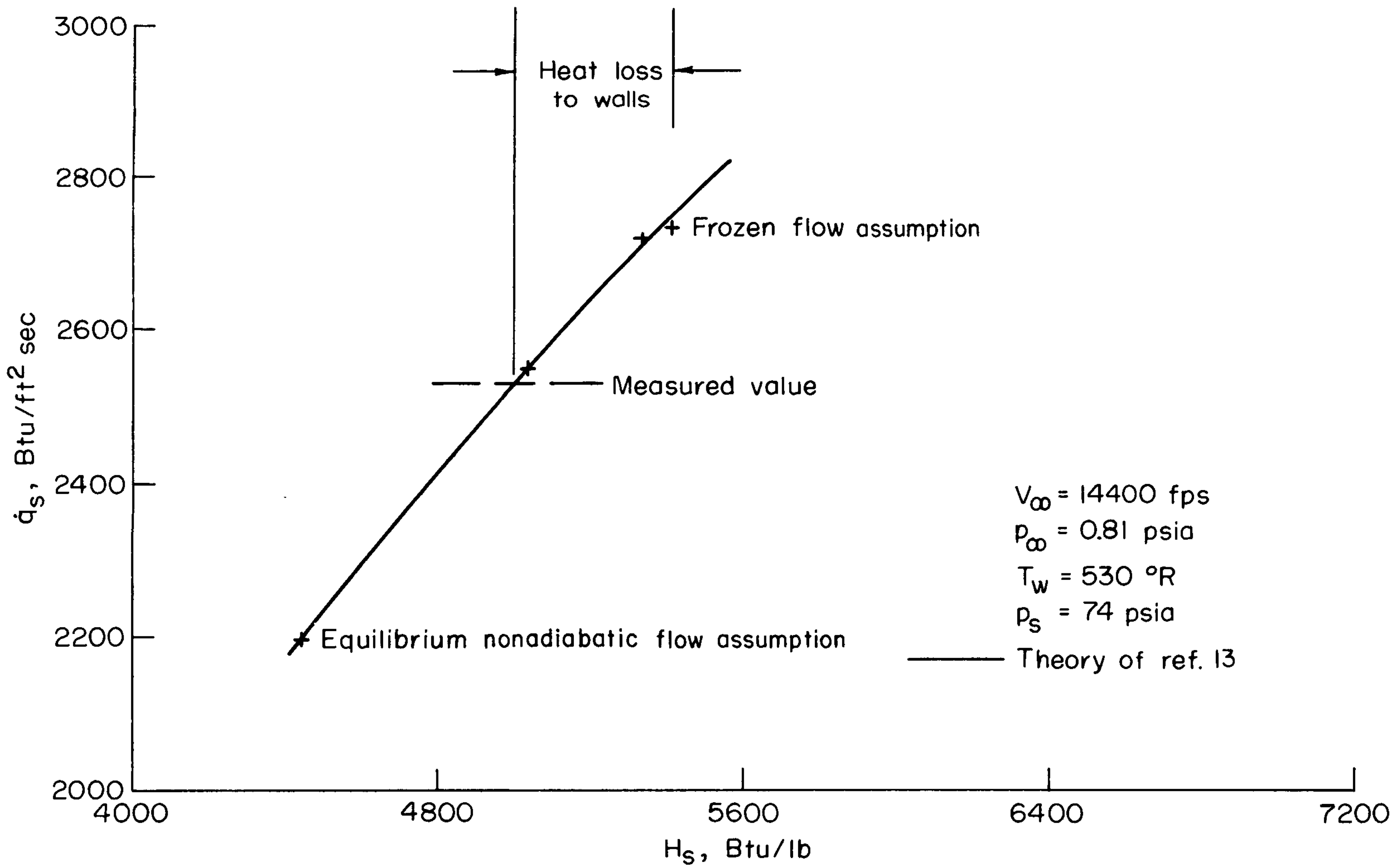

Figure 27.- Variation of heating rate with enthalpy at the stagnation point of a model in the 2-inch shock tunnel.

[redacted]

DECLASSIFIED

[redacted]

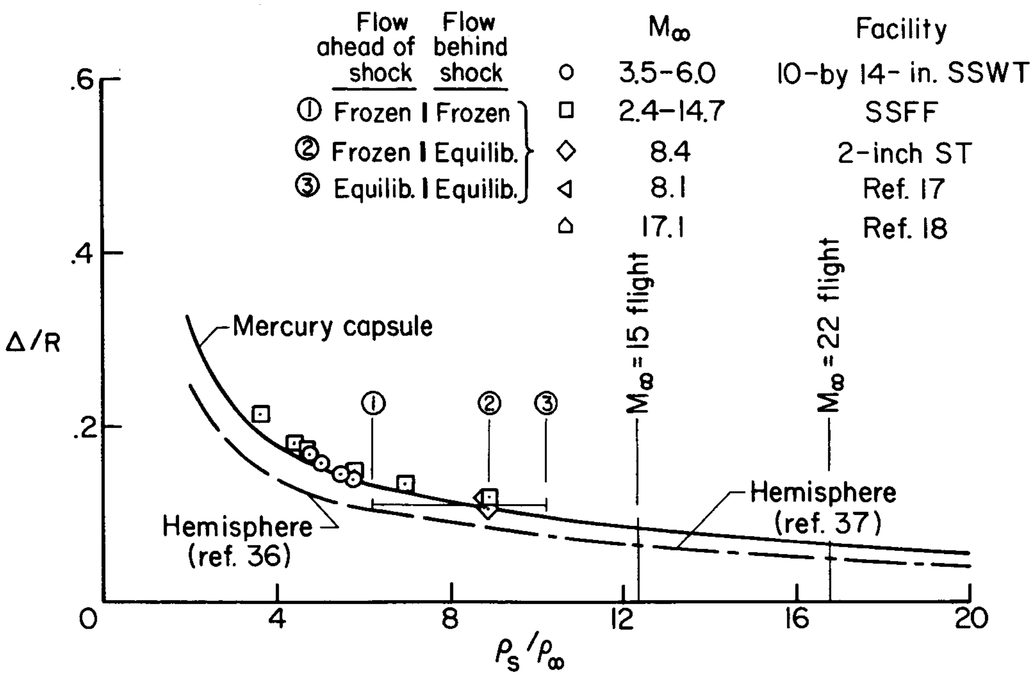

(a) Comparison with theory

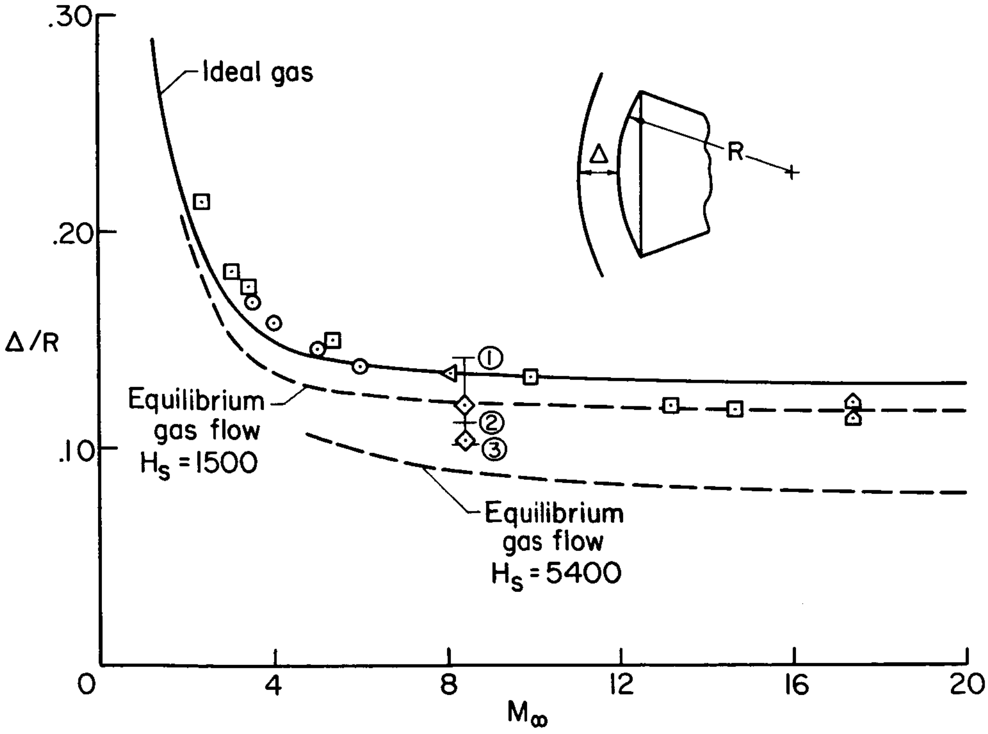

(b) Real gas effects

Figure 28.- Shock detachment distance at $\alpha = 0^\circ$.

[redacted]